UNIVERSITAT DE BARCELONA

# Integral spectroscopy of black hole transients and multi-wavelengh study of a new accreting binary system

María Dolores Caballero García

**ADVERTIMENT**. La consulta d'aquesta tesi queda condicionada a l'acceptació de les següents condicions d'ús: La difusió d'aquesta tesi per mitjà del servei TDX (**www.tdx.cat**) i a través del Dipòsit Digital de la UB (**diposit.ub.edu**) ha estat autoritzada pels titulars dels drets de propietat intel·lectual únicament per a usos privats emmarcats en activitats d'investigació i docència. No s'autoritza la seva reproducció amb finalitats de lucre ni la seva difusió i posada a disposició des d'un lloc aliè al servei TDX ni al Dipòsit Digital de la UB. No s'autoritza la presentació del seu contingut en una finestra o marc aliè a TDX o al Dipòsit Digital de la UB (framing). Aquesta reserva de drets afecta tant al resum de presentació de la tesi com als seus continguts. En la utilització o cita de parts de la tesi és obligat indicar el nom de la persona autora.

**ADVERTENCIA**. La consulta de esta tesis queda condicionada a la aceptación de las siguientes condiciones de uso: La difusión de esta tesis por medio del servicio TDR (**www.tdx.cat**) y a través del Repositorio Digital de la UB (**diposit.ub.edu**) ha sido autorizada por los titulares de los derechos de propiedad intelectual únicamente para usos privados enmarcados en actividades de investigación y docencia. No se autoriza su reproducción con finalidades de lucro ni su difusión y puesta a disposición desde un sitio ajeno al servicio TDR o al Repositorio Digital de la UB. No se autoriza la presentación de su contenido en una ventana o marco ajeno a TDR o al Repositorio Digital de la UB (framing). Esta reserva de derechos afecta tanto al resumen de presentación de la tesis como a sus contenidos. En la utilización o cita de partes de la tesis es obligado indicar el nombre de la persona autora.

**WARNING**. On having consulted this thesis you're accepting the following use conditions: Spreading this thesis by the TDX (**www.tdx.cat**) service and by the UB Digital Repository (**diposit.ub.edu**) has been authorized by the titular of the intellectual property rights only for private uses placed in investigation and teaching activities. Reproduction with lucrative aims is not authorized nor its spreading and availability from a site foreign to the TDX service or to the UB Digital Repository. Introducing its content in a window or frame foreign to the TDX service or to the UB Digital Repository is not authorized (framing). Those rights affect to the presentation summary of the thesis as well as to its contents. In the using or citation of parts of the thesis it's obliged to indicate the name of the author.

**UNIVERSITAT DE BARCELONA**
**Facultat de Física i Química**
**Departament d'Astronomia i Meteorologia**


# INTEGRAL SPECTROSCOPY OF BLACK HOLE TRANSIENTS AND MULTI-WAVELENGTH STUDY OF A NEW ACCRETING BINARY SYSTEM

**María Dolores Caballero García**
**Barcelona, 2008**

**UNIVERSITAT DE BARCELONA**
Facultat de Física i Química
(Departament d'Astronomia i Meteorologia)

*Programa d' Astronomia i Meteorologia*
*Bienni 2001-2002*

# INTEGRAL SPECTROSCOPY OF BLACK HOLE TRANSIENTS AND MULTI-WAVELENGTH STUDY OF A NEW ACCRETING BINARY SYSTEM

Dirigido por el **Dr. Jose Miguel Mas-Hesse**
en el
Laboratorio de Astrofísica Espacial y Física Fundamental
(INSTITUTO NACIONAL DE TÉCNICA AEROESPACIAL)

Tutelado por la **Dra. Francesca Figueras Siñol**
en el
Departament d'Astronomia i Meteorologia
(UNIVERSITAT DE BARCELONA)

Memoria presentada por
**María Dolores Caballero García**
para aspirar al grado de
**Doctora en Ciencias Físicas**

Barcelona, marzo 2008

*A mis padres, Juan y Dolores.*

# Acknowledgements

This work surely would not have been possible without the help of all the people that I will mention in these acknowledgements. All of them are important and provided me the necessary strength to keep on going, reminding me that my illusion for the Astronomy science came from a long time ago.

First and foremost, I would like to show my gratefulness to Jordi Torra, Francesca Figueras and Carme Jordi, for allowing me my entrance to this fascinating world when I finished my Physics degree in 2001. I also thank Francesc Vilardell and Salvador Ribas, for all the experiences shared during our *Cel Fosc* campaigns.

Also to José Miguel Mas-Hesse and Albert Domingo for introducing me to the space and satellite astrophysics. All my knowledge of CCD detectors and space platforms came from my admiration of their work. I duplicate my gratefulness to José Miguel Mas-Hesse for giving me the opportunity to iniciate this thesis and being my advisor during all these years.

This work would not have been possible without Ignasi Ribas, Peter Kretschmar and Erik Kuulkers, who understood my personal motivation regarding binary systems and gave me very interesting insights. Very special thanks to Jon Miller, for being so involved in my studies regarding black holes and for giving me the chance of studying these systems.

Thanks to the Spanish council for funding me with a PhD grant during 2003-2007 and also to the personal at LAEFF (Margie Guitart, Benjamín Montesinos, Sergio Suárez, Carlos Núñez Barranco and a large etcetera) for providing the best resources. Also to my friends, for all the good moments shared in Madrid. In general, to all the LAEFF staff, who I have met during all these years, for making exciting my staying there.

My most grateful thanks to my parents, for their understanding and cooperation, without them this work definitely would not have been possible.

María Dolores Caballero García,
15 de marzo de 2008

# List of contents

# List of Figures

# List of Tables

# Resumen

En esta tesis utilizamos los instrumentos de altas energías del satélite *INTEGRAL* para hacer espectroscopía y la cámara OMC para hacer fotometría de dos tipos diferentes de objetos celestes emisores de rayos X. *INTEGRAL* permite obtener la espectroscopía en rayos X y $\gamma$ (cubriendo un rango espectral de 3–8 000 keV) y OMC es una cámara CCD que opera en el filtro V de Johnson, capaz de proporcionar una monitorización continua de las fuentes científicas incluídas en el *OMC Input Catalogue*. La capacidad de hacer espectroscopía nos permitió el estudio de la emisión de alta energía de dos sistemas transitorios con agujero negro (i.e. GRO J1655–40 y GX 339–4) dando nuevas pistas acerca de la física de los procesos de emisión en alta energía (rayos X y $\gamma$) de este tipo de objetos. OMC, el monitor óptico a bordo del satélite *INTEGRAL*, nos permitió hacer un análisis multi-longitud de onda de TYC 2675- 663-1, desvelando que se trata de un sistema binario con propiedades dominadas por acreción. Mientras que el estudio de los sistemas transitorios con agujero negro estudiados en esta tesis corresponden a observaciones dedicadas tras la aceptación de un programa de observación, TYC 2675-663-1 corresponde a parte de un programa de ciencia serendípita.

En esta tesis se presenta el descubrimiento de 3 nuevos sistemas binarios (TYC 2675 663 1, TYC 237 363 1 y HD 86222) en base a sus propiedades fotométricas, todos mostrando emisión en rayos X blandos ya que pertenecen al catalogo ROSAT. Para dos de estos sistemas, la emisión en rayos X es la esperada en estrellas de rotación rápida y debido a actividad cromosférica. Para TYC 2675- 663-1 la situación es diferente ya que se detectó un exceso en la emisión en rayos X blandos de $\approx$50%. Se inició una campaña fotométrica y espectroscópica para desvelar el origen de este exceso y la naturaleza de ambas componentes del sistema binario. Como resultado, se detectaron un pronunciado efecto O-Connell, comportamiento errático en forma de erupciones y la presencia de mínimos asimétricos y diferentes máximos ocasionalmente en la curva de luz. La espectroscopía permitió detectar emisión notable y ensanchada de las líneas $H_\alpha$ and He I con perfil P Cygni. Esto es debido a procesos de acreción y a la presencia de vientos estelares notables en el sistema binario. Todas estas propiedades llevan a pensar que este sistema es un candidato a sistema de tipo Algol, presentando cambios drásticos y que podría convertirse en un sistema cataclísmico en el futuro. Finalmente, actividad en forma de erupciones en rayos X es probable que suceda en este sistema.

Presentamos espectros con un cubrimiento amplio en el rango (3-500) keV y curvas de luz en rayos X y óptico obtenidas con el satélite *INTEGRAL* del sistema transitorio, candidato a agujero negro y fuente de jets relativistas, GRO J1655–40. Nuestro análisis cubre cinco observaciones de la erupción que comenzó en febrero de 2005. Hemos hallado que la emisión de alta energía de GRO J1655–40 es descrita por una ley de potencias plana

y sin cortes exponenciales (con índices de fotones de 1.72±0.03,2.21±0.04 para la primera y la segunda observación, respectivamente). Éstas corresponden a los estados *low/hard* y *high/soft*, respectivamente. Al contrario que en los espectros de muchos otros candidatos a agujero negro, complejidad espectral en forma de corte exponencial en el espectro no es necesaria en la descripción del estado *low/hard*, contrariamente a lo que se esperaba. En este estudio mostramos por primera vez que los procesos de Comptonización no térmica son los dominantes en la emisión de alta energía también durante el estado *low/hard*. Finalmente, discutimos nuestros resultados en el contexto de los modelos utilizados para la emisión de alta energía y de los flujos de acreción en los sistemas con agujero negro.

Finalmente, presentamos observaciones simultáneas realizadas con los satélites *INTEGRAL* y *XMM-Newton* del candidato a agujero negro y fuente de jets relativistas GX 339–4. El análisis cubre 5 y 3 observaciones con los satélites *INTEGRAL* y *XMM-Newton*, respectivamente, de la explosión que comenzó en noviembre de 2006 y fueron realizadas entre enero y marzo de 2007. En este estudio hemos encontrado que durante la primera época de las observaciones la fuente se hallaba en el denominado estado *low/hard* y que la mejor descripción de su espectro en el rango de energia $E \leq 300\,\mathrm{keV}$ es una distribución de fotones descrita por una ley de potencias con un corte exponencial a energía $66\pm2\,\mathrm{keV}$. Utilizando el modelo de Comptonización EQPAIR, hemos podido determinar que la corona presenta una geometría compacta con una distribución de electrones relativista, compatible con *la emisión por un jet*. Hemos detectado transiciones espectrales rápidas entre estados *hard* y *soft intermediate*, con una correlación positiva entre la reaparición de la línea relativista del $\mathrm{Fe\,K_\alpha}$ (y reflexión) y el endurecimento del espectro en la época 3 (al contrario que en el espectro de la época 2, más blando). Esto último sería consistente con la aparición/desaparición de la fuente primaria de alta energía (*jet?*) en la transición entre estos estados. Todos los resultados que hemos obtenido han sido discutidos en el contexto de procesos de emisión en rayos X y transiciones entre estados en sistemas constituídos por agujeros negros de masas estelares.

# Chapter 1

# Introduction: High-energy astrophysics with INTEGRAL

We introduce this thesis by showing important points regarding the *INTEGRAL* satellite and the high-energy emission originating in X-ray Binary systems. First and foremost, in Section 1.1 a brief history of the high-energy missions is presented. This is important in order to understand the context in which *INTEGRAL* was planned as a new mission to supersede them. We thus, in Section 1.2, continue with a description of *INTEGRAL*, on-board instruments and on-ground segment as well. Finally, in Section 1.3.2, we describe the different emission processes taking place in X-ray Binaries in the X-$\gamma$-ray domain.

## 1.1 Historical summary of high-energy missions

Gamma-ray astronomy is a recent science with no more than $\approx$40 years of history. As shown below, through the 1960s, 70s, 80s, and 90s the sensitivity increase of the detectors was essential in its development. The detection of hard X-rays and/or $\gamma$-rays (E$\gtrsim$100 keV) is a hard task, which involves development of new techniques, different of that used in X-ray astronomy. The history of the $\gamma$-ray astronomy is the history of the high-energy astrophysics satellites as well, due to the fact that radiation in this energy range does not reach the surface of the Earth. In particular, high-energy detection in the energy range (100 keV–10 MeV) is only possible from high altitudes (h$\gtrsim$40 km), with balloons, airplanes, rockets and satellites. Nevertheless, the most important high-energy missions are satellites, due to their height, stability and duration of the missions.

Now, with the *INTEGRAL* satellite, the ability to localize the incident $\gamma$-rays has developed enormously and it is possible to make high-resolution spectroscopy and imaging studies. The *INTEGRAL* satellite (as described in Section 1.2) observes the sky

at hard X and $\gamma$-rays, at energies up to $\approx$10 MeV. As shown in the following, INTEGRAL supersedes earlier works by the Compton Gamma-Ray Observatory (*CGRO*), both in angular/spectral resolution and sensitivity. With CGRO it was possible to make the first complete systematic sky survey, and was considered the milestone mission of the golden age decade (1990s) in the $\gamma$-ray astronomy. In the following, we present a summary of the high-energy missions previous to *INTEGRAL* together with their most relevant achievements.

### 1.1.1 Introduction and early history of gamma-ray astronomy

The discovery of cosmic rays was made in 1912 by Hess (1913) and Kolhörster (1914) via ionisation rate measurements in air at different altitudes. At that time, the radiation was not called `cosmic radiation`, but `high-altitude radiation`. The term `cosmic rays` was introduced by Millican in the mid 1920s. At that time, the radiation was supposed to consist of $\gamma$-rays, which enter the atmosphere from outside and produce recoil-electrons in the atmosphere causing the measured ionisation. But, as it is currently known, this time period was not the hour of birth of $\gamma$-ray astronomy. Bothe & Kolhörster (1929) discovered the corpuscular nature of the `high-altitude radiation` by means of two Geiger-Müller counters in coincidence, and it was a still long time to go until the first cosmic rays were detected.

Previous studies (e.g. Morrison (1958)) were too optimistic and overestimated the $\gamma$-ray fluxes from celestial objects (solar flares, Crab nebula and radio galaxies). As the consequence, the first experiments were too simple and had not enough sensitivity. As it is currently known, $\gamma$-ray fluxes from celestial objects are extremely weak and this is the main reason why $\gamma$-ray astronomy is such a difficult research field, and why it took so long to really explore this field. Sophisticated massive and large area instruments were absolutely mandatory.

### 1.1.2 High-energy satellite missions

**EXPLORER XI** *(100 MeV–1 GeV)*

Explorer XI was launched in 1961 and was designed to measure high-energy radiation above 100 MeV. It did the first real cosmic $\gamma$-ray detection from space and Earth atmosphere (Kraushaar et al., 1965) (i.e. 31 cosmic rays were detected).

**ERS-18** *(10 keV–10 MeV)*

Launched in 1967, it did the first detection of a solar flare in the $\gamma$-ray continuum.

**OSO-3** *(30 MeV–1 GeV)*

It was launched in 1967 and, as Explorer XI, it was designed to measure high-energy radiation above 50 or 100 MeV. 621 cosmic $\gamma$-rays at E > 100 keV were detected and its results clearly showed evidence for $\gamma$-ray emission from the Milky Way.

**Vela** *(100 keV–1 MeV)*

Launched in 1969, the Network of Vela Satellites of the US Department of Defence was designed to monitor nuclear tests in the atmosphere after the Nuclear Test Ban Treaty of 1963. In 1967 the cosmic $\gamma$-ray bursts were discovered and published later by Klebesadel et al. (1973). The origin of these phenomena was a puzzle for another 25 years.

**SAS-II** *(10 MeV–500 MeV)*

Launched in 1972, it was designed to measure high-energy radiation above 30 MeV. This satellite discovered a diffuse $\gamma$-ray background, made first $\gamma$-ray images of parts of the sky and the discovered Geminga, which remained unidentified for another 20 years (finally identified as a pulsar).

**OSO-7** *(200 keV–20 MeV)*

Launched in 1972, it did the first detection of solar flare $\gamma$-ray lines (flare of August 4, 1972). Apart from the continuum emission, four lines were clearly detected: the anihilation line at 511 keV, the 2.2 MeV neutron capture line, and nuclear interaction lines at 4.4 and 6.1 MeV from excitations of Carbon and Oxygen nuclei.

**COS-B** *(100 MeV–1 GeV)*

Launched in 1975, this satellite, the first high-energy mission from ESA, produced the first detailed map of the sky at $\gamma$-ray wavelengths. The $\gamma$-ray sky was found to be dominated by diffuse emission from the Galactic Plane, which at the highest energies (E > 100 MeV) is the decay of neutral pions generated in the collision of cosmic rays with interstellar gas. Together with SAS-II, the two missions provided the first real source detections. The strongest source features were found from the Crab, Vela and Geminga. The COS-B source catalog contained a total of 25 objects, of which only one (3C 273) was extragalactic.

**HEAO-3** *(20 keV–10 MeV)*

Launched in 1979, it supposed a milestone of the $\gamma$-ray line spectroscopy. It did the first detection of a nucleosynthetic line: the 1 809 MeV line from radioactive $^{26}$Al, which was discovered from the direction of the Galactic Center region (Mahoney et al., 1984). It did also the first measurement of the line profile of the 511 keV line from the Galactic Center region.

**SMM** *(500 keV–10 MeV)*

Launched in 1981, it provided a wealth of information of solar flare $\gamma$-ray emission in lines and continuum up to 10 MeV. In addition, it also made important studies of cosmic $\gamma$-ray lines, e.g. 511 keV anihilation line, the 1 809 MeV $^{26}$Al line and detection of nucleosynthesis lines from $^{56}$Co decay in SN 1987a in the Large Magellanic Cloud (Leising & Share, 1990).

**SIGMA** *(10 keV–1 MeV)*

Launched in 1989, it did the first high-resolution images (13' resolution) of the sky regions in the hard X-ray/soft-$\gamma$-ray (E$\approx$100 keV) range. It mainly observed the Galactic Center region, where it detected about 30 sources, showing a great variety of objects, i.e. X-ray novae and others (Vargas et al., 1997).

**Compton** *(10 keV–100 GeV)*

Launched in 1991, the satellite carried four major experiments (COMPTEL, EGRET, BATSE and OSSE), which greatly improved the spatial and temporal resolution of $\gamma$-ray observations. The Compton Gamma Ray Observatory (CGRO) ceased operation in June 2000, and was de-orbited by NASA. This satellite, in operation during 9 years, established the role of $\gamma$-ray astronomy as an important branch of astronomy and astrophysics, in general. Thanks to CGRO $\gamma$-ray astronomy became an integrated part of the astronomy. Highlights of the Compton mission are specially the all-sky maps in the continuum and line emission. In the field of $\gamma$-ray bursts, BATSE measured the locations, energy spectra and time profiles of more than 2 500 individual bursts.

**BEPPO-SAX** *(1 keV-500 keV)*

Launched in 1997, it succeeded in observing X-ray afterglows of a few burst

sources (Costa et al., 1997). The subsequent observations of these objects at optical – and in a few cases also radio wavelengths – clearly established the extragalactic origin of the $\gamma$-ray burst sources.

## 1.2 The INTEGRAL mission

The INTErnational Gamma-Ray Astrophysics Laboratory (INTEGRAL; Winkler et al. 2003), is a medium-sized mission of the European Space Agency (ESA). The purpose of this satellite is to provide high resolution imaging and spectroscopy of the X and $\gamma$-ray sky, as a continuation of the *Compton* and *SIGMA* missions (see Section 1.1). This mission belonged to the ESA's so called *Horizon 2000* programme. It was successfully launched on October 17 2002 by a Russian ПРОТОН (i.e. PROTON in English) rocket from the Baikonour Space Centre in Kazakhztan.

Four scientific instruments were integrated on-board the spacecraft. All together cover a large range of the electromagnetic spectrum from the optical to the $\gamma$-ray band. Their goal is to study the different physical processes producing emission at high energies. The two main instruments (IBIS and SPI) have been specifically designed to observe in the hard X-ray and $\gamma$-ray ranges with fine spatial and spectroscopic resolutions.

The main targets for this space observatory are $\gamma$-ray sources, either point or diffuse sources, present mainly in our galaxy, but also sometimes in extragalactic fields. Another topic of interest for INTEGRAL are the regions where stellar nucleosynthesis takes place.

In this Section, both the spacecraft and the ground segment are introduced. Thereafter, short descriptions of each of the instruments plus a brief introduction of the coded-mask technique are presented as well.

### 1.2.1 The spacecraft

The spacecraft (S/C) is made of two big structures. At the bottom, the service module supports the technical systems (e.g. the thermal, attitude and electrical control ones). The INTEGRAL Radiation Environment Monitor (IREM), whose goal is to monitor the radiation activity around the satellite, is also mounted on the service module and, in case of an increase of such radiation, an alert is sent to the instruments. The service module is also the place to which solar panels are fixed. In the upper the payload module is located. It consists of the four instruments, plus the star trackers and associated thermal control hardware (see Figure 1.1).

The S/C flies around the Earth in an elliptical orbit lasting 3 days. An eccentric orbit was chosen to make sure that the S/C spends most of its time far away from the disturbing electronic and hadronic belts located high above the Earth surface. When the

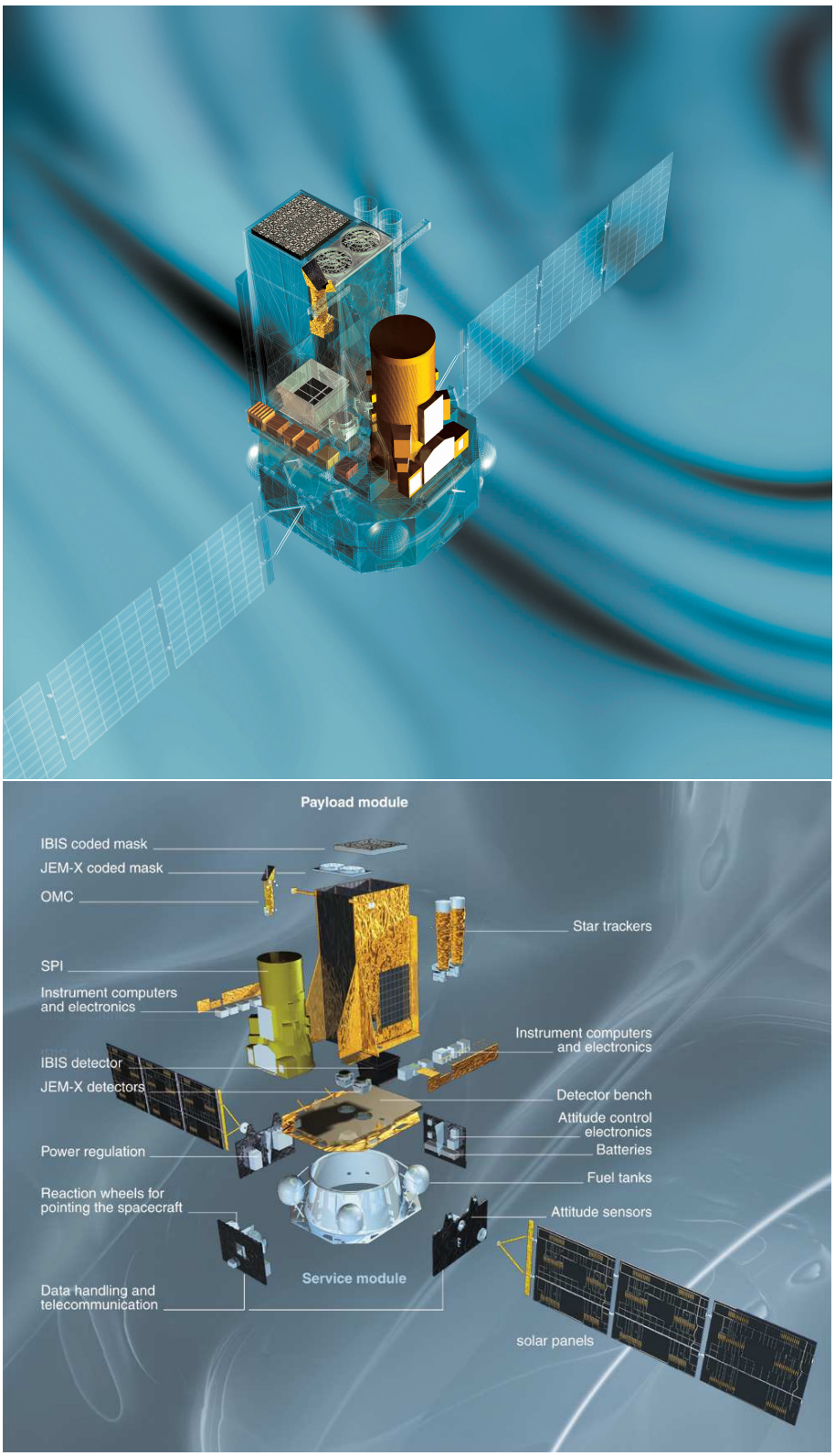


**Figure 1.1**: INTEGRAL's instruments seen through the transparent structure of the spacecraft (top). An exploded view of the INTEGRAL spacecraft showing all its instruments and other components (bottom). Credits: ESA.

S/C crosses the belts, the high energy instruments must be turned off, because they interact with the particles causing an increase of the detected background activity and possible damage to the detectors. Every revolution, the satellite orbits the Earth at a perigee distance of 9 000 km and retraits until it reaches an apogee of 160 000 km. Therefore, the detectors can perform long exposure observations without interruptions for nearly 3 days: almost 90% of the revolution can be dedicated to scientific observations. During the rest of the time the detectors are put in safe mode to ensure that they will not be damaged when crossing the vicinity of the Earth and its radiation belts.

### 1.2.2 The ground segment

Two stations ensure the satellite tracking: Redu in Belgium and Goldstone in California. Hence, the whole orbit is covered. The telemetry packets are then sent to the Mission Operation Centre (MOC) located at Darmstadt (Germany).

The INTEGRAL ground segment is divided in two parts: the S/C operations and the science. The INTEGRAL Science Operation Centre (ISOC) (located at ESAC, near Madrid) is in charge of managing the calls for proposals and of providing the observation plans to the MOC.

The INTEGRAL Science Data Centre (ISDC) (located at Versoix, near Geneva) receives the telemetry data and process them before releasing the processed data to the community. An archive of all the data is maintained at the ISDC. The ISDC also provides the Offline Science Analysis (OSA) package that allows an interactive analysis of the INTEGRAL data by the scientific community.

### 1.2.3 The instruments on-board INTEGRAL

The four instruments on-board INTEGRAL are:

- The hard X-ray and $\gamma$-ray imager IBIS (Ubertini et al., 2003) which works in the 15 keV to 10 MeV energy range and has got two detection layers:
  - ISGRI (Lebrun et al., 2003) for the 15 keV to 1 MeV energy band;
  - PICsIT (Labanti et al., 2003) for the 200 keV to the 10 MeV energy band;
- The hard X-ray and $\gamma$-ray spectrometer SPI (Vedrenne et al., 2003) which goes from 20 keV to 8 MeV;
- The X-ray monitor JEM-X (Lund et al., 2003) that covers the 3-30 keV energy range and
- The optical monitoring camera OMC (Mas-Hesse et al., 2003) performing photometry using a Johnson V filter ($\approx$550 nm).

All these insruments offer a full coverage in the high energy band from X-rays to $\gamma$-rays (i.e. 3 keV to 10 MeV), and optical in the V band ($\lambda = 5\,500$ Å). They all point in the same direction and are simultaneously operated.

The main characteristic of the three high energy detectors is that they are based on *coded-mask* detectors. Indeed, focusing high energy photons remains a difficult task. The incident X or $\gamma$-ray photons tend to either be absorbed by the optics built to focus them or to cross it, but they are usually not reflected. Therefore, the common technique based on gathering all the photons at a focal plane where the detector is located (e.g. as XMM-Newton works [1]) was discarded during the design of the instruments. Instead of this, masks with specific patterns were placed in front of each detector. The photons coming from a given source in the field of view of the instrument are distributed on the detector following the pattern of the coded-mask and the position of the source. Afterwards, the sky image can be reconstructed provided the mask pattern was carefully chosen (in a so called *deconvolution* process). In the deconvolution process, the shadowgram – i.e. the image of both the source and the background through the detector – is deconvolved or solved (Skinner & Connell, 2003). This technique allows to create images of the sky in hard X and $\gamma$-rays. One advantage of this technique is that both the source and the background are measured simultaneously. The other main advantage is the significantly wider FOV, as its size is of the order of degrees, while classical X-ray telescopes (as XMM-Newton) are limited in FOV to a few arc-minutes.

Another important property of coded masks is that their FOV can be divided into two regions: the fully-coded and the partially-coded field of view (FCFOV and PCFOV, respectively). These two regions are defined as the zones for which the source modulated by the mask totally illuminates the detector plane (FCFOV) or only part of the detector plane is covered by the shadow (PCFOV). The significance being higher when the source is located within the FCFOV. A way to increase the size of the FCFOV is to build a mask larger than the detector. The inconvenience of this method based on masks with a repeated geometry is that sources located within the PCFOV produce non-perfect coded shadowgrams, so it provides ghost peaks in the images that must be elliminated during the deconvolution process.

**The imager IBIS**

IBIS stands for Imager on Board (the) INTEGRAL Satellite. It is a $\gamma$-ray telescope designed to obtain images with a high angular resolution. It operates in the 15 keV to 10 MeV energy range. It is made of two detector layers behind a coded mask made of Tungsten. The mask is formed by the coded pattern plus the structure that sustains it.

[1] XMM-Newton is the acronym of X-ray Multi-Mirror mission. This is an ESA X-ray mission, which works in the energy range of $0.1 - 10$ keV.

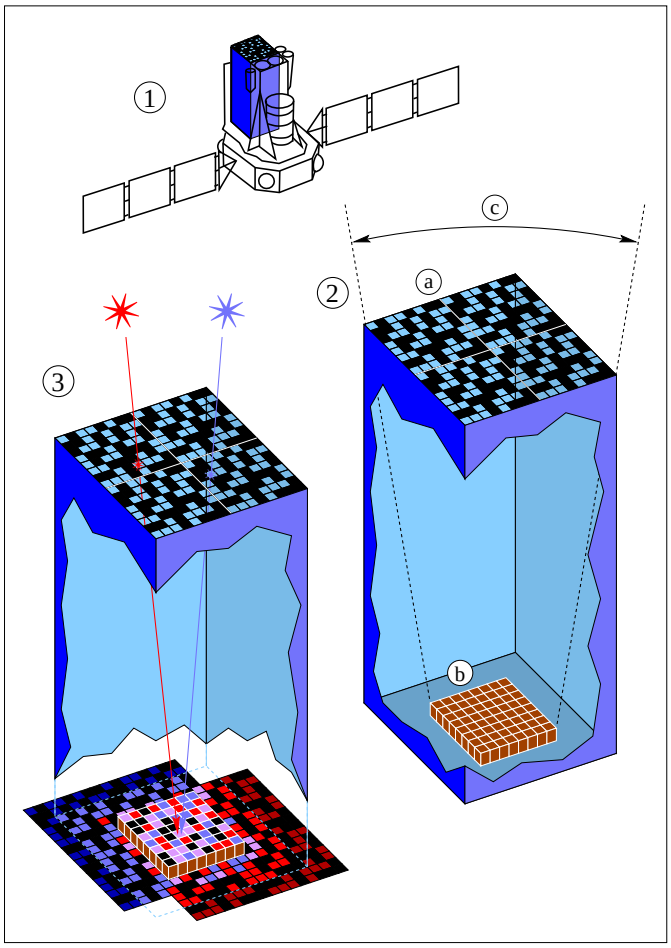


**Figure 1.2**: Schematic illustration of coded mask imaging. The image shows a simplified section of the IBIS imager on-board INTEGRAL. The coded mask partially covers the opening of the telescope. It is made of opaque plates and holes optimally distributed. The detector records the shadow of the mask projected by the gamma-ray sources located within the field of view. Figure shows, in the case of two sources, the superposition of the shadows of the mask onto the detector. Credits: ISDC.

Its angular resolution depends only on the size of the mask element (c = 11.2 mm) and on the distance between the mask and the detector plane (H = 3 133 mm), so the angular accuracy achieved is:

$$d\theta = \arctan(c/H) = 12' \tag{1.1}$$

This is the size of the point-spread function (PSF) used when decoding the images, but IBIS can determine the position of a $\gamma$-ray source with an accuracy of $\approx$2 arcmin. The mask is a parallelipipede of $1\,064\times1\,064\times16\,mm^3$, with $95\times95$ individual cells. Half of them are opaque in the IBIS energy range. The choice of the mask is based on a cyclic replication array called Multiple Uniformly Redundant Array (MURA). Between the mask and the detectors, there is a collimator made of a passive material that blocks as much as possible the high energy diffuse background emission entering from the lateral sides. The collimator is opaque up to 200 keV. The FOV achieved for IBIS is of $29^\circ\times29^\circ$ square ($8.3^\circ\times8^\circ$ for the FCFOV).

The top detector is the INTEGRAL Soft Gamma-Ray Imager, ISGRI, that operates from 15 keV up to approximately 1 MeV. It is an array of $128\times128$ independent pixels made of Cadmium-Telluride (CdTe) crystals.

The bottom detector is the Pixellated Imaging Caesium Iodide Telescope, PICsIT, that operates from approximately 200 keV up to 10 MeV. It is composed of Caesium-Iodide (CsI) scintillator crystals divided in an array of $64\times64$ pixels.

The two detector layers are completely surrounded on five sides (bottom+4 lateral sides) by an anti-coincidence VETO system. This shielding system is made of Bismuth Germanat (BGO) crystals. Its goal is to reduce the background by rejecting those events detected by the instruments due to cosmic particles or local environment radiation having entered outside the FOV.

The normal ISGRI science mode records each event, (i.e. each photon absorbed in one crystal), and tags it with the (X,Y) position of the detection pixel in the detector plane, the energy deposited in that pixel and the event time.

While the possibility to record each event exists also for PICsIT, this procedure is not used because of the higher background influence. Instead, the PICsIT standard mode is to accumulate images and spectra for 30 minutes and to download them as histograms. The time resolution of PICsIT is thus 30 minutes. Eventually, because PICsIT sensitivity is not high enough to create a good image for a single Science Window, it is expected to obtain good results only if INTEGRAL is in staring mode (and the source is really bright).

**Figure 1.3**: IBIS detectors (top) and coded mask (bottom). Credits: ESA.

### The spectrometer SPI

The SPectrometer on-board the INTEGRAL satellite, SPI, is the main instrument for high-resolution spectroscopy at hard X and $\gamma$-ray energies. Its spectral range goes from 20 keV up to 10 MeV. It also provides low-angular resolution images.

The instrument is made of three main parts: a coded mask, an array of detectors and a shield. The coded mask is made of Tungsten and has an hexagonal geometry. The elements are 60 mm large, and 50% of them are transparent. They are distributed in a 120° rotated symmetric pattern. The mask is located 1 710 mm in front of the detector plane, so the angular resolution is ≈2.8° (see Equation 1.1). The detector is a hexagonal array of 19 high purity Germanium crystals. Two of these detectors are currently dead: #2 and #17, so the effective area and the sensitivity are slightly reduced. In order to minimize the radiation damage on detectors and to bring them back to their nominal state, an annealing is needed every 6-12 months to recuperate perfect crystals. Due to high background contamination, an Anti-Coincidence Shield (ACS) made of BGO crystals sourrounds the detector array and detects all events coming from outside the observed FOV. Its size defines the wide field of view with a diameter of 35° (16° for the FCFOV).

SPI has only one operating mode: a photon-by-photon counting mode with a high-temporal resolution. All information for each photon (not coincident with an ACS event) is transmitted to the ground station. The event type can be either:

- a single event (i.e. detected in one detector); or
- a multiple event (i.e. when the incident photon is Compton scattered and deposits its energy in different locations, within the same detector or different ones.)

As there are few detectors, many pointings are needed in order to reconstruct the image. Therefore, a dithering strategy is adopted; the satellite observes the same field but with a slight offset for each pointing. This also allows a better average (and thus reduction) of the background. Background is an important issue in $\gamma$-ray domain, since fluxes from astrophysical sources in this energy range are very weak.

### The X-ray monitor JEM-X

The Joint European Monitor for X-rays, JEM-X, is designed to complement the observations taken with the two main instruments described above, thus extending the energy range down to 3 keV. JEM-X can also observe sources with steep spectra that would be well beyond the detection limits of IBIS and SPI.

The instrument consists of two identical coded-mask telescopes co-aligned with the other instruments on-board INTEGRAL. Each JEM-X unit is made of three parts: the

**Figure 1.4**: SPI detectors (top) and coded mask (bottom). Credits: ESA and CESR.

coded mask at the top, the detector, and the electronics at the bottom. The detector is a microstrip gas chamber where incident photons are absorbed by photo-electric processes and the resulting ionization is amplified towards the strip anodes using high voltages. The collimator structure, joining the mask and the detector, fixes the diameter of the FOV to 13°.2 (4°.8 for the FCFOV) and helps to reduce the background contamination. The mask pattern is based on an hexagonal uniformly redundant array. Only 25% of the cells are transparent. This value is a compromise between a better sensitivity and telemetry allocation constraints. The distance between the mask and the detector of 3 400 mm and the cell size of 3.3 mm determine the angular resolution of 3' (see Equation 1.1).

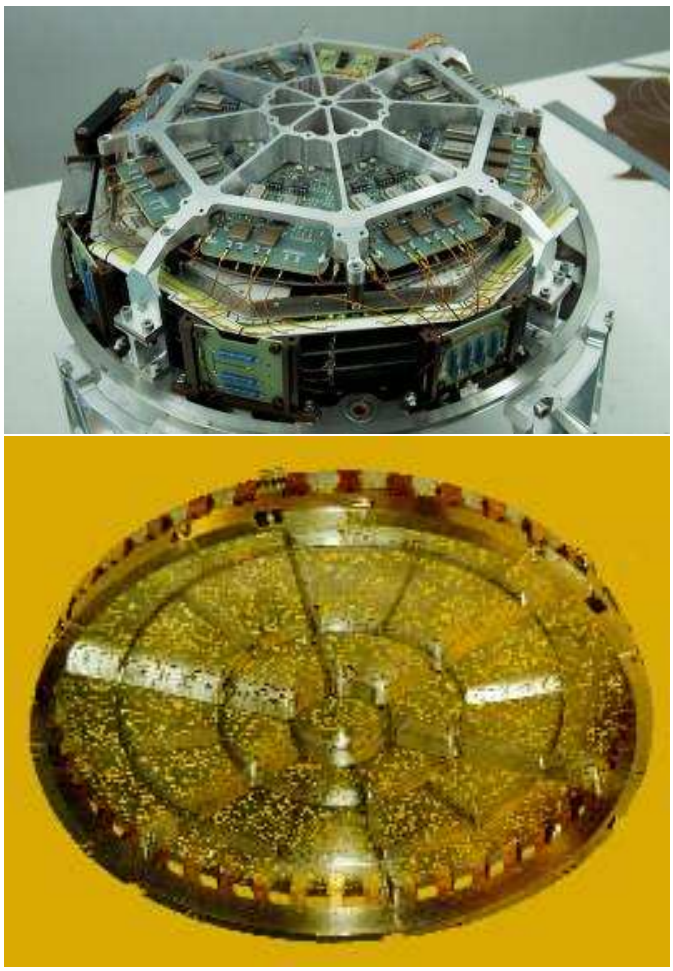

**Figure 1.5**: JEM-X detector (top) and coded mask (bottom). Credits: DSRI.

After the mission started, important degradations of the anodes due to interaction with cosmic rays were noted. Consequently, only one unit is operated at a time. At the beginning of the mission, JEM-X1 was turned off and since revolution 170 it is JEM-X2 that is not operational. The high voltage used after the launch is also reduced to protect the detectors, and this results in a loss of sensitivity.

### The optical monitor OMC

The optical monitoring camera, OMC, is a wide-field telescope using a $1\,056 \times 2\,061$ pixels CCD detector. It is co-aligned with the high energy instruments. The optical system consists of a set of refractive lenses and a Johnson V filter ($\lambda = 5\,500\,\text{Å}$). The astrometric resolution is better than $1''$ and performs optical photometry in the V band down to

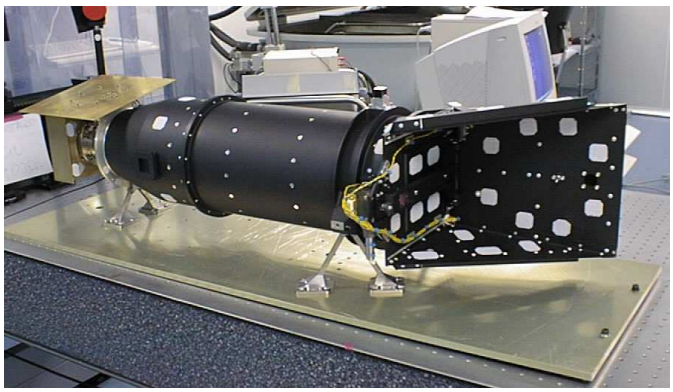

**Figure 1.6**: OMC flight model (w/o MLI). Credits: INTA.

18th magnitude. It has a square FOV of 4°.979×4°.979, but only small fractions of it are transmitted to the ground due to telemetry restrictions. In fact, the normal science operation mode consists of a selection of windows of 11×11 pixels (3.2'×3.2') around known sources within the FOV that are observed during short exposures (i.e. 10, 50 and 200 s). Reference stars, high energy sources and good-photometric candidates (see Chapter 2 for more details) are good targets for OMC, and are observed in consecutive shots. Another fast monitoring mode is used when highly fast variable targets are expected in the FOV. In this fast mode, the integration time is ≈3 s.

## 1.3 X-ray Binaries

The discovery of the first X-ray binary in the early 1960's, Sco X-1 by Giacconi et al. (1962), constituted the beginning of the X-ray astronomy. At the time of its discovery the physical processes which could explain the observed X-ray flux of the source were unknown. After the identification of the optical counterpart of Sco X-1 by Sandage et al. (1966), mass transfer in a close binary system was discussed as a possible mechanism to understand the enormous X-ray energy release detected from the source.

Since then, the number of discoveries of X-ray binaries has been growing steadily, in parallel to the evolution of the X-ray telescopes. Up to now about 824 X-ray binaries are known (Liu et al. 2000, 2001; Bird et al. 2007). In general an X-ray binary consists of a compact object and a mass donating companion star, orbiting around their common center of mass. The compact object can be either a white dwarf (so called cataclysmic variables; CV), a neutron star or a black hole (so-called black hole candidates; BHC). Meanwhile the companion star can be either a low-mass ($\leq$10 $M_\odot$, later than type A or even a white dwarf in very evolved systems) or a high-mass star ($\geq$10 $M_\odot$, with O, B or Be types), leading to the classification of the binary system into two main classes: Low

Mass X-ray Binaries (LMXB) or High Mass X-ray Binaries (HMXB).

The luminosity, temporal and spectral behaviour of an X-ray binary depends mainly on: the mass of the optical counterpart, the mass accretion rate, the geometry of the accretion flow from the companion and the type of the compact object. If the compact object is a neutron star, then the strength and geometry of its magnetic field plays an important role in the X-ray emission.

In Chapters 4 and 5 of this thesis, I focus on the study of the high-energy emission of the X-ray binaries GRO J1655–40 and GX 339–4, both containing a black hole and classified as LMXB (see Sections 4.2 and 5.1 for introductions to these sources). We summarize in this Section the different possible accretion scenarios and the radiation processes involved in order to understand their high-energy emission.

### 1.3.1 Mass Accretion in X-ray Binaries

The accretion process is a transfer of mass from the companion star to the compact object. This process depends basically on the spectral type, the mass of the companion star and the orbital separation of the binary system. In this section, the basic accretion mechanisms are described.

All accretion mechanisms have in common that the gravitational energy is the driving force for accretion, thus the shape and structure of the gravitational potential in a binary system have to be taken into account. The theoretical description of the gravitational potential in a binary system is founded in the studies of the French mathematician Eduard Albert Roche (1820-1883). The gravitational potential, known as Roche potential, of two point masses $M_1$ and $M_2$ in a circular Keplerian orbit around their center of mass, takes the following form in the corotating frame of reference (Frank et al., 2002):

$$\Phi(r) = -\frac{GM_1}{\mid \vec{r} - \vec{r_1} \mid} - \frac{GM_1}{\mid \vec{r} - \vec{r_2} \mid} - \frac{1}{2}(\vec{\omega}\times\vec{r})^2 \tag{1.2}$$

where $\vec{r_1}$ and $\vec{r_2}$ are the position vectors of the center of the two stars and $\vec{\omega}$ is the angular velocity of the binary system. The first two terms in the equation represent the gravitational potential of each component and the last term the influence of the centrifugal force.

The equipotential surface within which a mass element is bound to one of the components of the system is known as Roche lobe (Figure 1.7). The shape of the Roche lobe depends on the orbital separation and its size is given by the mass ratio $q = M_1/M_2$. The equilibrium points, where the total gravitational force vanishes, are called Lagrangian points ($L_1$-$L_5$). If material from the donor star reaches the saddle point $L_1$ possessing momentum in the outward direction, it can enter the Roche lobe of the compact object. A similar mass transfer can happen for matter crossing $L_2$ point inwards. We summarize here the two main mechanisms known by which such a mass transfer can proceed:

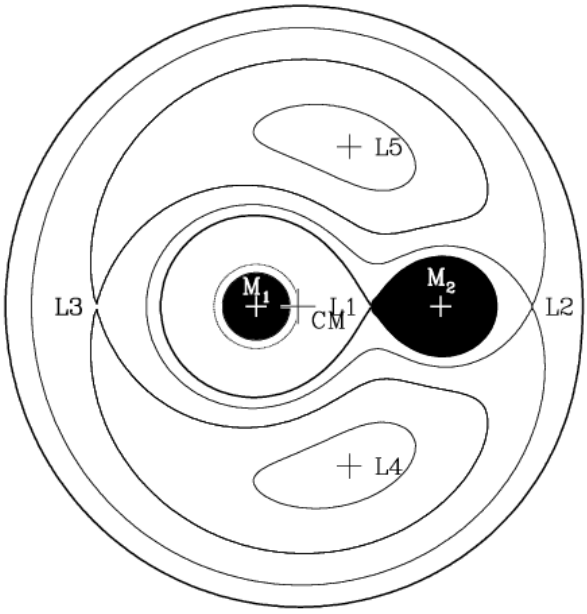


**Figure 1.7**: Schematic illustration of Roche lobe equipotential surfaces in the orbital plane for a system with $M_1 \gtrsim M_2$.

- Roche lobe accretion: during the evolutionary process of the donor star, its size can change several times, reaching and exceeding the size of its Roche lobe and starting an overflow of matter through the inner $L_1$ point. This mechanism is active mainly for low-mass, i.e., late-type stars.

- Stellar wind accretion: one of the two stars, at some evolutionary phase, eject mass in the form of a stellar wind into the Roche lobe of the compact object. This mass transfer can be either directly via $L_1$ or the stellar wind may loose its kinetic and angular momentum in the neighbourhood of $L_2$. This process is common of early type stars.

On the other hand, the accretion rate can not increase indefinitely since the rate is controlled by the outward momentum transferred from the radiation to the accreting material by scattering and absorption. For a steady and symmetric accretion model (see Frank et al. 2002), in which the accreted material is fully ionized hydrogen, the radiation exerts a force mainly on the free electrons through Thomson scattering. Then, the luminosity (and the rate) can not exceed an upper limit, given when the gravitational attraction balances the outward force on the accreting material due to Thomson scattering. The maximum luminosity, known as Eddington luminosity, is given by:

$$L_{edd} = \frac{4\pi G M_X m_p c}{\sigma_T} = 1.3{\times}10^{38} \frac{M_X}{M_\odot}\, erg\, s^{-1} \tag{1.3}$$

where $\sigma_T$ is the Thomson scattering cross-section, $M_X$ is the mass of the compact object and $m_p$ the proton mass. For higher luminosity than the Eddington luminosity the outward pressure of radiation exceeds the inward gravitational attraction and the accretion would be halted. In the case that all the gravitational energy is converted to luminosity, the maximum accretion rate is:

$$\dot{M}_{edd} = 1.5{\times}10^{-8} \frac{R}{10\,\mathrm{km}} M_\odot \mathrm{yr}^{-1} \tag{1.4}$$

Generally, the observed X-ray luminosity of X-ray binaries is lower than the Eddington limit. However, there are sources whose luminosity is higher than the Eddington limit. This is not in contradiction with the theory, since the Eddington limit is only valid for the case of spherical symmetric accretion. Super-Eddington accretion is possible when the radiation field and matter inflow are not isotropic.

#### 1.3.1.1 Geometry of the accretion flow

The geometry of the accretion flow is mainly determined by the angular momentum per specific mass of the accretion flow. For a neutron star, its magnetic field plays an important role in the geometry of the accretion flow in the nearby regions of the compact object [2]. In this Section the basic known geometries of the accretion flow in black holes are summarized:

- **Accretion disk**: the transferring material or accretion stream, from the donor star to the compact object, carries angular momentum so it can not be directly accreted by the compact object. Instead the material follows Keplerian trajectories around the compact object until the stream intercepts itself, forming a ring like structure (see Figure 1.8). The radius of this ring, known as circularization radius, depends on the angular momentum and initial energy of the accretion stream. Applying Kepler's third law, the circularization radius can be written in terms of the mass ratio $q$ and the orbital separation $a$ as follows (Frank et al., 2002):

$$r_{circ} = (1+q)[0.500 - 0.277 \log q]^4 a \tag{1.5}$$

[2] Recently, in an study of absorption lines in X-rays of the black hole GRO J1655–40, weak magnetic field has been found to play an important role for the accretion in the vicinity of the black hole (Miller et al, 2006). The magnetic activity is thought to arise from the hydrodinamic magneto-rotational-instability model (Hawley et al., 2001). This arised as an alternative to the $\alpha$ disk model of Shakura & Sunyaev (1973), which lacks of any influence from magnetic fields.

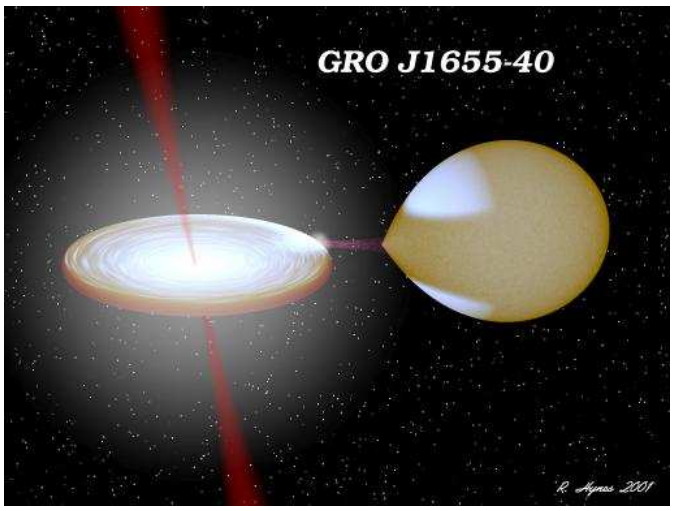


**Figure 1.8**: Schematic illustration of of the accretion disk in the orbital plane for a LMXB. Credits: R. Hynes.

Finally, the ring starts to spread under the influence of dissipative processes, like, e.g., viscous interaction or shock waves within the plasma of the ring. These dissipation processes are known as viscosity processes. Thus, the gas lose energy and starts to move inwards toward the compact object. Because the total angular momentum has to be conserved, and without an external angular momentum sink (e.g. magnetic field), material has to spread outwards at the same time (Frank et al., 2002), forming a flat accretion disk.

The modern standard theory of accretion disk ($\alpha$ disk) was published in a pioneering work in the early 1970s by Shakura & Sunyaev (1973). They suggested turbulent motion of the gas as a mechanism for angular momentum transport. However, such a mechanism could not explain – using two dimensional hydrodinamics alone – the large accretion rates and released energy observed in the X-ray binaries. The mechanisms that allow a sufficiently effective momentum transport are still debated. One of the most promising possibilities is turbulence in the accretion flow by weak magnetic fields (also called magneto-rotational instability (MRI) model; Hawley et al. 2001).

- **Accretion Disk Coronae**: several observations of accreting X-ray binaries indicate the presence of a diffuse low density corona in the upper and lower sides of the accretion disk. The main physical parameters defining te corona are its optical depth and its average electron temperature. There are several models to explain the origin of such corona like, e.g.: corona which evolve from external irradiation of the accretion disk by the central object (Dove et al., 1997) or which evolve from the

internal dynamic structure of the disk (Miller & Stone, 2000).

### 1.3.2 High-energy emission from X-ray Binary systems

One of the key targets of INTEGRAL are X-ray emitting binary systems. Their observed X-ray spectra are consequence of different radiation processes that take place at different emission regions of the binary system. For instance, thermal blackbody radiation from the accretion disk, photoelectric absorption from the outer and cooler regions, fluorescence lines from inner parts of the accretion disk and inverse Compton scattering from optically thick disk corona. A detailed review of the radiation processes in X-ray Binaries can be found in the PhD-Thesis of Kuster (2004).

In this Section, radiation processes which are important in the analysis of our data are summarized.

#### 1.3.2.1 Thermal-Blackbody radiation

In the case of thermodynamical equilibrium with its environment at all wavelengths, matter radiates as a blackbody, i.e. is a perfect absorber and emitter of radiation. The spectrum emited by a blackbody depends on its temperature $T$ and follows Planck's law:

$$B_\nu(T) = \frac{2h}{c^2} \qquad \frac{\nu^3}{e^{\frac{h\nu}{kT}} - 1} \tag{1.6}$$

with the Boltzmann constant $k = 1.381 \times 10^{-15}\,\mathrm{erg\,K^{-1}}$ and the Planck constant $h = 6.626 \times 10^{-27}\,\mathrm{erg\,s^{-1}}$.

Thermal radiation can be observed from plasma in thermodynamical equilibrium, as e.g., plasma in the accretion disk. The emitted spectrum of accretion disks can be explained as a superposition of several blackbody spectra at different temperatures (Mitsuda et al., 1984).

#### 1.3.2.2 Compton scattering

In the basic Compton scattering absorption process, a photon of energy $E$ collides with a stationary electron, transferring kinetic energy $T$ to the electron and thus reducing its own energy to $E'$, which is given by:

$$E' = \frac{E}{1 + \frac{E}{m_e c^2}(1 - cos\Theta)} \tag{1.7}$$

The differential cross section of this process is given by the Klein-Nishina formula (Klein & Nishina, 1929):

$$\frac{d\sigma_{KN}}{d\Omega} = \frac{3}{16\pi}\sigma_T \left(\frac{E'}{E}\right)^2 \left(\frac{E}{E'} + \frac{E'}{E} - sin^2\Theta\right) \tag{1.8}$$

For an ellastic collision ($E' = E$), the Klein-Nishina formula reduces to the Thomson scattering. For $E > 100\,\mathrm{keV}$ (X-ray and $\gamma$-ray photons), the cross section is highly dependent on $\Theta$. Then, the scattering is concentrated in forward direction due to the relativistic beaming.

In a plasma, Compton scattering from protons is suppressed by a factor of $(m_e/m_p)^2 \approx 10^{-7}$, as compared with electrons Compton scattering.

#### 1.3.2.3 Inverse Compton scattering

Up-scattering of photons of lower energy through collisions with energetic particles, mostly electrons, is called Inverse Compton Scattering.

In hot electrons plasmas like in accretion disk or accretion disk coronae the assumption of stationary electron (Compton Scattering) fails, because the thermal motion of the electron plasma becomes important. Assuming a Maxwellian velocity distribution of the electrons and the non-relativistic limit $h\nu \ll m_e c^2$, the energy transfer per scattering is given by:

$$\frac{\Delta E}{E} = \frac{4kT_e - E}{m_e c^2} \tag{1.9}$$

where $T_e$ is the temperature of the electron plasma (Rybicki & Lightman, 1979). For incident photons with $E < 4kT_e$, the energy transfer to the photon is positive and the photon gains energy during the scattering.

Under real physical conditions, the photons are moving through a plasma cloud of optical depth $\tau_c$. Thus, their gain energy has to be multiplied by the average number of scatterings and is given by the Compton "y"-parameter:

$$\mathrm{y} = \frac{4kT_e}{m_e c^2} max(\tau_c, \tau_c^2) \tag{1.10}$$

The emerging spectrum of the Comptonized photons can be derived by describing the process as a difusion problem. For non-relativistic electrons and plasmas with larger optical depths ($\tau_c > 1$), the spectral distribution is described by the Kompaneets equation (Rybicki & Lightman, 1979). A derivation of the Comptonized photon spectrum from the Kompaneets equation can be found in Sunyaev & Titarchuk (1980). Extensions of this formalism to lower optical depths and relativistic temperatures have been presented by Titarchuk (1994) and Hua & Titarchuk (1995).

The Comptonized process described above is known as *thermal Comptonization* process, since the *electrons follow a Maxwellian distribution, i.e., have been thermalized*

*through collisions*. There is also a non-thermal Comptonization process, normally referred as *bulk-flow Comptonization*, in which the electrons are accelerated by free fall. As we will show in Chapters 4 and 5, non-thermal accelerating processes in the base of a jet are a good explanation for the high-energy emission observed of two known black holes (GRO J1655–40 and GX 399–4). In the base of the jet, at the vicinity of black holes and neutron stars, the electrons move at velocities which are a substantial fraction of the speed of light ($v_e > 0.5c$).

#### 1.3.2.4 Cyclotron and Synchrotron Radiation

An electron which is bound to a magnetic field and which has a velocity component parallel to the magnetic field, moves along a helix like path along the magnetic field lines. The force acting on the electron is the Lorentz force. According to classical electrodynamics an accelerated charge particle emits a narrow line of emission, called cyclotron emission.

In the case of hot electron plasma in astrophysical sources, the emission process due to the presence of non-uniform magnetic fields requires a relativistic treatment. This leads to the synchrotron radiation, that peaks at a frequency:

$$v_c = \frac{3}{2}\gamma^2 \frac{eB}{2\pi m_e sin\Theta} \tag{1.11}$$

where $\gamma$ is the Lorentz factor, $B$ is the magnetic field, $e$ the electron charge, $m_e$ the electron mass rest and $\Theta$ is the opening angle of the emission cone.

The corresponding single electron spectrum is not a single line as in the classical approach, and it is spread over a large frequency range. The spectrum of a larger number of electrons emitting synchrotron radiation, has the shape of a power law, under the assumption that the energy distribution of the electrons is non-thermal and follows a power law distribution as well (Rybicki & Lightman, 1979).

The energy of the synchrotron radiation is characterised by the strength of the magnetic field. Typical magnetic field strengths of neutron stars ($\approx 10^8 - 10^{12}$ G) will produce synchrotron radiation from the radio to the X-ray band.

In the case of very strong magnetic fields ($B > 10^{12}$ G, as occurring in neutron stars), the influence of quantum mechanics becomes important. The energy of the electron can not be considered as continuous but is quantized in discrete levels (Landau levels). The energy difference between two allowed eigenstates is called cyclotron energy. The de-excitation of excited electrons to their ground state leads to the emission of resonant photons (Harding & Daugherty, 1991). At the same time the cross-sections are resonant and multiple of the cyclotron energy. Therefore, the plasma is optically thick for these resonant photons, and they are scattered out of line of sight creating a cyclotron resonant scattering feature (CRSF) in the photon spectrum.

#### 1.3.2.5 Photoelectric Absorption

At low photon energies, i.e., when $h\nu \ll m_e c^2$, the dominant process by which photons are absorbed is the photoelectric absorption mainly by neutral H and He atoms. In this process the atomic electrons are removed from their nuclei by the X-ray and $\gamma$-ray photons, acquiring velocities proportional to the incident photon energy.

The photoelectric absorption depends mainly on the photon energy and the amount of material between the source and our telescope. Above 5 keV this process becomes important for hydrogen columns greater than $\approx 10^{23}$ atoms cm$^{-2}$.

#### 1.3.2.6 De-excitations of Atomic Nuclei

Atomic nuclei in excited states are produced in energetic collisions in interestellar space and the vicinity of compact objects. The de-excitation of atomic nuclei produces a photon of energy equal to the binding energy between the two nuclei atomic states, creating *fluorescence* lines in the photon spectrum. This is the mechanism known to produce the *relativistic broad* Fe K *lines* in black holes (Fabian et al., 1989) and, partially, responsible for the *reflection* features observed in black holes as well (George & Fabian, 1991) [3].

## 1.4 Objetivos y sumario de la tesis

En esta tesis presentamos un trabajo de estudio multi-longitud de onda (óptico, rayos X y gamma) de varios sistemas binarios emisores en rayos X y/o $\gamma$. En el óptico hemos descubierto y estudiado en detalle el sistema TYC 2675 663 1 (Cap. 3), emisor de rayos X blandos (E$\leq$2.1 keV). En rayos X y $\gamma$ hemos estudiado dos sistemas transitorios con agujero negro (comúnmente llamados *microcuásares*): GRO J1655–40 y GX 339–4 (Caps. 4 y 5). Las capacidades espectrales de *INTEGRAL* en el rango de rayos X y $\gamma$ (E = 3 − 10 000 keV) nos han permitido realizar el estudio en detalle de los procesos físicos que dan lugar a dicha emisión en este tipo de objetos. Las capacidades fotométricas de la cámara OMC, junto con la utilización de telescopios en tierra, nos han permitido desvelar la naturaleza de este nuevo sistema binario y de las causas de su emisión en rayos X.

Mientras que los agujeros negros estudiados en esta tesis corresponden a un programa aceptado de observación (Caps. 4 y 5), el sistema estudiado en el Cap. 3 resultó de las observaciones de un programa de ciencia serendípita con OMC. En este último programa, tal y como se explica en el Cap. 2, todas las fuentes emisoras y candidatas a emitir en rayos X y/o $\gamma$ han sido incluídas en el *OMC Input Catalogue*, y son candidatas a ser observadas en cualquier momento con INTEGRAL.

[3] Reflection is described in the high energy spectra of black holes by a decrease of flux at $\approx$10 keV plus a spectral hump at around 20 − 30 keV. This is due to photoabsorption, iron fluorescence and Compton scattering (George & Fabian, 1991).

La contribución más importante en esta tesis sido el estudio de la emisión en altas energías de dos agujeros negros, dando valiosas pistas acerca de la fuente emisora en dicho rango. Estos dos agujeros negros, debido al diferente ángulo de inclinación de sus planos orbitales con respecto a nuestra dirección visual, nos han permitido obtener conclusiones importantes acerca de la geometría y los procesos físicos que dan lugar a dicha emisión. Dichas conclusiones, aunque preliminares, de confirmarse serían cruciales en otras ramas de la astrofísica de altas energías (como los estudios en rayos X realizados con otros satélites como *CHANDRA* y *XMM-Newton*) puesto que muchas veces la emisión en rayos X es estimulada por procesos de emisión a energías aún mayores, como el rango cubierto por *INTEGRAL*.

# Chapter 2

# The OMC Input Catalogue

In this chapter we present the basic concepts of the *OMC Input Catalogue* for the Optical Monitoring Camera on-board the *INTEGRAL* satellite. For a description of the Catalogue format and entries see Sections 2.5 and 2.6.

## 2.1 Purpose and scope

The OMC has been designed to make, for the first time, observations of long duration in the optical band simultaneously with X-ray and Gamma-ray observations. These simultaneous multi-wavelength observations are particularly important in high-energy astrophysics, where variability is typically fast.

To provide calibrated standard V-Johnson photometry for the targets of interest, it is necessary to observe a set of well calibrated photometric standard stars. Moreover, in order to know the pointing of the instrument with a fraction of a pixel precision, a set of astrometric reference stars is also needed. Due to limitations in the available RAM memory on the Data Processing Electronics (DPE), the On Board Data Handling (OBDH) capabilities and the available telemetry to the ground, it is also necessary to know, *a priori*, the objects of interest within the FOV. Only windows of the CCD containing those objects will be transmitted to ground. The OMC Input Catalogue (with 541 802 entries), is able to suply all this information, the reference stars and the objects of scientific interest.

The OMC Pointing Software (OMCPS) runs at ISOC to create the telecommands required to operate the OMC. It takes into account the strategy of the observation for each pointing, the expected objects in the OMC FOV, their V magnitudes and their priorities, allowing to optimize the scientific performances of the instrument.

The OMC telecommands allow to monitor a maximum of 228 targets. However, the maximum number of science sources that can be monitored depends on the OMC telemetry allocation, the size of downloaded sub-windows and the number of sub-windows generated for each target. OMCPS can generate a mosaic of sub-windows for a given

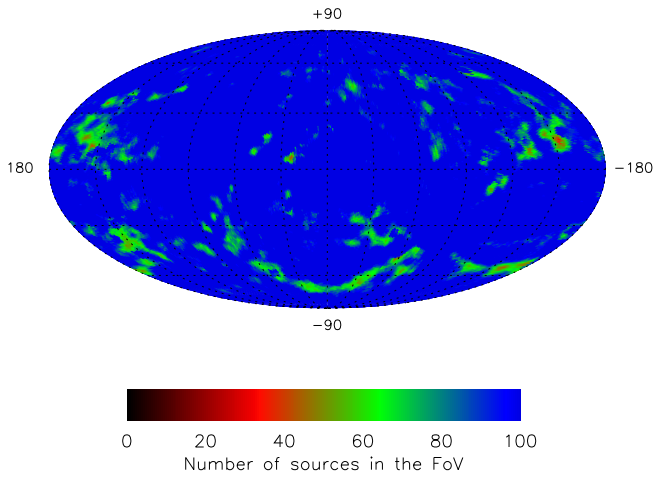


**Figure 2.1**: Number of sources per OMC FOV contained in the OMCIC (100 level means $\gtrsim$100 sources within each FOV). Galactic coordinates with the origin at the center of the plot.

target, depending on their *extension parameter*. A maximum value of 900 arcsec has been assigned to the extension parameter, in such case a 5×5 mosaic of sub-windows of 11×11 pixels is generated by the OMCPS. Typically 100 sub-windows of 11×11 pixels are downloaded. In Figure 2.1 we show the distribution of sources contained in the OMCIC (reference stars plus scientific sources) over the sky.

In this Chapter we focus on the description of the scientific targets compiled in the last version of this catalogue. For a description of the work done in the compilation of reference stars see Domingo et al. (2003) and the Catalogue internal report document OMC/UBA/22000/RPT/001 [1].

## 2.2 $\gamma$-ray sources

We included all the sources emitting at $\gamma$-rays compiled in several catalogues from older missions:

1. **The Third EGRET Catalog of High-Energy Gamma-Ray Sources**
   Hartman et al. (1999)

   - 271 sources (E > 100 MeV) detected during CGRO Cycles 1,2,3 and 4. Completely reprocessed data has been used in this compilation.

[1] A link to this document can be found at: ftp://ftp.laeff.inta.es/pub/users/mcaballe/OMCIC/.

2. **Second COS-B catalog of high-energy Gamma-ray sources**
   Swanenburg et al. (1981)

   - 25 high-energy sources (E > 100 MeV) observed during the period 1975-1978.

3. **First COS-B catalog: New high-energy Gamma-ray sources observed by COS-B**
   Hermsen et al. (1977)

   - 13 high-energy sources.

4. **First COS-B catalog: Present Status of Gamma Ray Astronomy**
   Pinkau (1979)

   - 24 high-energy sources.

5. **SIGMA survey of the Galactic Center region and discovery of a hard X-ray transient**
   Vargas et al. (1996)

   - 15 high-energy sources in the Galactic Center region observed from March 1990 to September 1994.

6. **Catalog of SAS-2 Gamma-Ray Observations**
   Fichtel et al. (1990)

   - 32 sources (AGN, LMC, SMC, ....) + 113 pulsars.
   - 27 SAS-2 *other* sources, some of them coming from:
     - **High-Energy Gamma-Ray results from the Second Small Astronomy Satellite (SAS-2)** (Fichtel et al., 1975)
     - **Final SAS-2 Gamma-Ray results on sources in the galactic anticenter region** (Thompson et al., 1977)

7. **Sources from the INTEGRAL Reference Catalogue (HEC)**
   Ebisawa et al. (2003)

   - 1 518 sources in v24, and increasing in successive releases.
   - HMXB catalog (Liu et al., 2000)

- LMXB catalog (Liu et al., 2001)
- Gamma ray sources catalog (50 keV-1 TeV) (Macomb & Gehrels, 1999)
- 4th Uhuru catalog (2-6 keV) (Forman et al., 1978)
- HEAO1 A4 catalog (13-180 keV) (Levine et al., 1984)
- Piccinotti's sample AGNs Batse observations (2-10 keV) (Malizia et al., 1999)
- Tartarus reduced ASCA AGN data (Turner et al., 2001)
- IAUC new sources (from 7341 to 7932)

In parallel to the work with the previously mentioned catalogues, the SIMBAD data base has been interrogated to extract all the Gamma-ray sources included in it (refer to the Catalogue internal report document OMC/UBA/22000/RPT/001). By considering all the objects classified as *object type: gamma* and all those belonging to *gamma catalogues* we obtain a compilation of additional 252 gamma sources.

## 2.3 X-ray sources

One of the main scientific goals of the ROSAT mission (1990-1999) has been to perform the first all-sky survey in X-rays, containing 4 times more sources than all other existing X-ray catalogues. For this reason, we concentrated our compilation work on ROSAT, not considering older missions as UHURU (2-6 keV), OSO-7 (1-60 keV), ARIEL-5 (2-18 keV), HEAO-1/A1 (1-20 keV), HEAO-1/A2 (0.2-2.8 keV) and HEAO-1/A4 (13-180 keV), which sampled only a few percent of the sky and have been superseded by ROSAT.

The ROSAT All-Sky Survey (RASS) was conducted in 1990/91, and after a second analysis performed in 1994/95, 145 060 sources were detected (detection likelihood $\geq$ 7). The brightest 18 806 sources have been published up to now in the *All-Sky Survey Bright Source Catalogue* (Voges et al., 1999) (hereafter RASS-BSC), whereas the remaining sources (105 924 fainter sources) have been published in *All-Sky Survey Faint Source Catalogue* (Voges et al., 2000) (hereafter RASS-FSC).

## 2.4 Optical variable sources

At the same time of monitoring all the main targets observed by the high-energy instruments, the OMC observes a large amount of optical objects present in its field of view. In this section we describe the process of compilation of the optical sources with special scientific interest that have been included.

OMCIC includes all known galactic and extragalactic variable stars as well as those classified as *suspected variables*. The OMC will substantially increase our physical

understanding on this type of objects since its operational mode allows relatively long and continuous monitoring periods of up to two weeks.

Special care has been devoted to the compilation of extragalactic objects (AGN, QSO, Starburts Galaxies, HII galaxies,...). Apart from their interest as potential high-energy emitters, the OMC analyzes its optical variability during a large period of time and provides a large data base with homogeneus V magnitudes (most of these objects have only B or photographic magnitudes).

In this section, we first list the catalogues and data bases used, with the compilation itself described as well.

The second part refers to the work of Downes et al. (2001) catalog and the inclusion of candidates to classical T-Tauri stars and candidates to cool dwarfs of G-K-M spectral type, as explained in Section 2.4.2 to 2.4.3.

In the following we list the catalogues used for the compilation of optical variable sources:

- Hipparcos Catalogue (11 597 variable stars). The information on variability present in the Tycho-1 Catalogue was not considered since its photometry was not yet thoroughly used to investigate intrinsic stellar variability and several sources of confusion were expected because of the difficult treatment of non-detected transits and apparent variability due to duplicity.

- *General Catalogue of Variable Stars (GCVS)* (Kholopov et al., 1998)
  This version contains:

  - GCVS Catalogue (Vols. I-III): It includes the catalogue of variable stars (Kholopov et al. 1985-88), updated and completed with the seven Name-Lists of Variable Stars Nos. 67-73 published during the period 1985-1997 (see IBVS No. 2681, 1985; No. 3058, 1987; No. 3323, 1989; No. 3530, 1990; No. 3840, 1993; No. 4140, 1995; No. 4471, 1997).
  - NSV Catalogue: This is a catalogue of suspected variable stars (not designated as variables prior to 1980). It mainly contains the same data as in the *New Catalogue of Suspected Variable Stars* (Kukarkin et al., 1982), but the coordinates were improved and necessary corrections were also introduced.
  - GCVS Catalogue (Vol. V): It contains data for extragalactic variable stars and extragalactic supernovae.
  - A file containing cross-identifications of variable stars (GCVS Vol. IV).

  Thus, this 4.1 Edition is an update of the 4.0 one (Volumes I-V) of the GCVS, that included also the NSV Catalogue. The Sternberg Institute started preparation of

a release GCVS 4.2 which will contain improved positions, classifications, etc. The number of sources in these catalogues (4.1 Edition) is:

| | |
|---|---|
| 31 918 | galactic variable stars |
| 14 811 | suspected variable stars |
| 10 979 | extragalactic variable stars |
| 984 | extragalactic supernovae |

- *New Catalogue of Suspected Variable Stars. Supplement* (Kazarovets et al., 1998)
  It is the supplementary part to the NSV (Kukarkin et al., 1982). It contains 11 206 stars suspected of variability which were not designated as variables prior to 1997.

- *The 74th Special Name-list of Variable Stars* (Kazarovets et al., 1999)
  This list contains 3 157 variable stars whose variability was discovered by the Hipparcos mission. All these stars satisfed the GCVS variability criteria. According to these criteria several variables were reclassified. In the other hand, new cross-identifications were added to the ones from Hipparcos.

  2 417 stars whose variability was discovered by Hipparcos were not included in this list: 91 were contained in the GCVS; the rest of objects did not meet some of the GCVS naming criteria and they appeared either in the Supplement to the NSV Catalogue (Kazarovets et al., 1998), or are already present in the NSV Catalogue (Kukarkin et al., 1982).

- *Variable stars in the Tycho photometric observations* (1091 stars) (Piquard , 2001)
  This is constructed in base on photometric observations taken by Tycho experiment, onboard the Hipparcos mission. A treatment taking into account truncated detections and censored measurements was made to search for variability in the faint part of Tycho-1 catalogue. Reliable results were obtained for stars as faint as 11 mag.

  This list contains 687 stars suspected to be variable stars, which likely do not belong to other existing variable compilations available in the OMC catalogue. We took astrometric data from Tycho-2 and rejected those stars without position in this catalogue.

- *Quasars and Active Galactic Nuclei, 8th Edition* (Véron-Cetty & Véron, 1998)
  This catalogue is an update of the previous versions. It contains:

| | | |
|---|---|---|
| table1 | 11 358 | Quasars (brighter than absolute B magnitude -23) |
| table2 | 357 | Confirmed, probable or possible BL Lac objects |
| table3 | 3 334 | Active galaxies (fainter than -23) |
| table4 | 57 | Rejected quasars |
| refs | 2 740 | References to tables 1 to 4 |

- *The Active Galactic Nuclei (AGN) Catalog* (Padovani , 1998)
  This catalogue includes 12 021 quasars and active galaxies and is heavily based on the catalogue of *Quasars and Active Galactic Nuclei (7th Edition)* (Véron-Cetty & Véron, 1996). It also includes the *BL Lac Catalog* (Padovani & Giommi, 1995) updated with BL Lacs discovered in 1996, and the radio galaxies in the 1 Jy, S4, and S5 radio catalogues. The AGN Catalog reports V magnitudes almost for all their objects. Nevertheless, in some cases V magnitudes have been derived from B magnitudes by subtracting (B-V) values typical of the class to which an object belongs to. According to Padovani, the V magnitudes in Véron-Cetty & Véron catalogue were mostly B or photographic magnitudes when no (B-V) value was available. Furthermore, for all sources in this catalogue, the author reported a classification based mostly on the one given by Véron-Cetty & Véron, subdividing the QSO in *radio-loud* and *radio-quiet*.

- *HII Galaxies Compilation* (Mas-Hesse et al., 1998)
  It contains 441 objects.

In parallel to the work with the previously mentioned catalogues, the SIMBAD data base has been interrogated to extract all the variable sources (galactic and extra-galactic) included in it. This work is thoroughly explained in the Catalogue internal report document OMC/UBA/22000/RPT/001.

### 2.4.1 Catalog of Cataclysmic variables

We have included the *Catalog of Cataclysmic Variables* of Downes et al. (2001), with 1 314 sources.

Duplicities from OMCIC (i.e doing a search by coordinates given a radius of $10''$) were avoided and, in the case of such a duplicity, we only updated the values of R16 and R18 in the catalogue (only in the case that R16 $> 5,6$). Otherwise, if no entry was found inside this radius, we created a new entry with all the information included in the catalog (Downes et al., 2001) and, in the cases with counterpart at SIMBAD, this last identification was included as well (containing astrometric and photometric information). Magnitudes correspond to the value at maximum brightness of the target.

### 2.4.2 Candidates to Classical T-Tauri stars

We are interested in monitoring by OMC of these Classical T-Tauri Stars (hereafter CTTS) because of several reasons:

1. They emit in the optical band in a periodic or no periodic way, but always having some type of variability related to their physical conditions.

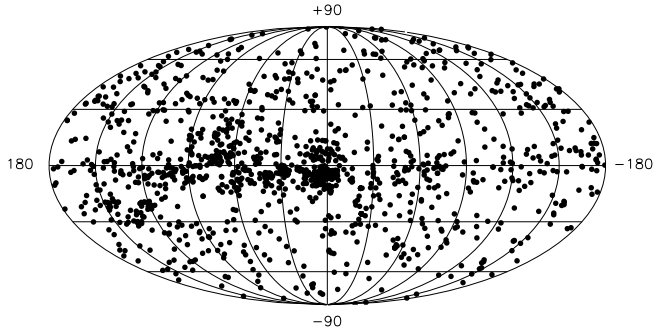


**Figure 2.2**: Sky distribution of the cataclysmic variables coming from Downes et al. (2001). Here only appear those which are not in HEC. Galactic coordinates with the origin at the center of the plot.

2. The amplitude of the light curve variations varies in the range (0.01-3) mag.

3. Periods often are about ≈1 day, so monitoring from a space platform should overcome the problems of observing them from the ground.

We summarize the work done in the compilation of candidates to classical T-Tauri stars as follows:

The search of CTTS has been made in all the sky, on the basis of their observed colors inferred from their intrinsic colors through some standard color-transformation equations (Caballero-García , 2003). We did not consider reddening effects (this is an approximation). We started keeping entries from *The Second U.S. Naval Observatory CCD Astrograph Catalog* (hereafter UCAC2) (Zacharias et al., 2004), which has infrared colors $J$, $H$, and $K$ from *2MASS All-Sky Catalog of Point Sources* (hereafter 2MASS) (Cutri et al., 2003), imposing a search radius of $2''$ between each entry of UCAC2 and 2MASS. Note the fact that UCAC2 was not distributed uniformly over the sky at the time of our compilation (i.e. see in Figure 2.4 the hole at declinations above $+45°$)

Once we had UCAC2 sources (which have very good astrometric data together with magnitudes in the optical band) with infrared colors, we imposed the restriction of CTTS in a $(J-H)/(H-K)$ diagram color (Caballero-García , 2003). We imposed also limit ranges in infrared colors, not to be fainter than 16 mag and not brighter than 5 mag.

When we finished the search in the color diagram, we imposed restrictions in the sense of contamination by other stars in the field around the target. To do that, we used *The Guide Star Catalog, Version 2.2* (hereafter GSC2) (STScI , 2001) imposing a maximum degree of contamination of 0.2 mag in a field radius of 2.9 pix (to be more realistic, we considered also a corona of radius 1.5 pix. in which stars contribute only by a half of their flux).

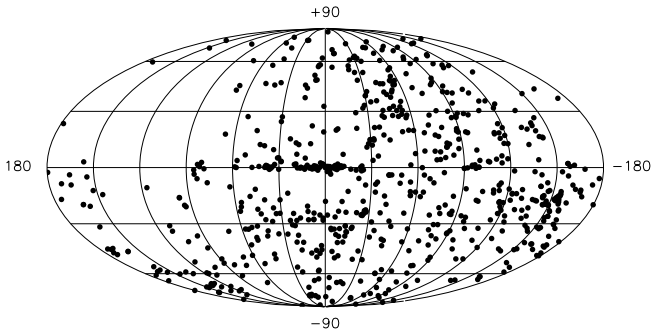


**Figure 2.3**: Sky distribution of CTTS coming from our compilation. Galactic coordinates, with the origin in the center of the plot.

Finally, we checked duplicities with OMCIC (by coordinates, imposing a radius search of $10''$), resulting in 141 candidates with an OMCIC entry inside the radius and 732 entries without any entry from OMCIC. In Figure 2.3 we present the spatial distribution of the 732 candidates to CTTS without any counterpart at OMCIC.

As we mentioned above, in the case that duplicities with OMCIC exist (i.e doing a search by coordinates given a radius of $10''$) we only updated the values of R16 and R18 in the catalogue (only in the case that R16 $> 3$). Otherwise, if no entry was found inside this radius, we created a new entry with all the information included in the catalog of Zacharias et al. (2004) (astrometric and photometric information comes from UCAC2).

### 2.4.3 Candidates to cool dwarfs of G-K-M spectral type

It is broadly known that cool dwarfs of G-K-M spectral type can be variable at a certain degree (mainly in the range 0.05-0.1 mag and not greater than 0.2 mag), showing very interesting properties of the behaviour of this kind of stars.

We summarize the work done in the compilation of candidates to cool dwarfs of G-K-M spectral type as follows:

As in the case of CTTS we did a search of candidates to cool dwarfs of G-K-M spectral type (hereafter GKM) in all the sky (we did not consider reddening effects; this is an approximation). In the selection of GKM we need suitable proper motions and colors, in order to avoid giant stars. We select only proper motions greater than 0.04 $''$/year. Additionally, we took infrared 2MASS (Cutri et al., 2003) colors present in UCAC2 (Zacharias et al., 2004) (imposing 2MASS counterpart at a radius of $2''$ as maximum). Then, we select those entries with $(J-H) \in (0.305, 0.66)$ and $(H-K) \in (0.05, 0.37)$ (i.e. the condition of star with G to M spectral type).

We also limited the optical magnitudes to the range (6,16) mag (these values correpond to the UCAC2 system) and took only those entries with good photometric

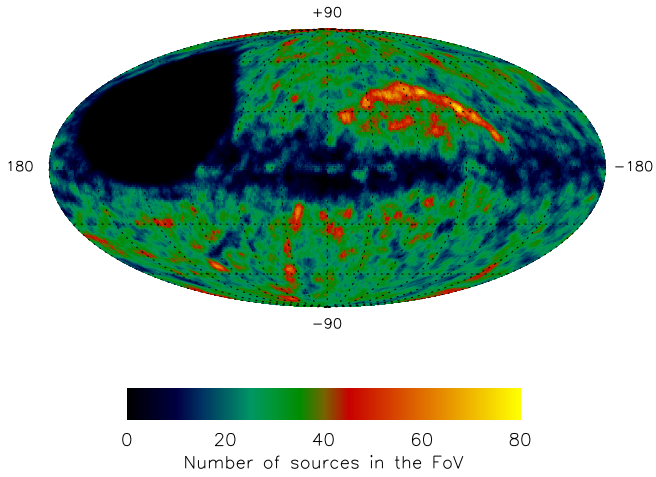


**Figure 2.4**: Number of sources for each field coming from the CTTS and GKM compilation. Galactic coordinates, with the origin in the center of the plot.

quality 2MASS data.

Then, when we finished the selection of cool dwarfs candidates, we imposed restrictions in the sense of contamination by other stars in the field around the target. To do that, we used the GSC2 imposing a maximum degree of contamination of 0.2 mag in a field radius of 2.9 pix (to be more realistic, we considered also a corona of radius 1.5 pix. in which stars contribute only by a half of their flux).

Finally, we checked duplicities with OMCIC (by coordinates, imposing a radius search of $10''$), resulting in 5 527 candidates with an OMCIC entry inside the radius and 35 101 entries without any entry from OMCIC. In Figure 2.4 we present the spatial distribution of the 35 833 candidates to CTTS and GKM without any counterpart at OMCIC.

As we mentioned above, in the case that duplicities with OMCIC exist (i.e. doing a search by coordinates given a radius of $10''$) we only updated the values of R16 and R18 in the catalogue (only in the case that R16 $>$ 4). Otherwise, if no entry was found inside this radius, we created a new entry with all the information included in the catalog of Zacharias et al. (2004) (astrometric and photometric information comes from UCAC2).

The photometric system for magnitudes is UCAC2 system, which is defined by the UCAC (579-642) nm bandpass, located between V and R. Observations were not made under photometric conditions and the magnitude is given only for UCAC2 identification purposes. Estimated errors are 0.3 mag absolute, 0.1 mag relative.

## 2.5 Global characteristics of the OMC Input Catalogue

### 2.5.1 Contents at present

- Reference stars
  - Astrometric standards
    Needed: 10 stars/pointing (4° x 4°): 26 000 stars
    Available: 61 941 stars
    * from Hipparcos [2]: 7 020 stars
    * from Tycho [3]: 17 488 stars
  - Photometric standards
    Needed: 10 stars/pointing (4° x 4°): 26 000 stars
    Available: 205 697 stars
    * from Hipparcos: 5 677 stars
    * from Tycho: 200 020 stars
    * faint stars: 369 stars
  - Total (astr. + phot.) 267 638
    (36 950 stars are both astrometric and photometric standard stars)
- High energy sources [4]
  - $\gamma$-ray from our compilation 85
  - High energy sources (from HEC at ISDC) 1513
  - X-ray 123 857
  - Sources from the OMC Extended Catalogue (at ISOC) 36
  - Sources from internal lists (Announcements of Opportunities and others) 187
- Additional sources
  - Optical variables (not classified as cold G-K-M or CTT star candidates) 84 293
  - Candidates to Classical T-Tauri stars 858
  - Candidates to G-K-M spectral type 40 492
- Objects without any priority 22 843

**Total number of entries** 541 802

[2] With magnitude taken from Hipparcos catalogue.
[3] With magnitude taken from Tycho catalogue.
[4] Because a given source can belong to more than one of these groups, the numbers reported here have been calculated as the number of entries of each priority assigned to every class of objects (see Section 2.5.2).

### 2.5.2 Priority assigned to the scientific targets

As explained in Section 2.1, the OMC scientific mode operations are performed by uploading a table with the expected (X,Y) coordinates of the targets of interest to be monitored by the OMC. To arrange this table, a priority flag must be assigned to all scientific targets included in the OMC Input Catalogue.

For the assignation of such priority flag, we have adopted the general criterion:

- Priority 1: $\gamma$-ray sources without mosaics greater than 11×11 pixels$^2$ size (i.e. R10≤190).
- Priority 2: $\gamma$-ray sources with mosaics greater than 11×11 pixels$^2$ size (i.e. R10 > 190).
- Priority 3: Bright X-ray sources
- Priority 4: Candidates to classical T-Tauri stars
- Priority 5: Candidates to cool dwarfs of G-K-M spectral type
- Priority 6: Isolated optical variable sources with $V < 18.0$ or without any magnitude
- Priority 7: The rest of optical variable sources with $V < 18.0$ or without any magnitude
- Priority 8: Faint X-ray sources

In the present version of the catalogue, a first attempt has been made to follow this criterion: priorities 1 and 2 have been given to the 1821 high energy sources (Section 2.2). priority 3 to the 18 332 X-ray bright sources (Section 2.3), priority 4 to the 858 candidates to classical T-Tauri stars (Section 2.4.2), priority 4 to the 40 492 candidates to cool dwarfs of G-K-M spectral type (Section 2.4.3), priority 6 to the 21 797 isolated optical variable sources (Section 2.4 and 2.5.2.2) with $V$<18 mag or without any magnitude, priority 7 to the 62 496 rest of optical variable sources with $V$<18 mag or without any magnitude (Section 2.4 and 2.5.2.2) and priority 8 to the 105 525 X-ray faint sources (Section 2.3). However, its application had some drawbacks until OMCIC (V0004). In OMCIC (V0001), due to the compilation process followed in Section 2.4, several sources classified as optical variables were also potential or real X-ray and/or $\gamma$-ray emitters (e.g. known X-ray binaries were included as optical variables). On the other hand, some X and $\gamma$-ray compiled sources had their optical counterpart already included as optical variable. These items were corrected in the building of OMCIC (V0004) (and in some sense in OMCIC (V0003)). To solve this problem, in this version we made a work of cross-correlation between all the entries of the OMCIC, finally keeping the entry with the largest priority (i.e. smallest

number in R16 field) and updating the rest of duplicated sources with null priority (see Section 2.5.2.3). In parallel, we updated C20 for all the sources with the identifier appearing at SIMBAD (Section 2.5.2.4). We are working continuously in updating the OMCIC to include the interesting sources to be monitored with OMC with the appropiate priority field. With these items we have the intention of avoiding duplicities, having OMCIC on-line with SIMBAD (and with HEC; Ebisawa et al. 2003) and keeping all the sources with the correct priority according to their interest to be observed by OMC.

#### 2.5.2.1 Priority in optical sources

Those sources with priority field (R16) empty will not be observed by OMC, except astrometric and photometric standard stars. In the catalogue several optical sources appear with $V \geq 18$ which have R16 empty. These sources will not be observed, because they have magnitude larger than the limiting magnitude of the OMC (Section 1.2.3). Only those optical sources with $V < 18$ or without any magnitude will be observed and have a filled priority field (R16='6','7').

#### 2.5.2.2 Contamination of optical variable sources

Due to the great number of sources appearing at OMCIC and the interest to have good photometry for as many sources as possible, we have decided to rearrange priorities of optical sources in OMCIC V0004 according to their degree of contamination.

As we mentioned above, a treatment to flag the sources which are contaminated by others in the field around the target was made during the building of OMCIC (V0004). To do that, we used GSC2, imposing a maximum degree of contamination of 0.75 mag (which corresponds to $F_{joint} = 2 \times F_{target}$) in a field radius of 2.9 pix (to be more realistic, we considered also a corona of radius 1.5 pix. in which stars contribute only by a half of their flux).

Thus, the sources contaminated by more than 0.75 mag were flagged with priority '7' while the rest of the optical variable sources were assigned priority '6'.

#### 2.5.2.3 Treatment of duplicated sources

It is an annoying fact for any catalogue to have duplicities (or multiplicities) of entries and it is even worse that these duplicated entries have different priorities. In order to avoid that, in the building of OMCIC (V0004) we removed the priority of those entries with the same identifier at SIMBAD database except those cases in which the discrepancy in the coordinates was greater than 18 arcsec. This resulted in 8 406 sources that lost their priority.

#### 2.5.2.4 Cross-correlation with SIMBAD

An important fact in order to search for sources in OMCIC is to have at least one identifier different from `OMCID`. To do that and in order to make identifications easier, the SIMBAD database was queried, with the identifiers present in our catalogue. After the upgrade, only 28 550 entries of OMCIC continued with a blank in $C_{20}$ in OMCIC (V0004) whereas in OMCIC (V0003) there were 431 137 entries.

#### 2.5.2.5 The source extent field

The source extent is the minimum size of the box that will be downloaded in OMC operations. As it is explained in Section 2.1 the maximum value of this field is '900' arcsec and it is an imposed value. All values of the source extent field (calculated from the original catalogues) greater than the previous are cutted at this value. If this field is zero then a box of 11×11 pixels of size is downloaded in OMC operations. In this sense, when this field is different of zero then a mosaic of boxes of 11×11 pixels each is downloaded in OMC operations to reach the source extent value.

#### 2.5.2.6 Additional considerations

**Null values in the catalogue**

In those cases without any value for the fields R5, R6, R10, R11, R12 and R14 (R3 and R4 never have a null value, because all entries in the catalogue have coordinates) a null value is adopted which is required since the catalogue will be converted to a FITS format by ISDC in satellite operations.

| | | |
|---|---|---|
| R5 | = | 99999.9999 |
| R6 | = | 99999.9999 |
| R11 | = | 99.999 |
| R12 | = | 9.999 |
| R14 | = | +9.999 |

With the fields R7, R8 a null zero value and a flag is adopted when data is not available (Section 2.6.1). On contrary, with the field R10 a null zero value is taken only.

**Mandatory fields**

Those fields which always are filled and never have null values constitute this category. These fields are: R1, R3, R4, R7, R8, R9 and R10.

## 2.6 The present catalogue

In the next figures we present the distribution of sources of OMCIC depending on their priority (see the attached captions).

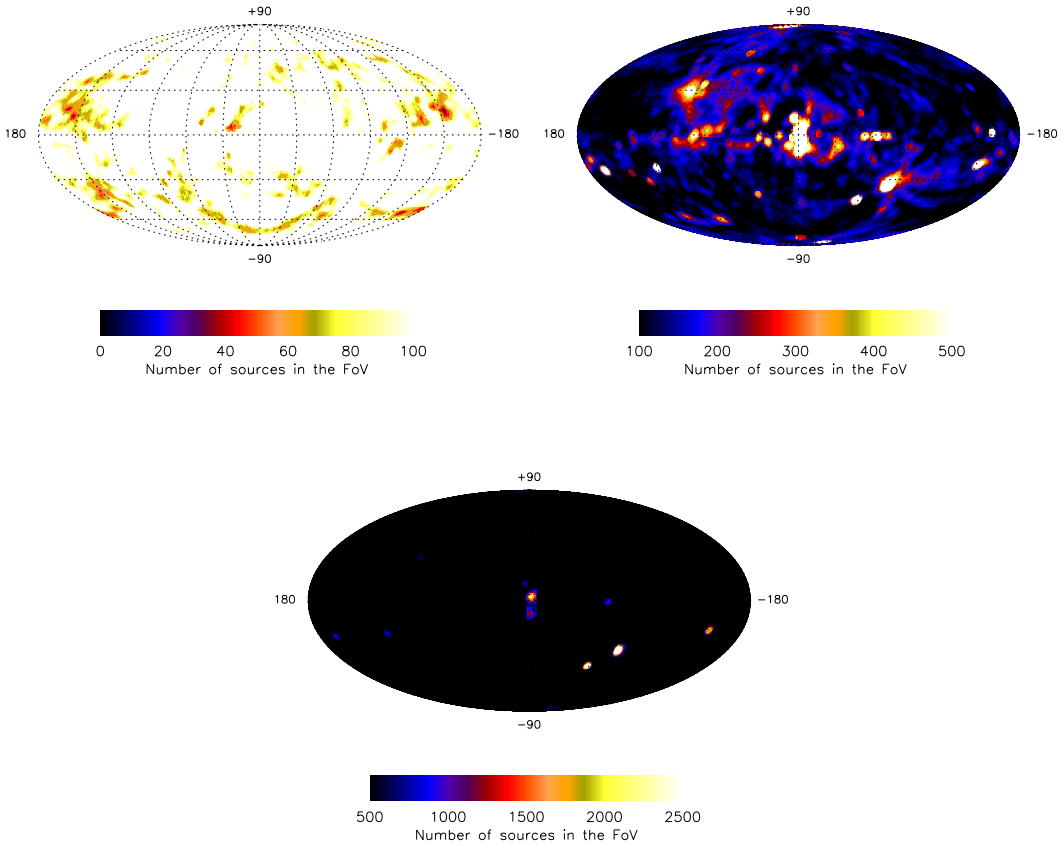


**Figure 2.5**: Sky distribution in galactic coordinates (with the origin at the center of the plot) of 251 321 sources with non null priority contained in OMCIC. Fields with less than 100, 500 and 2 500 sources (top-left, top-right and bottom, respectively).

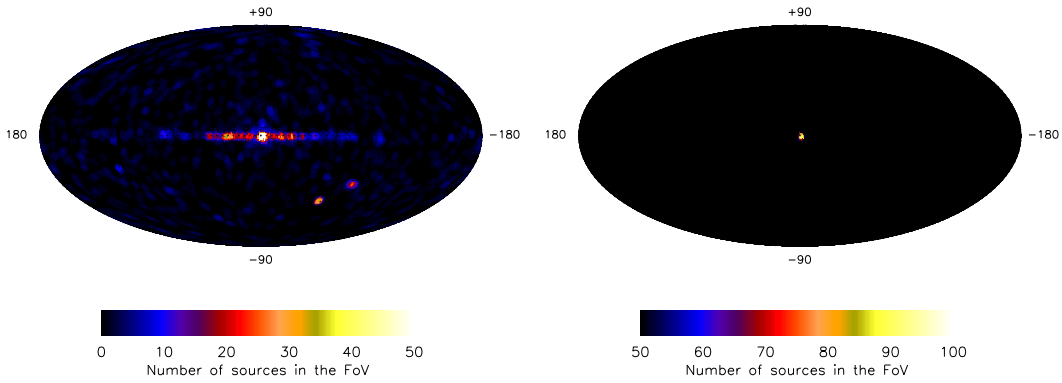


**Figure 2.6**: Sky distribution in galactic coordinates of 1 821 sources with the highest priority (i.e. '1' and '2') contained in OMCIC. Fields with less and more than 50 sources (left and right, respectively).

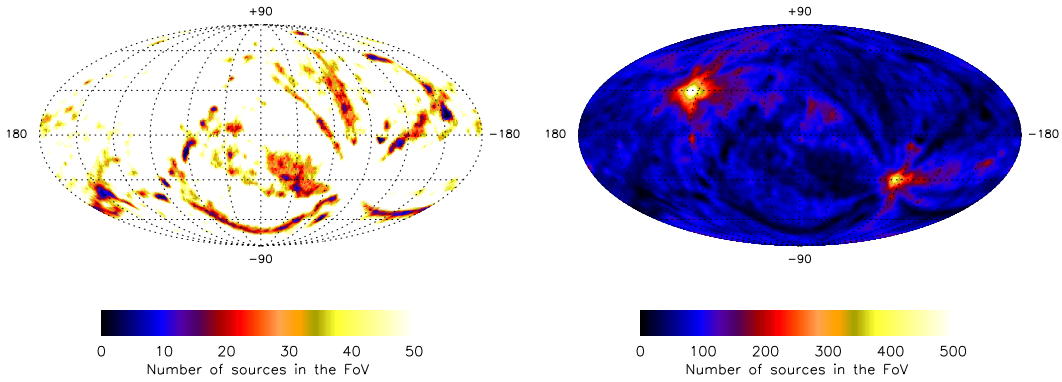


**Figure 2.7**: Sky distribution in galactic coordinates of 123 857 sources with priorities '3' and '8' contained in OMCIC. Fields with less and more than 50 sources (left and right, respectively).

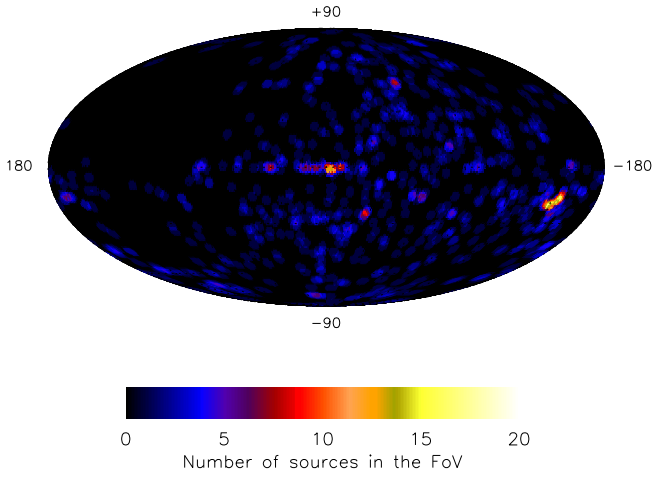


**Figure 2.8**: Sky distribution in galactic coordinates of 858 sources with priority '4' contained in OMCIC.

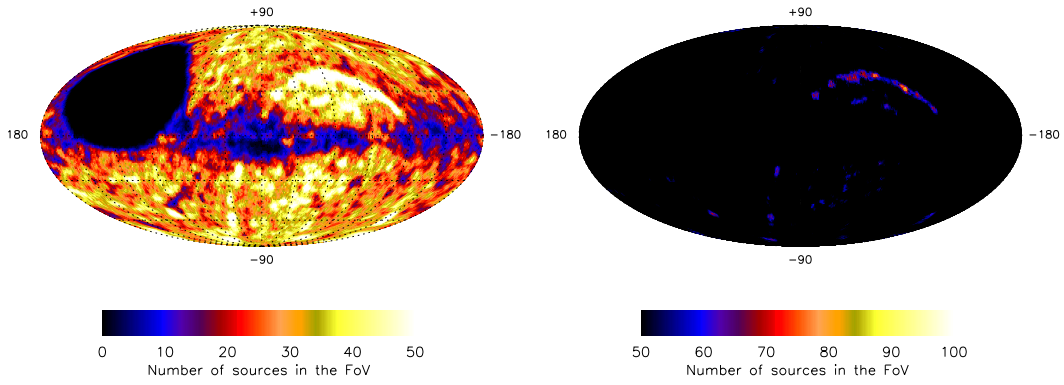


**Figure 2.9**: Sky distribution in galactic coordinates of 40 492 sources with priority '5' contained in OMCIC. Fields with less and more than 50 sources (left and right, respectively).

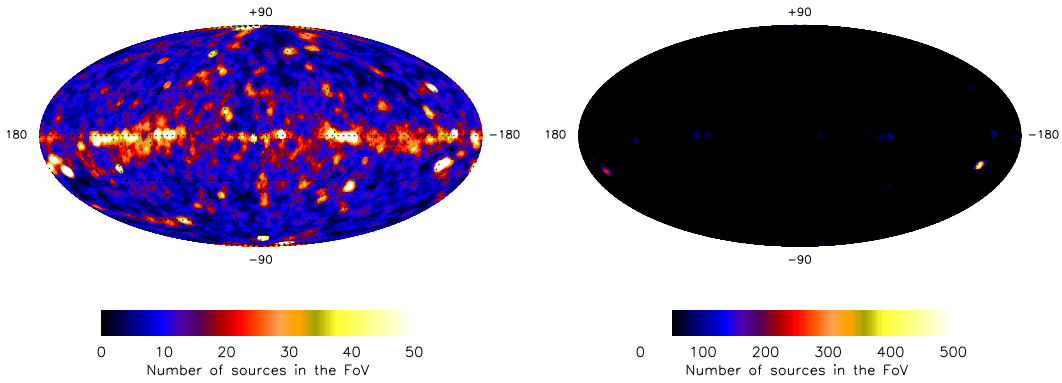


**Figure 2.10**: Sky distribution in galactic coordinates of 21 797 sources with priority '6' contained in OMCIC. Fields with less and more than 50 sources (left and right, respectively).

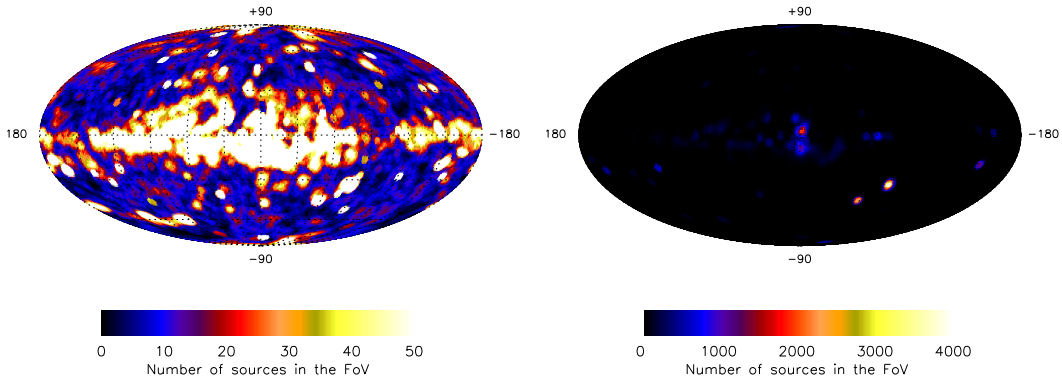


**Figure 2.11**: Sky distribution in galactic coordinates of 62 496 sources with priority '7' contained in OMCIC. Fields with less and more than 50 sources (left and right, respectively).

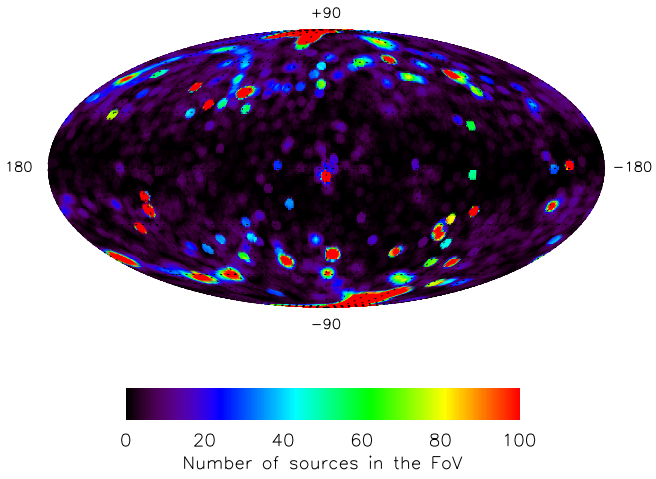


**Figure 2.12**: Spatial distribution of scientific sources with null priority in OMCIC.

### 2.6.1 Byte-per-byte format description

#### 2.6.1.1 OMC Main Catalogue

| **Contents of the OMC Main Catalogue** | | | |
|---|---|---|---|
| **Field** | **Bytes** | **Format** | **Description** |
| R1 | 1- 13 | I4,I6,3X | OMC Identifier |
| R2 | 14- 26 | A12,1X | Object type |
| R3 | 27- 39 | F12.8,1X | $\alpha$, degrees (Epoch J2000.0, Equinox J2000.0) |
| R4 | 40- 52 | F12.8,1X | $\delta$, degrees (Epoch J2000.0, Equinox J2000.0) |
| R5 | 53- 63 | F10.4,1X | Standard error in $\alpha \cdot \cos\delta$ at J2000.0 (arcsec) |
| R6 | 64- 74 | F10.4,1X | Standard error in $\delta$ at J2000.0 (arcsec) |
| R7 | 75- 83 | F8.2,1X | $\mu_\alpha \cdot \cos\delta$ (mas/yr) |
| R8 | 84- 92 | F8.2,1X | $\mu_\delta$ (mas/yr) |
| R9 | 93- 95 | A2,1X | Source of astrometric data |
| R10 | 96-103 | F7.1,1X | Source extent (arcsec) |
| R11 | 104-110 | F6.3,1X | V (Johnson) magnitude |
| R12 | 111-116 | F5.3,1X | $\sigma_{V_J}$ |
| R13 | 117-119 | A2,1X | Source of V (Johnson) magnitude |
| R14 | 120-126 | F6.3,1X | $(B-V)_J$ (mag) |
| R15 | 127-129 | A2,1X | Flag: Standard star for OMC |
| R16 | 130-132 | A2,1X | Flag: Priority of the targets of interest |
| R17 | 133-134 | A1,1X | Flag: Updating the OMC catalogue |
| R18 | 135-140 | 3I2 | Updating date of the record |

**Remarks:**

- **Field R1 : Identifier**
  A procedure similar to that used for the designation of the identifiers in the Guide Star Catalogue (GSC) has been adopted for the OMC: a region number and a number within this region (the regions have the same boundaries as those in the GSC). For convenience, the last two bytes are blank.

- **Field R2 : Object type**
  The SIMBAD object type coding system is adopted. Note that it emphasizes the physical nature of the object rather than a peculiar emission in some region of the electromagnetic spectrum.
  - Bytes 1-3 Object type in SIMBAD
  - Bytes 4-12 Other classifications from source catalogues

    K- Kholopov et al., 1998
    P- Padovani, P., 1998
    C- Véron-Cetty, M.P., Véron, P., 1998
    D- Downes et al., 2001
    M- Mas, M., 1998
    T- Piquard et al., 2001

    GAM Gamma ray source according to our compilation (not in HEC)
    XB ROSAT X-ray Bright Source
    XF ROSAT X-ray Faint Source
    HEC INTEGRAL Reference Catalogue at ISDC
    CTT Candidates to classical T-Tauri stars
    GKM Candidates to cool dwarfs of G-K-M spectral type

- **Field R9, 1st digit: Source of the astrometric data**
  Codified as:

  **H** Hipparcos
  **T** Tycho-2
  **S** Simbad
  **U** UCAC2
  **V** GCVS group
  **C** Véron-Cetty, M.P., Véron, P., 1998
  **P** Padovani, P., 1998
  **M** Mas, M., 1998
  **B** ROSAT X-ray Bright Source Catalogue
  **F** ROSAT X-ray Faint Source Catalogue
  **E** EGRET
  **L** Landolt (faint photometric standard stars)
  **G** GSC

**X** INTEGRAL Reference Catalogue at ISDC (HEC)

**O** Others from the ground

- **Field R9, 2nd digit: Source of the astrometric data**
  Codified as:

  **U** No proper motion available (+0000.00 has been adopted)

  **X** Proper motion is greater than 9999.99 in absolute value (9998.00 value has been adopted)

- **Field R13, 1st digit: Source of the V (Johnson) magnitude**
  The following categories are distinguished:

  **H** Hipparcos

  **T** Tycho-2

  **S** SIMBAD

  **V** GCVS group

  **C** Véron-Cetty, M.P., Véron, P., 1998

  **P** Padovani, P., 1998

  **L** Landolt (faint photometric standard stars)

  **G** GSC

  **A** CAGE database

  **B** UCAC2 observations

  **O** Others from the ground

  **U** Updated from OMC observations

- **Field R13, 2nd digit: Source of the V (Johnson) magnitude**
  Depending on the original photometric system:

  **0** Originally in the Johnson system

  **1** Transformed from $H_{Hip}$

  **2** Transformed from $V_{Tyc}$

  **3** Transformed from other photometric systems

  **4** $V_{Tyc}$ is given in R11 (not transformed)

  **5** $B_{Tyc}$ or B (Johnson) are given in R11. ($B_{Tyc}$ only if the 1st digit of R13 is 'T')

  **6** R11 is a photographic magnitude

  **9** R11 is given in other photometric system not listed above (not transformed)

- **Field R15, 1st digit: Standard star for OMC**
  Three categories of stardard are distinguished:

  A Astrometric standard star

  P Photometric standard star

  B Both, astrometric and photometric standard star

- **Field R15, 2nd digit: Standard star for OMC**
  For photometric standard stars, three categories are distinguished:

  **C** Confirmed long-term stability by Hipparcos

  **S** The star is a secondary photometric standard star (from Hipparcos + Tycho)

  **F** Faint photometric standard star from other sources

  **N** New photometric standard star from OMC observations

- **Field R16: Priority of the targets of interest**

  **1** $\gamma$-ray sources without mosaics greater than 11×11 pixels$^2$ size (i.e. R10≤190)

  **2** $\gamma$-ray sources with mosaics greater than 11×11 pixels$^2$ size (i.e. R10 > 190)

  **3** X-ray sources from ROSAT Bright Source Catalogue

  **4** Candidates to Classical T-Tauri stars

  **5** Candidates to cool dwarfs of G-K-M spectral type

  **6** Optical variable sources (galactic and extragalactic variable stars, AGNs, radio-galaxies, HII galaxies,...) relatively non contaminated by other stars. No priority has been adopted for sources with V (Johnson) $\geq$ 18

  **7** The rest of optical variable sources with V (Johnson) $<$ 18

  **8** X-ray sources from ROSAT Faint Source Catalogue

- **Field R17: Updating the OMC catalogue**
  Several categories are distinguished:

  **1** Newly discovered optical counterparts of high-energy sources from INTEGRAL

  **2** Other sources of interest from ground-based observations or other space missions (not used).

  **3** Sources from INTEGRAL Reference Catalogue at ISDC

  **4** Sources from Extended Catalogue at ISOC.

  **5** Sources from INTEGRAL AO-N releases (where N is an integer number).

#### 2.6.1.2 OMC Cross-identification Catalogue

| Contents of the OMC Cross-identification Catalogue | | | |
|---|---|---|---|
| **Field** | **Bytes** | **Format** | **Description** |
| C1 | 1- 13 | I4,I6,3X | OMC Identifier |
| C2 | 14- 26 | A12,1X | Object type |
| C3 | 27- 51 | I10,15X | 2MASS Unique source identifier |
| C4 | 52- 58 | I6,1X | HIPPARCOS number |
| C5 | 59- 71 | I4,I6,I2,1X | TYCHO number |
| C6 | 72- 83 | I5,I6,1X | GSC number |
| C7 | 84- 91 | I6,A1,1X | HD number |
| C8 | 92-102 | I3,1X,I5,A1,1X | BD number |
| C9 | 103-113 | I3,1X,I5,A1,1X | CoD number |
| C10 | 114-124 | I3,1X,I5,A1,1X | CPD number |
| C11 | 125-137 | A12,1X | Variable star name |
| C12 | 138-144 | I5,A1,1X | NSV/NSVS number |
| C13 | 145-161 | A16,1X | CCDM number |
| C14 | 162-174 | A12,1X | INTEGRAL source name (IGR) |
| C15 | 175-191 | A16,1X | ROSAT source name (1RXS) |
| C16 | 192-208 | A16,1X | HEC source identifier |
| C17 | 209-225 | A16,1X | OMC Identifier in the Extended Catalogue |
| C18 | 226-244 | A18,1X | Other X-catalogue name |
| C19 | 245-263 | A18,1X | Gamma source name |
| C20 | 264-299 | A35,1X | SIMBAD Basic Identifier |
| C21 | 300-302 | A2,1X | Source of the optical counterpart identification |
| C22 | 303-318 | A15,1X | Spectral type |
| C23 | 319-325 | F6.3,1X | Mag. at max. brightness (magMax) |
| C24 | 326-332 | F6.3,1X | Mag. at min. brightness (magMin) |
| C25 | 333-335 | A2,1X | The photometric system for mags. (GCVS) |
| C26 | 336-352 | F16.10,1X | Period of the variable star (days) |
| C27 | 353-397 | 5(I4,I4,1X) | Proposal numbers |
| C28 | 398-398 | A1 | Relevant Flags for the source compilation |

**Description of the fields:**

- **Field C3: 2MASS Unique source identifier**
  This is the *pts key* star identification number found in the 2MASS point source catalog. It is a 4-byte integer greater than 0.

- **Field C14: INTEGRAL source name**
  It is based on J2000 position (format `JHHMMm+DDMM`)

- **Field C15: ROSAT source name (1RXS)**
  ROSAT All-Sky Survey Bright Source Catalogue name. It is based on J2000 position (format JHHMMSS.S+DDMMSS). One can get the complete standard name by adding 1RXS to the C15 field. Sources from ROSAT All-Sky Survey Faint Source Catalogue have also this designation.

- **Field C16: HEC source identifier**
  `SOURCE_ID` in HEC (High Energy Catalog), at ISDC. It is based on J2000 position (format JHHMMSS.S+DDMMSS)

- **Field C17: OMC Identifier from ISOC**
  From the OMC Extended Catalogue at ISOC. One can get the complete standard name by adding IOMC to the C17 field.

- **Field C18: Other X-catalogues name**
  X-ray source name not listed above. This field and C19 are the only fields which include an acronym with the identifier. The following priorities have been established:

  1. **2E** (Einstein obs. 2nd version)
  2. **2A** (Ariel satellite list 2)
  3. **3A** (Ariel satellite list 3)
  4. **AX** (ASCA satellite X-ray)
  5. **2S** (SAS-3 satellite list 2)
  6. **Granat** (Granat satellite)

- **Field C19: Gamma source name**
  Gamma source name including an acronym of the source catalogue. The following priorities have been established:

  1. **3EG** (Third EGRET Gamma-ray Catalogue)
  2. **1CG** (1st Cos B)
  3. **2CG** (2nd Cos B)

4. **2EG** (2nd EGRET Gamma-ray Catalogue)
5. **2EGS** (2nd EGRET Gamma-ray Catalogue Supplement)
6. **GRO** (Compton Gamma Ray Observatory)
7. **GeV** (Lamb R.C. & Macomb D.J. (1997) list)

- **Field C20: SIMBAD Basic Identifier**
- **Field C21: Source of the optical counterpart identification** (Not yet implemented)
  The optical counterpart of the high energy source has been obtained from:
  - **X**: XMM Input Catalogue
  - **S**: SIMBAD
  - **H**: HEASARC
  - **I**: Individual papers
- **Field C27: Proposal Numbers**
  The first four digits indicates the number assigned to the individual proposal made by the observer, the other four is a running number of each of the objects proposed to be observed.
- **Field C28: Relevant Flags for the source compilation**

  **1** NSV source not appearing both in SIMBAD and in GCVS (Vols I-III, IV).

  **2** NSV Supp. source not appearing in SIMBAD as variable.

  **3** GCVS (Vols. I-III) source not appearing in SIMBAD.

  **4** Name-list 74 source not appearing in SIMBAD as variable.

  **5** GCVS (Vol. V) source not appearing in SIMBAD.

  **a** Véron-Cetty & Véron (1998) source not appearing in SIMBAD as AGN (and subtypes) or Q?, or simply not appearing in SIMBAD.

  **b** Padovani (1998) source not appearing in SIMBAD as AGN (and subtypes) or Q?, or simply not appearing in Simbad and also not appearing in Véron-Cetty & Véron (1998).

  **c** Source from M. Mas (1998) compilation not appearing in SIMBAD as AGN (and subtypes), Q?, H2G, EmG, rG or BCG, or simply not appearing in SIMBAD and also not appearing both in Véron and in Padovani catalogues.

# Chapter 3

# TYC 2675- 663-1: a newly discovered accreting binary system

TYC 2675- 663-1 (with coordinates $\alpha$ = 20h9m11s, $\delta$ = +32°33m53s) was first monitored (in $V$ filter alone) by the Optical Monitor Camera (OMC) on-board the INTEGRAL satellite (Mas-Hesse et al., 2003) during the period of time MJD=52 594–53 961[1] as a part of a serendipitous program of optical monitoring of ROSAT sources. Cross-correlating the list of objects shown by OMC to be variable after the first months of operation, with the ROSAT catalogues, we found 5 sources, which potentially are optical counterparts of X-ray sources due to its close location to a ROSAT entry (inside the ROSAT 3$\sigma$ position error radius; Caballero 2004; Caballero-García et al. 2006). Optical variability with modulation being characteristic of binary systems was detected for 3 of them. In this Chapter we concentrate our study on TYC 2675- 663-1, which is located at 14" (with a catalog 1$\sigma$ position error of 8") from the ROSAT 1RXS J200912.0+323344 (contained in the RASS BSC). Since there was no previous information regarding this source, we engaged in both photometric and spectroscopic campaigns in order to disentangle the nature of this system. This source was classified in the OMCIC as IOMC 2675000078.

## 3.1 Introduction: optical counterparts of ROSAT sources

We obtained light curves for five targets from ROSAT catalogues and 3 of them showed a large degree of variability, typical of binary systems. There was no reported value for the periods of the systems elsewhere, so we calculated them without help of any previous measurement. To search for the period of these optically variable systems, we did a first scanning of the period value with a program based in the Phase Dispersion Minimization

[1]In the OMC, MJD is corrected from baricentring. The relationship between MJD and HJD is as follows: MJD=JD-2 400 000.5 .

**Table 3.1**: New ROSAT optically variable sources.

| ROSAT identifier | OMC identifier | TYCHO or HD name |
|---|---|---|
| 1RXS J095156.0+004722 | IOMC 0237000035 | TYC 237 -363 -1 |
| 1RXS J054101.8+203624 | IOMC 1306000026 | TYC 1306 -153 -1 |
| 1RXS J200219.0+333912 | IOMC 2674000067 | TYC 2674 -5404 -1 |
| 1RXS J200912.0+323344 | IOMC 2675000078 | TYC 2675 -663 -1 |
| 1RXS J095706.3-012019 | IOMC 4896000046 | HD 86222 |

**Table 3.2**: Periods obtained for the binary systems.

| TYCHO or HD name | Period (days) |
|---|---|
| TYC 237 -363 -1 | 0.46515±0.00018 |
| TYC 1306 -153 -1 | – |
| TYC 2674 -5404 -1 | – |
| TYC 2675 -663 -1 | 0.42233±0.00003 |
| HD 86222 | 0.9871±0.0008 |

method (Stellingwerf , 1978) as developed in our group of research. Visual inspection of the resulting light curves was used to choose the period that minimized the scatter in the light curves. In order to refine these coarse values obtained we applied a common method of determining the linear orbital ephemeris of an eclipsing binary by collecting times of minimum light, spanning as large an interval as possible and fitting them with a linear polinomium against cycle number. With this procedure, we took advantage of the very long base times of photometric observations covered by our photometric campaign of the binary systems. We took the mid-time of the eclipses as the minimum value obtained for a high-degree polinomium fitted to the data between start of the ingress and the end of the egress. Their periods and folded light curves are shown in Table 3.2 and Figures 3.1, 3.2 and 3.3. The 2 other variable objects have properties typical of pulsating stars, with irregular periods. For them we simply plot the light curves versus time (see Figures 3.4 and 3.5).

All these light curves indicate strong, and previously unknown, optical variability. For IOMC 0237000035 (or TYC 237 363 1) an optical counterpart was proposed before (Bade et al., 1998), which is the same that we have identified from its variability. IOMC 4896000046 is a known visual double binary or multiple system (with a visual separation of 0.56 arcsec), although no photometric light curve had been obtained before the OMC one.

In the following we summarize some optical properties of the counterpart candidates:

**IOMC 2675000078 = TYC 2675 663 1**

The possible optical counterpart of the X-ray source 1RXS J200912.0+323344 was identified with a star of $V \simeq 11.5$ and a color index of $B - V = 0.71$. Without considering the effects of extinction this may indicate a G0 spectral type. The star is located $14''$ apart from 1RXS J200912.0+323344 (with a catalogue $1\sigma$ position error of $8''$). The light curve (with a preliminary obtained orbital period of $0.42233 \pm 0.00003$ days) shows optical apparent variability that could be due to accretion processes occurring in the binary system, as confirmed in the analysis shown in Sections 3.2–3.4

**IOMC 0237000035 = TYC 237 363 1**

The potential optical counterpart of the X-ray source 1RXS J095156.0+004722 was identified with a star of $V \simeq 10.2$ and a color index of $B - V = 0.70$ (again corresponding roughly to F8 spectral type if interstellar absorption is neglected). It is positioned at a distance of $8''$ from 1RXS J095156.0+004722, itself with a catalogue $1\sigma$ position error of $19''$. The light curve (Figure 3.2), with obvious better quality than the previous case, also suggests an eclipsing binary system. This time, the estimated orbital period is $P = 0.46515 \pm 0.00018$ days.

**IOMC 4896000046 = HD 86222**

The optical counterpart of the X-ray source 1RXS J095706.3-012019 has been identified with the bright, $V \simeq 9$ , star HD 86222 that shows a color index of $B - V = 0.52$. Again neglecting any effect of interstellar reddening this may indicate an average F5 spectral type. The star is at a distance of $20''$ from 1RXS J095706.3-012019 (with a catalogue $1\sigma$ position error of $19''$). The light curve (Figure 3.3) clearly points to the presence of a detached close eclipsing binary with an estimated orbital period of $P = 0.9871 \pm 0.0008$ days. The analysis of this system is very attractive for the determination of stellar structure parameters given the expected spectral types or the component stars and the clean shape of the light curve. If confirmed as the optical counterpart of the ROSAT source we should be observing an active late-type binary with a period close to one day and, thus, difficult to observe in ground-based observatories.

**IOMC 1306000026 = TYC 1306 153 1**

This object is certainly not showing typical characteristics of eclipsing binaries and is the identified potential optical counterpart of the X-ray source 1RXS J054101.8+203

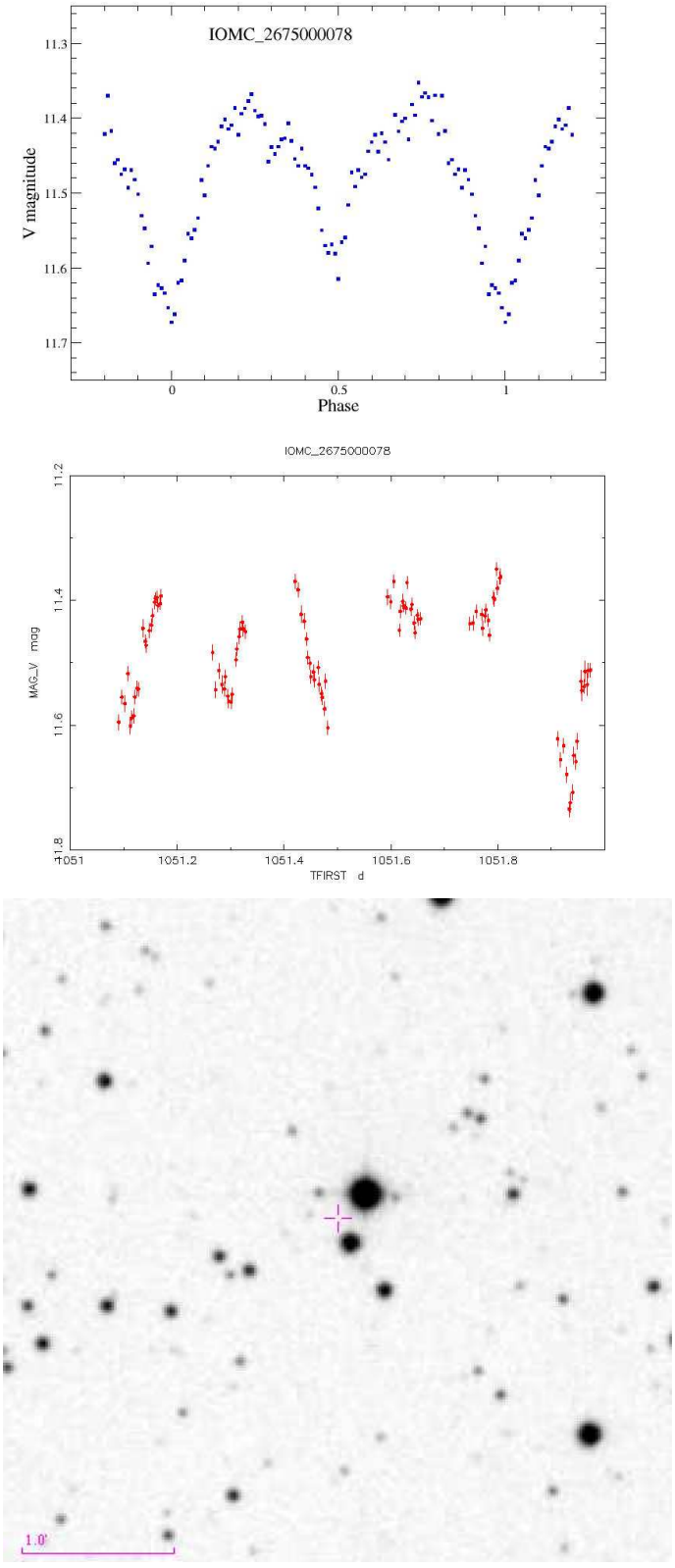


**Figure 3.1**: Folded light curve (blue) (with the period P = 0.42233±0.00003 d) and light curve versus time (red) of the eclipsing binary system TYC 2675 663 1. Digital Sky Survey (DSS) image showing the field of the target (the mark shows the position of the ROSAT source).

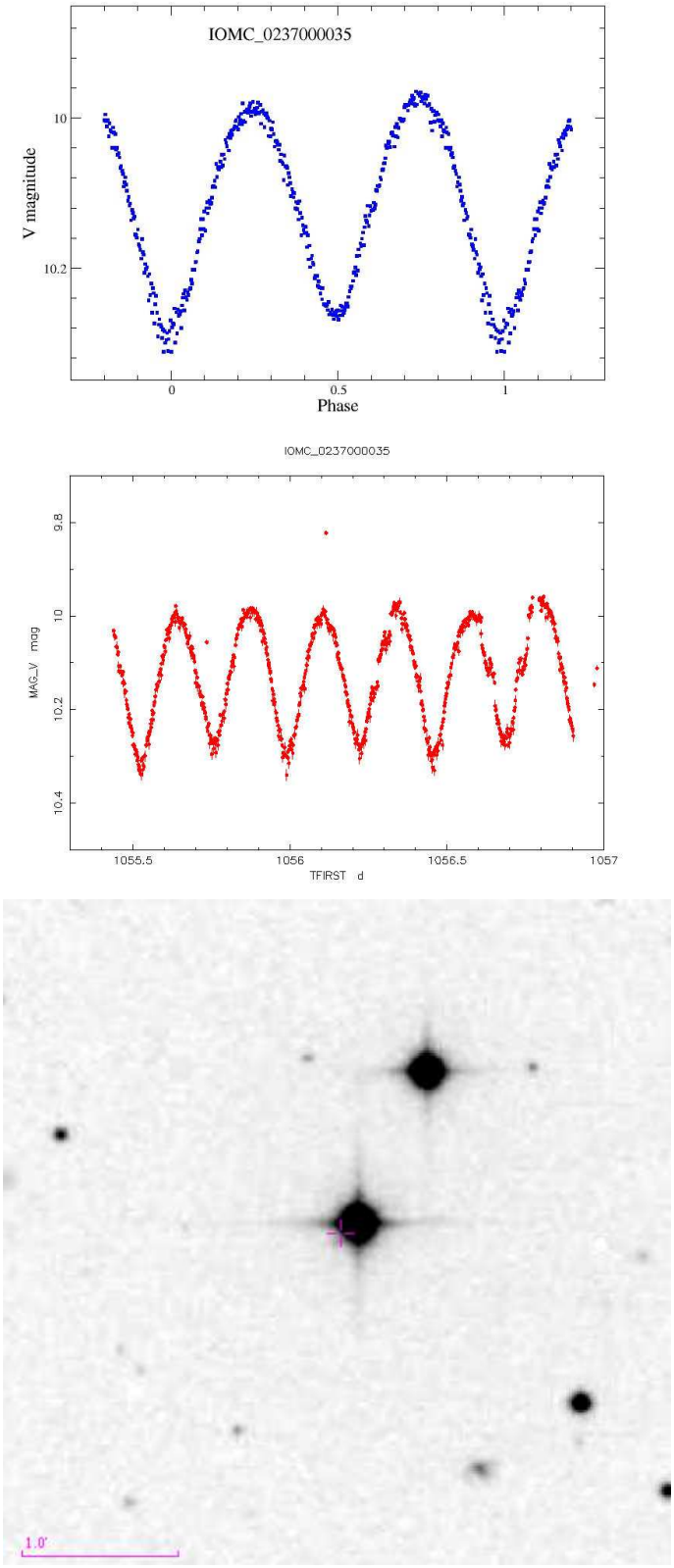


**Figure 3.2**: Folded light curve (blue) (with the period P = 0.46515±0.00018 d) and light curve versus time (red) of the eclipsing binary system TYC 237 363 1. Digital Sky Survey (DSS) image showing the field of the target (the mark shows the position of the ROSAT source).

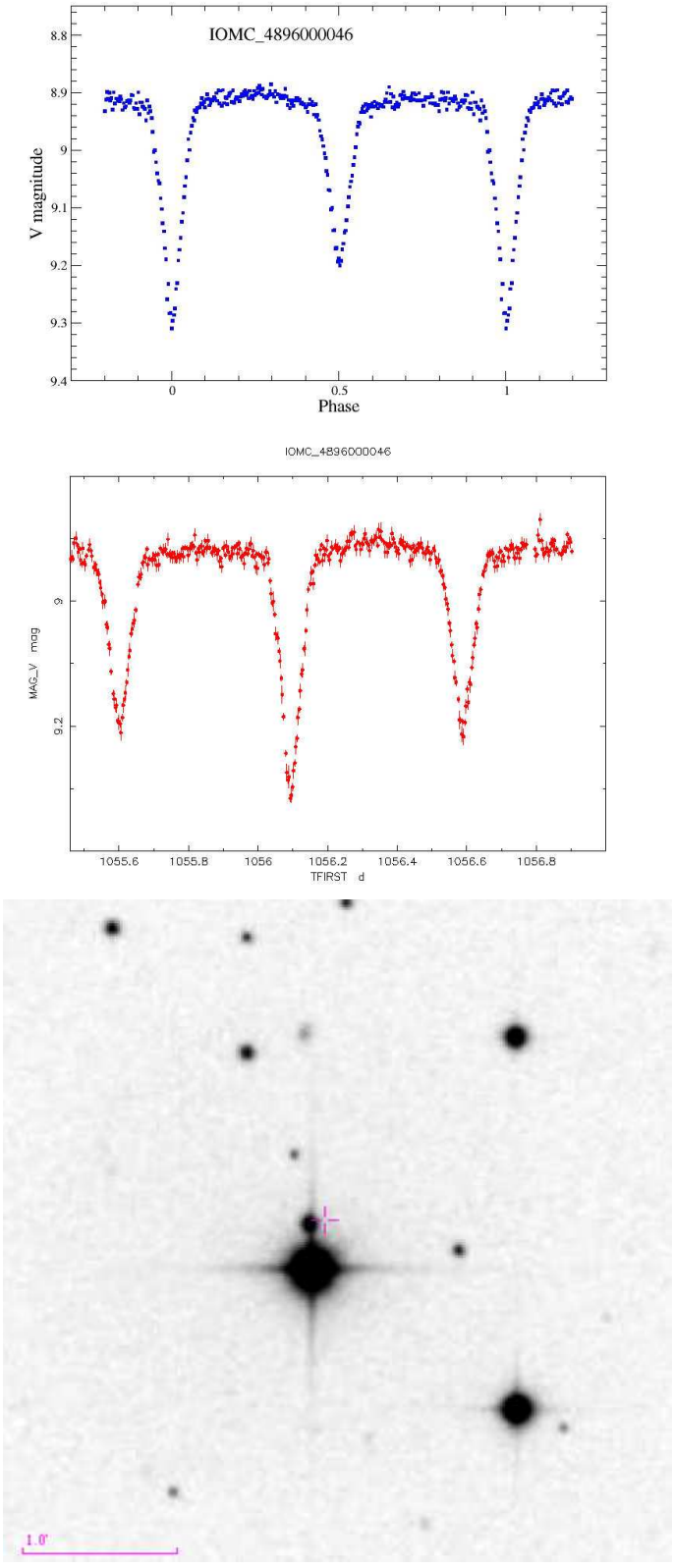


**Figure 3.3**: Folded light curve (blue) (with the period P = 0.9871±0.0008 d) and light curve versus time (red) of the eclipsing binary system HD 86222. Digital Sky Survey (DSS) image showing the field of the target (the mark shows the position of the ROSAT source).

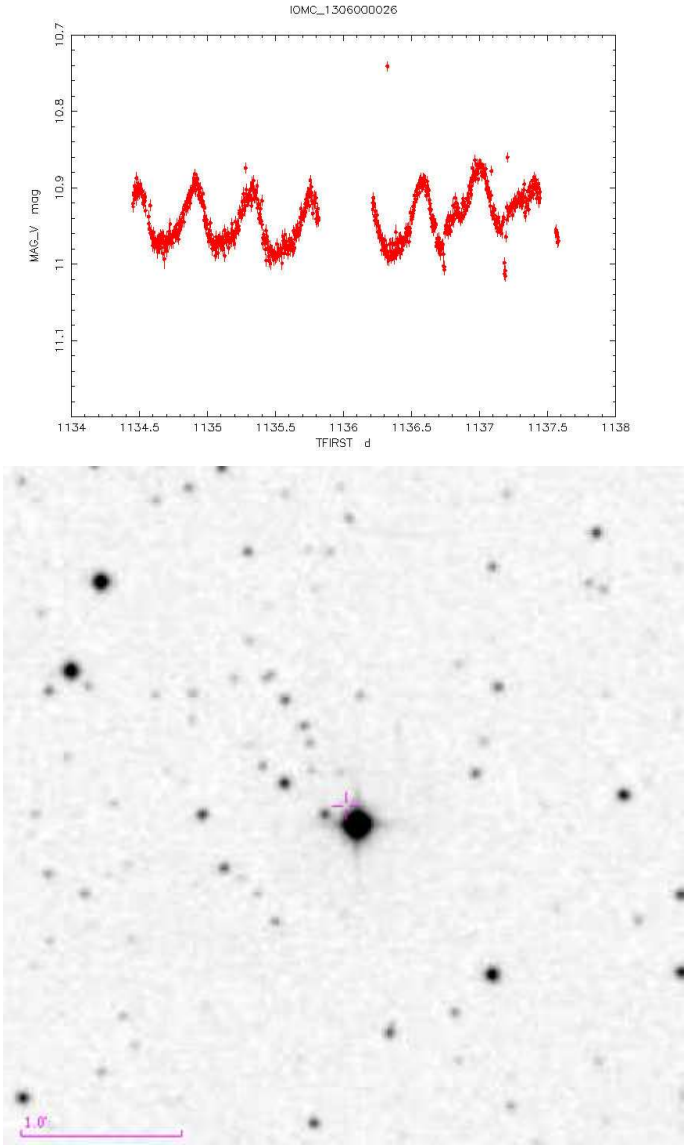


**Figure 3.4**: Light curves versus time of the pulsating stars TYC 1306 153 1 (top) and TYC 2674 5404 1 (bottom). Digital Sky Survey (DSS) image showing the field of the target (the mark shows the position of the ROSAT source).

**Table 3.3**: Optical and infrared colors from Cutri et al. (2003) and Tycho catalogues.

| TYCHO or HD name | (J-H) (mag.) | (H-K) (mag.) | (B-V) (mag.) | ST |
|---|---|---|---|---|
| TYC 237 -363 -1 | 0.29±0.03 | 0.099±0.03 | 0.70 | F8 |
| TYC 1306 -153 -1 | 0.50±0.03 | 0.155±0.03 | 0.99 | K2 |
| TYC 2674 -5404 -1 | 0.43±0.02 | 0.030±0.02 | 0.71 | G8 |
| TYC 2675 -663 -1 | 0.30±0.03 | 0.059±0.04 | 0.71 | G0 |
| HD 86222 | 0.19±0.02 | 0.061±0.03 | 0.52 | F5 |

624. The optical object shows $V \simeq 10.9$ and $B-V=0.99$, i.e. a late spectral type around K2 if there were no interstellar reddening of its light. The position of the star is at a distance of $8''$ from 1RXS J054101.8+203624 (with a catalogue position error of $10''$). The light curve type is perfectly consistent with an ellipsoidal or spot dominated type of variable.

**IOMC 2674000067 = TYC 2674 5404 1**

The last of the selected candidates, is the suspected optical counterpart of the X-ray source 1RXS J200219.0+333912. The star has a color index of $B-V=0.71$, thus an estimated G8 spectral type. Its location in the sky is the farthest from the high-energy source, at a distance of $41.7''$ from 1RXS J200219.0+333912 (with $1\sigma$ position error of $27''$). The light curve type is perfectly consistent with an ellipsoidal or spot dominated type of variable.

We could make a rough estimation of spectral types (ST) by taking the infrared (J, H and K colors from Cutri et al. 2003) and optical (B, V from the Tycho catalogue), with help of tabulated values in Cox (2000), and the resulting values are shown in Table 3.3. These are average values, and do not take into account reddening and multiple nature of some of these systems. With the information of the spectral types and the tabulated values for the intrinsic $M_V$ magnitudes of Cox (2000) we could estimate the distance to the systems (Tables 3.4 and 3.5). With these estimations for the distances and intrinsic $M_V$ luminosities it is possible to infer the intrinsic bolometric luminosity by taking tabulated Bolometric Correction (BC) factors from Cox (2000) and known $L_{bol}$, $M_V$ solar values (i.e. $L_\odot = 3.845\times10^{33}$ erg/s, $M_V$=4.74).

We used the known $L_X = L_{bol}\times10^{-3}$ relationship (Messina et al., 2003), to estimate the intrinsic X-ray luminosities (Table 3.5). These expected X-ray luminosities are systematically higher than the ones inferred from ROSAT observations except for TYC 2675 -663 -1. This might be due to the fact that ROSAT covers only a reduced X-ray energy range (0.1-2.4 keV). However, the X-ray excess of TYC 2675 -663 -1 with respect to the expected value is difficult to explain and this could be due to additional

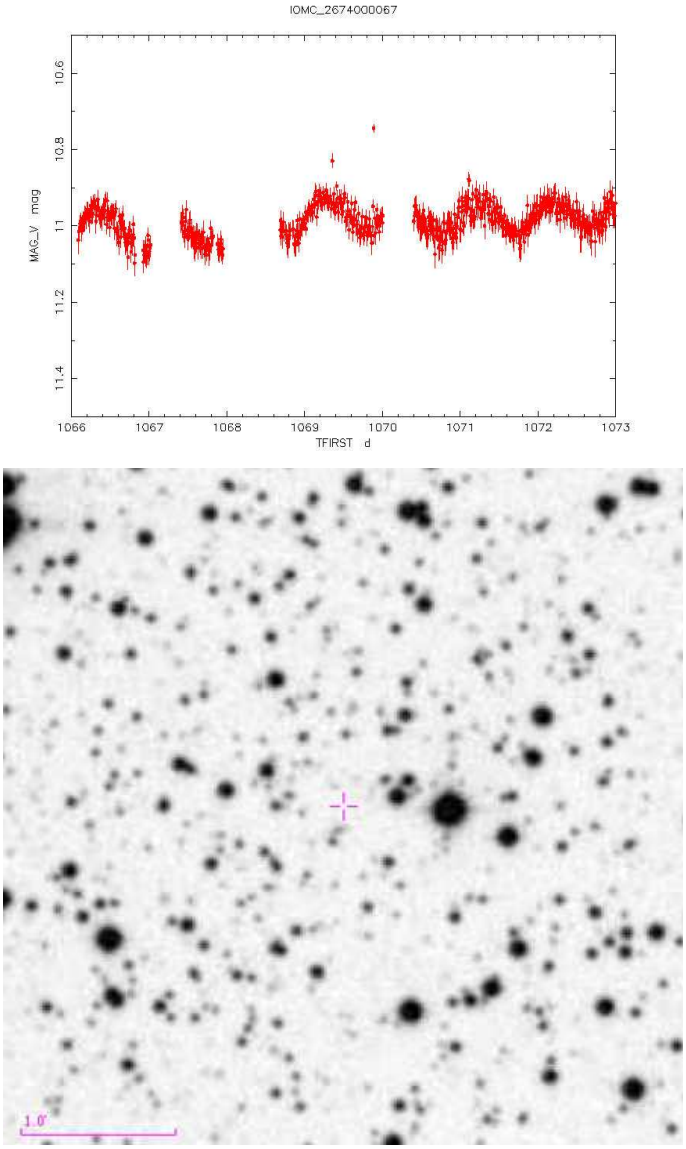


**Figure 3.5**: Light curves versus time of the pulsating star TYC 2674 5404 1 (top). Digital Sky Survey (DSS) image showing the field of the target (bottom; the red mark shows the position of the ROSAT source and the TYC source corresponds to the brightest one in a radius of 1', to the right in the image).

**Table 3.4**: Spectral types, bolometric correction factors and bolometric luminosities.

| TYCHO or HD name | Spectral type | BC | $M_V$ (mag.) | $L_{bol}$ (erg/s) |
|---|---|---|---|---|
| TYC 237 -363 -1 | F8 | -0.16 | 7.63 | $3.11\times10^{32}$ |
| TYC 1306 -153 -1 | K2 | -0.42 | 6.40 | $1.23\times10^{33}$ |
| TYC 2674 -5404 -1 | G8 | -0.40 | 5.50 | $2.76\times10^{33}$ |
| TYC 2675 -663 -1 | G0 | -0.18 | 4.40 | $6.21\times10^{33}$ |
| HD 86222 | F5 | -0.14 | 5.01 | $3.41\times10^{33}$ |

**Table 3.5**: Inferred X-ray luminosities from ROSAT data.

| TYCHO or HD name | Distance (pc) | $L_X$ (*obs.*) (erg/s) | $L_X$ (exp.) (erg/s) |
|---|---|---|---|
| TYC 237 -363 -1 | 148 | $1.15\times10^{29}$ | $3.11\times10^{29}$ |
| TYC 1306 -153 -1 | 76 | $1.09\times10^{30}$ | $1.23\times10^{30}$ |
| TYC 2674 -5404 -1 | 124 | $2.11\times10^{30}$ | $2.76\times10^{30}$ |
| TYC 2675 -663 -1 | 275 | $1.41\times10^{31}$ | $6.21\times10^{30}$ |
| HD 86222 | 138 | $1.07\times10^{30}$ | $3.41\times10^{30}$ |

effects not due to chromospheric activity of normal stars.

X-ray activity in normal stars (like the sun; as the ones presented in this Chapter except TYC 2675 -663 -1) is related with their rotational period (equal to the orbital periods, supposing synchronized orbits), as shown in Messina et al. (2003). This increases with the orbital period of the system up to saturation level (occurring at periods $\leq$0.3 d). This is due to the fact that magnetic activity of a normal star is directly related with its rotational period (Applegate , 1992). X-ray emission is a direct consequence of emission from a very hot (T$\approx$1 000 000 K) coronal plasma. The emission mechanism is bremsstrahlung, although other mechanisms as reflection and absorption are sometimes considered (Homan et al., 2003).

We conclude that the presence of an *X-ray excess* in TYC 2675 -663 -1 shows that this emission is not due to chromospheric activity occurring on the surface of the components of the binary system and other effects have to be taken into account.

## 3.2 TYC 2675- 663-1: follow-up observations

In the next Section we present the follow-up study we performed on TYC 2675-663-1, in order to better understand its properties. We present photometry taken with OMC and several telescopes in V, B and I Johnson filters as described in this Section. We obtained high resolution spectroscopy of TYC 2675−663−1 with the two channel spectrograph TWIN ($\Delta\lambda = 4\,400 - 5\,500, 6\,000 - 7\,100$ Å) at the 3.5 m telescope of the German-Spanish Astronomical Centre on the Calar Alto (hereafter called CAHA) in Spain taken during the night 2007 September 25. The timeline of the observations and instrumentation

used (both photometric and spectroscopic) are summarized in Table 3.6. Spectroscopy has the additional advantage over photometry that we can use our spectra to classify the parent star, deriving effective temperature, rotational velocity and surface gravity by correlating the observed spectra with a library of synthetic spectra, as we did in Section 3.3.2. From the analysis of high-resolution spectra, we report on the appearance of some interesting features as well (see Section 3.2.2).

This source also appears in the *XMM Slew source Catalogue* (Freyberg et al., 2006) as XMMSL1 J200910.0+323358 (located at 29.5″ from 1RXS J200912.0+323344). Its estimated unabsorbed X-ray flux in the (0.2-12) keV energy range is $(16\pm6)\times10^{-12}$ $erg/s\,cm^2$ (considering a column density of $N_H = 3.0\times10^{+20}cm^{-2}$). This confirms the detection of TYC 2675- 663-1 in X-rays. As explained above, single stars of F-M spectral type showing high rotation rates do emit strongly in soft X-rays due to enhanced chromospheric activity (Applegate , 1992), which is expected to be $L_X \approx 10^{-3} L_{bol}$, not increasing with periods $\leq$0.3 days because of saturation effects (Messina et al., 2003). For the same reason, binary systems composed by two F-M stars with rather short periods, like WUMa systems, are expected to emit strongly at X-rays ($L_X = 10^{+29} - 10^{+30}$ erg/s; McGale et al. 1996; Cruddace & Dupree 1984).

Both the instrumentation and the long time coverage allowed us to unveil the nature of the components and the configuration of the binary system as presented in Section 3.3. Finally, in Section 3.4 we discuss the results obtained.

As discussed in Chapter 2, for each INTEGRAL pointing, the OMC monitors the sources in its field of view by means of shots of variable integration time. Typical values in the range 10 to 200 s (currently 10, 50 and 200 s) are used to optimize the sensitivity and to minimize noise and cosmic-ray effects. In the analysis of TYC 2675- 663-1, only pointings with a duration of 100 and 200 s were kept, in order to get the measurements with proper signal to noise ratio. Telemetry constraints do not allow to download the entire OMC image. For this reason, windows were selected around the proposed X-ray/$\gamma$-ray targets as well as other targets of interest in the same field of view. Only sub-windows of the CCD with a size of 11×11 pixels (3.2'×3.2') containing those objects are transmitted to ground. The fact that TYC 2675- 663-1 is located 14" (with a catalog 1$\sigma$ position error of 8") apart from the ROSAT 1RXS J200912.0+323344 (contained in the RASS BSC) allowed us to monitor it. We got the magnitudes obtained from the processing of the overall data up to MJD=53 961 with the Off-line Scientific Analysis Software [2]. This resulted in 1 123 photometric points of data covering the time interval MJD=52 594–53 961. We used a photometric aperture of 5×5 pixels, because there were not problems of significant contamination by nearby sources (see Figure 3.6).

The long monitoring by OMC allowed us to discover that this source is a semi-

[2]Available in the web: http://isdc.unige.ch/?Soft+download

**Table 3.6**: Log of the observations reported in this work. See Sections 3.2, 3.2.2 and 3.3.2 for more details.

| Time interval (HJD-2 400 000.5) | Kind of observation | Telescope used |
|---|---|---|
| 52 594-53 961 | Photometry | INTEGRAL/OMC |
| 53 207-53 249 | Photometry | 0.5 m CAB/CAHA |
| 53 966-53 971 | Photometry | 1.52 m OAN/CAHA |
| 53 271-54 044 | Spectroscopy | 1.5 m Whipple Observatory |
| 54 306 | High-resolution spectroscopy | 3.5 m TWIN/CAHA |

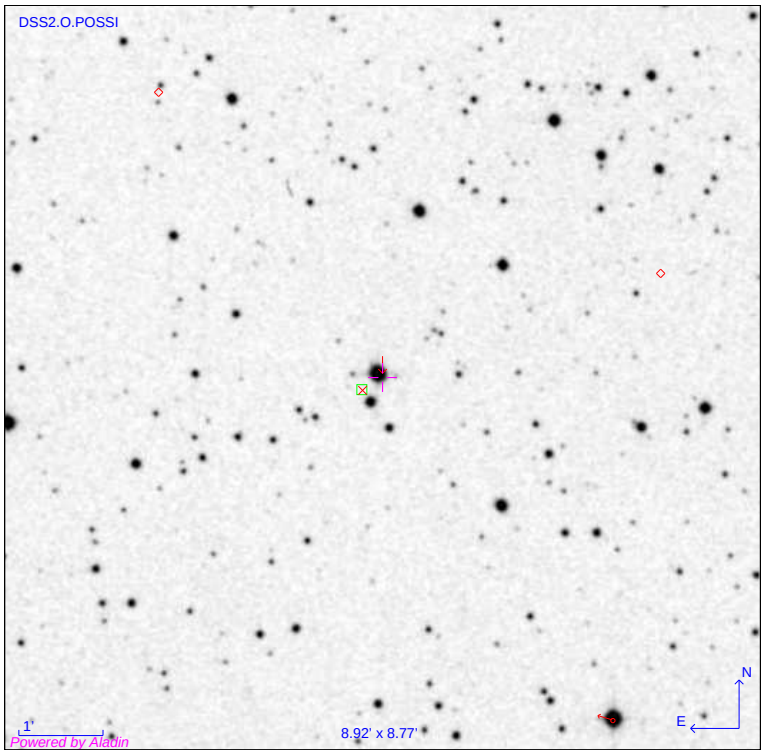


**Figure 3.6**: Field of view with our monitored target (TYC 2675- 663-1) (marked with an arrow) and 1RXS J200912.0+323344 (green square).

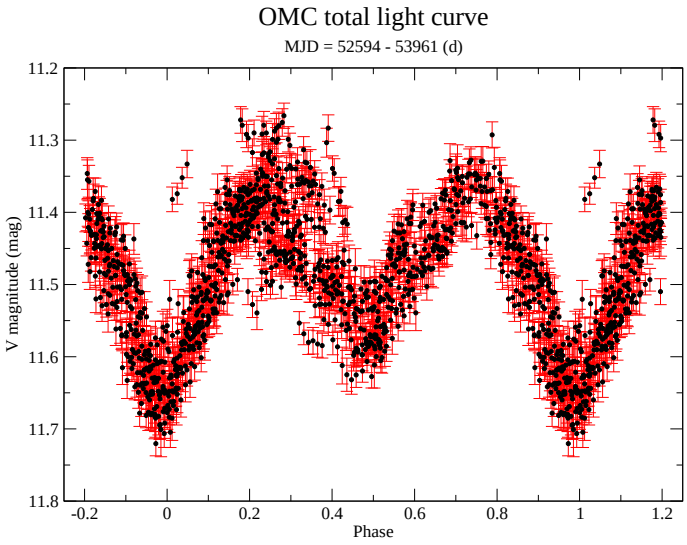


**Figure 3.7**: **Total** OMC light curve folded with the period of P=0.42235760±0.00000094 and HJD0(-2 400 000)=52 612.48048, the last being the time of the inferior conjunction of the secondary.

detached contact eclipsing binary with an orbital period of P=0.42235760±0.00000094 days (see Caballero 2004; Caballero-García et al. 2006 and Section 3.2.1 for both preliminary and detailed analysis, respectively). The total OMC light curve (covering 3.7 y of data) folded with this period is shown in Figure 3.7. This long monitoring also allowed us to unveil the peculiar shape of the minima ($\phi$=0,0.5), being occasionally highly asymmetrical (see Figure 3.8).

### 3.2.1 Ground-based photometry

Photometric observations were also obtained with the Robotic Telescope Giordano Bruno of Centro de Astrobiología (D=50 cm) located at Calar Alto. This telescope was equipped with a Finger Lakes Instrumentation IMG1024S 1024×1024 back-illuminated CCD and Johnson *BV* filters. The camera has an image scale of 0.97 arcsec pixel$^{-1}$, which results in a field of view of 16'×16'. We used two CCD cameras with very similar characteristics, one was used in the period of time HJD-2 400 000.5=53 208–53 236 and the other in the period of time HJD-2 400 000.5=53 236–53 250 (in Figure 3.9 we show the complete light curve assembling the data obtained from the two cameras). The working temperature of the CCD was −20° C which led us to take into account dark current correction in our images. All the images were corrected of bias current and flat field using the MIDAS analysis software. We derived differential photometry with respect to three comparison stars (with coordinates RA=20:08:57.822 Dec=+32:29:54.20,

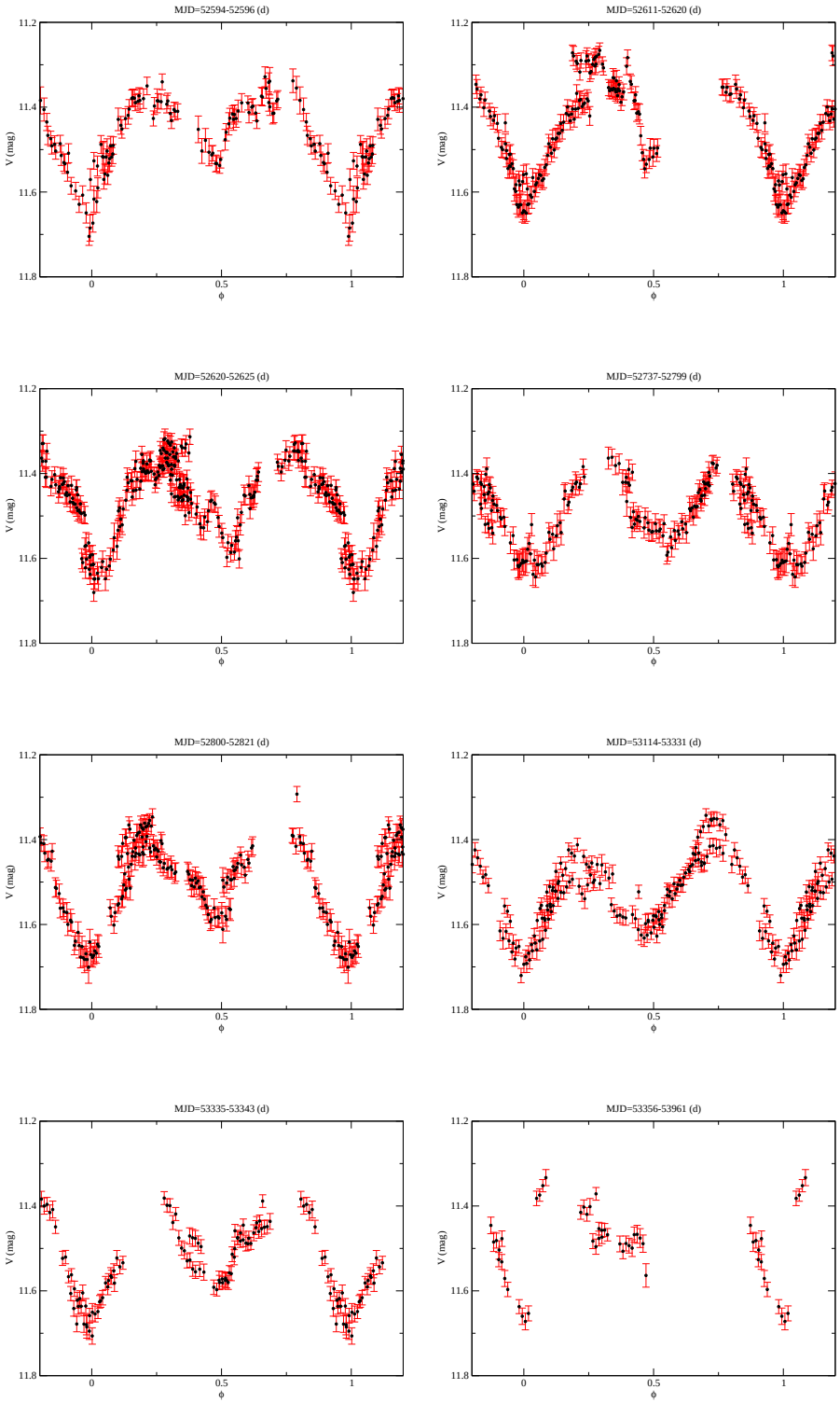


**Figure 3.8**: OMC light curves folded with a period of P=0.42235760±0.00000094 and HJD0(-2 400 000)=52 612.48048, the last being the time of the inferior conjunction of the secondary. The curves correspond to different periods of time.

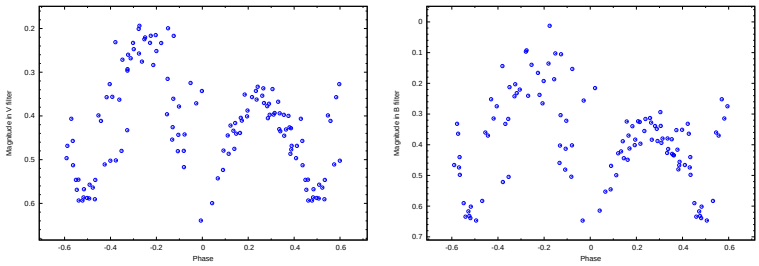


**Figure 3.9**: Light curves obtained with the Giordano Bruno Telescope (CAHA; HJD-2 400 000.5=53 207–53 249) folded with a period of P=0.42235760±0.00000094 and HJD0(-2 400 000)=52 612.48048, the last being the time of the inferior conjunction of the secondary.

RA=20:09:41.506 Dec=+32:27:49.47 and RA=20:09:42.516 Dec=+32:23:47.21) in the $V$ filter and four comparison stars (the same as the former plus another one with coordinates RA=20:09:46.011, Dec=+32:25:31.16) in the $B$ filter, using STARLINK/GAIA (for the astrometric calibration of the images) and Sextractor (for the photometric extraction of fluxes) analysis packages. This allowed us to obtain photometry for the source of $< 0.02$ mag precision for both $V$ and $B$, which is enough for our purposes.

In these observations we noticed a strong O-Connell effect (see Figure 3.9). This feature has been broadly reported for WUMa binary systems (Niarchos et al., 1997), and is usually associated to either accretion processes or chromospheric activity in the form of spots (Li et al. 2001; Yang & Liu 2001; Gu et al. 2004; Csizmadia et al. 2004; Kang et al. 2004; Niarchos et al. 1997). This is manifested as different magnitudes of the maxima (i.e. quadrature phases – $\phi = 0.25$,0.75 –) in the light curve ($\Delta V, \Delta B \approx 0.1$ mag). This effect is confirmed by OMC photometry simultaneous to these observations (MJD=53 114–53 331; see Figure 3.8). Such a large effect was only monitored before in the binary system [HH97] FS Aur-79 (Austin , 2007). This effect, jointly with the asymmetrical minima and presence of flares, form altogether part of the same physical effect, usually understood as evidence of chromospheric effects in the components of the binary. An alternative point of view was proposed by Liu & Yang (2001) who pointed out that the O-Connell effect is due to the circumstellar material that is being captured by the components of the binary system.

In order to obtain high precision photometry in the johnson $B$,$V$ and $I$ filters, we also carried out observations with the OAN Telescope (D=1.52 m) located at Calar Alto. These observations covered the period of time HJD-2 400 000.5 = 53 966–53 972. The telescope was equipped with a Photometrics Series 200 back-illuminated CCD and Johnson $BVI$ filters. The camera has a scale of 0.4 arcsec pixel$^{-1}$ and a field of view with a size of 6.9'×6.9'. The working temperature of the camera was $-115^{\circ}$ C, so it was not necessary to apply dark current correction to the images. We applied bias and flat field correc-

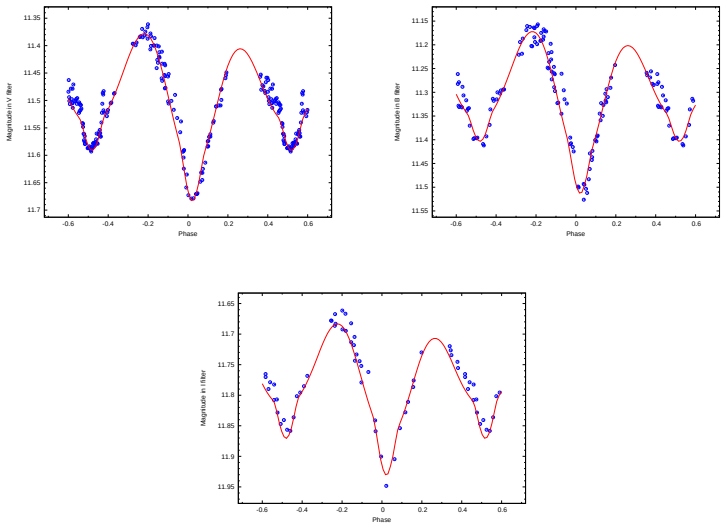

**Figure 3.10**: Light curves obtained with the OAN Telescope (CAHA) folded with a period of P=0.42235760±0.00000094 and HJD0(-2 400 000)=52 612.48048. The fit of the system (explained in Section 3.3.3) is represented as well (red solid line).

tion using the IRAF software. We derived differential photometry with respect to three comparison stars (with coordinates RA=20:09:09.21 Dec=+32:35:47.0, RA=20:09:23.0 Dec=+32:35:31 and RA=20:09:11.5 Dec=+32:36:21.0), selected from those field stars with low $(B-V)$ color indices (i.e. $< 1$). In the reduction procedure we used IRAF (bias and flat field corrections), STARLINK/GAIA (for the astrometric calibration of the images), Sextractor (for the photometric extraction of fluxes) and IDL software packages.

As can be seen from the light curves taken with OMC and OAN/CAHA, minima are characterized by being occasionally asymmetrical and showing erratic activity in the form of flares (MJD=52 797.825194 for the OMC and $\phi \approx -0.4$ for the OAN/CAHA light curves, prespectively; see Figures 3.8 and 3.10).

### Ephemeris of the eclipsing binary

An initial value of the period of TYC-2675-663-1 was derived using a method based on the Phase Dispersion Minimization algorithm of Stellingwerf (1978). In order to refine this period, we determined individual times of minimum from all our photometry data (INTEGRAL OMC, 0.5m Giordano Bruno Telescope, and 1.52m OAN) by fitting each eclipse with a high degree polynomial. A total of 59 timings were obtained (21 primary eclipses and 38 secondary eclipses), which are listed in Table 3.7. These were then used to establish the final period and reference epoch by solving for a linear ephemeris

using standard least-squares techniques. Primary and secondary minima were adjusted simultaneously, and the orbit was assumed to be circular. Given the asymmetry of the eclipses, realistic uncertainties are a bit difficult to determine. Instead, we assigned reasonable initial uncertainties by telescope, and then adjusted them by iterations so as to achieve reduced $\chi^2$ values near unity separately for the minima from each data set. In this way we established realistic errors of 0.011 mag, 0.012 mag, and 0.0065 mag for the OMC and the 0.5m and 1.52m telescopes, respectively. The resulting period and epoch are given by

$$P = 0.42235760 \pm 0.00000094 \,\text{days} \tag{3.1}$$

$$T(I) = 2453080.0249 \pm 0.0014 \,(\text{HJD}) \tag{3.2}$$

Where T(I) is the epoch value, chosen to be close to the mean value of all the timing minima. We detect no sign of period changes over the nearly 4-year interval. We adopt this ephemeris for the remainder of the Section.

### 3.2.2 High resolution spectroscopy

TYC 2675−663−1 was observed in 2007 July 25 from 22:02:06 (UTC) to July 26 01:02:24 (UTC) at the 3.5 m telescope at Calar Alto with the double-beam spectrograph TWIN, with a dichroic at 5500Å, yielding wavelength ranges from $\approx$ 4 400 Å to 5 500 Å and from 6 000 to 7 100 Å. The spectral resolution of this data is 0.54 Å/pix; thus $\approx$32 km/s in the red channel and $\approx$25 km/s in the blue one.

The sky conditions were photometric and the mean seeing was of 2″, enough for our purposes. Dome flat fields and bias were taken at the beginning of the night and comparison lamps spectra were taken regularly.

The full observation period covered is $\approx$3 h. The exposure time for each spectra was 600 s (resolution of 100 phase bins per orbital cycle). From the ephemeris obtained in Section 3.2.1 we inferred the orbital phase of the system corresponding to each spectrum (see correspondence in Figures 3.12 and 3.13). We began our spectroscopic observations almost coinciding with an inferior conjuction of the secondary of the binary system ($\phi = 0.05$) and evolved to the quadrature of the two components ($\phi = 0.25$). Thus, while these spectra do not serve for determining a well sampled radial velocity curve for the orbit determination (we used data from Whipple Observatory instead, as explained in Section 3.3.2, with a full coverage), their higher sensitivity allowed us to constrain important parameters of the system.

We extracted the spectra using the standard reduction procedures in the IRAF package (bias subtraction and flat-field correction). The extraction, sky subtraction, wave-

**Table 3.7**: Times of the observed mid-eclipses for the binary TYC 2675- 663-1 together with the cycle number (E) and the corresponding time difference (predicted from the ephemeris minus observed times).

| HJD-2 400 000.0 | $\sigma$ | $O-C$ | E | Year | Tel |
|---|---|---|---|---|---|
| 52595.58979 | 0.0110 | +0.00910 | -1147.0 | 2002.8764 | OMC |
| 52595.76130 | 0.0110 | -0.03057 | -1146.5 | 2002.8768 | OMC |
| 52595.99658 | 0.0110 | -0.00647 | -1146.0 | 2002.8775 | OMC |
| 52596.20278 | 0.0110 | -0.01145 | -1145.5 | 2002.8780 | OMC |
| 52596.43136 | 0.0110 | +0.00596 | -1145.0 | 2002.8787 | OMC |
| 52612.48048 | 0.0110 | +0.00549 | -1107.0 | 2002.9226 | OMC |
| 52617.96213 | 0.0110 | -0.00351 | -1094.0 | 2002.9376 | OMC |
| 52619.03278 | 0.0110 | +0.01124 | -1091.5 | 2002.9405 | OMC |
| 52620.29992 | 0.0110 | +0.01131 | -1088.5 | 2002.9440 | OMC |
| 52620.92656 | 0.0110 | +0.00441 | -1087.0 | 2002.9457 | OMC |
| 52621.76625 | 0.0110 | -0.00061 | -1085.0 | 2002.9480 | OMC |
| 52621.97140 | 0.0110 | -0.00664 | -1084.5 | 2002.9486 | OMC |
| 52622.18812 | 0.0110 | -0.00110 | -1084.0 | 2002.9492 | OMC |
| 52622.81180 | 0.0110 | -0.01095 | -1082.5 | 2002.9509 | OMC |
| 52623.03091 | 0.0110 | -0.00302 | -1082.0 | 2002.9515 | OMC |
| 52623.46205 | 0.0110 | +0.00576 | -1081.0 | 2002.9527 | OMC |
| 52624.30990 | 0.0110 | +0.00889 | -1079.0 | 2002.9550 | OMC |
| 52624.52707 | 0.0110 | +0.01489 | -1078.5 | 2002.9556 | OMC |
| 52624.71628 | 0.0110 | -0.00708 | -1078.0 | 2002.9561 | OMC |
| 52624.92494 | 0.0110 | -0.00960 | -1077.5 | 2002.9567 | OMC |
| 52737.71162 | 0.0110 | +0.00760 | -810.5 | 2003.2655 | OMC |
| 52746.76104 | 0.0110 | -0.02367 | -789.0 | 2003.2902 | OMC |
| 52797.69304 | 0.0110 | +0.01424 | -668.5 | 2003.4297 | OMC |
| 52798.32169 | 0.0110 | +0.00935 | -667.0 | 2003.4314 | OMC |
| 52798.73015 | 0.0110 | -0.00455 | -666.0 | 2003.4325 | OMC |
| 52798.95242 | 0.0110 | +0.00655 | -665.5 | 2003.4331 | OMC |
| 52799.16068 | 0.0110 | +0.00363 | -665.0 | 2003.4337 | OMC |
| 52800.62850 | 0.0110 | -0.00681 | -661.5 | 2003.4377 | OMC |
| 52800.86694 | 0.0110 | +0.02046 | -661.0 | 2003.4384 | OMC |
| 52801.26446 | 0.0110 | -0.00438 | -660.0 | 2003.4395 | OMC |
| 52806.33100 | 0.0110 | -0.00613 | -648.0 | 2003.4533 | OMC |
| 53208.40495 | 0.0124 | -0.01662 | 304.0 | 2004.5542 | 0.5m |
| 53209.46826 | 0.0124 | -0.00920 | 306.5 | 2004.5571 | 0.5m |
| 53220.45425 | 0.0124 | -0.00451 | 332.5 | 2004.5871 | 0.5m |
| 53224.49223 | 0.0124 | +0.02107 | 342.0 | 2004.5982 | 0.5m |
| 53231.42901 | 0.0124 | -0.01105 | 358.5 | 2004.6172 | 0.5m |
| 53231.65903 | 0.0124 | +0.00779 | 359.0 | 2004.6178 | 0.5m |
| 53233.53572 | 0.0124 | -0.01613 | 363.5 | 2004.6230 | 0.5m |
| 53235.44962 | 0.0124 | -0.00284 | 368.0 | 2004.6282 | 0.5m |
| 53250.43605 | 0.0124 | -0.01010 | 403.5 | 2004.6692 | 0.5m |
| 53324.15075 | 0.0110 | +0.00320 | 578.0 | 2004.8710 | OMC |
| 53324.59421 | 0.0110 | +0.02430 | 579.0 | 2004.8723 | OMC |
| 53330.06528 | 0.0110 | +0.00472 | 592.0 | 2004.8872 | OMC |
| 53330.49275 | 0.0110 | +0.00983 | 593.0 | 2004.8884 | OMC |
| 53336.39682 | 0.0110 | +0.00090 | 607.0 | 2004.9046 | OMC |
| 53336.82269 | 0.0110 | +0.00441 | 608.0 | 2004.9057 | OMC |
| 53342.29115 | 0.0110 | -0.01778 | 621.0 | 2004.9207 | OMC |
| 53342.74087 | 0.0110 | +0.00958 | 622.0 | 2004.9219 | OMC |
| 53357.09190 | 0.0110 | +0.00046 | 656.0 | 2004.9612 | OMC |

**Table 3.7**: (Continued.)

| HJD-2 400 000.0 | $\sigma$ | $O-C$ | E | Year | Tel |
|---|---|---|---|---|---|
| 53966.55612 | 0.0065 | +0.00265 | 2099.0 | 2006.6299 | 1.52m |
| 53967.39777 | 0.0065 | -0.00041 | 2101.0 | 2006.6322 | 1.52m |
| 53967.61149 | 0.0065 | +0.00213 | 2101.5 | 2006.6327 | 1.52m |
| 53968.44541 | 0.0065 | -0.00866 | 2103.5 | 2006.6350 | 1.52m |
| 53969.51250 | 0.0065 | +0.00253 | 2106.0 | 2006.6380 | 1.52m |
| 53970.36807 | 0.0065 | +0.01339 | 2108.0 | 2006.6403 | 1.52m |
| 53970.56628 | 0.0065 | +0.00042 | 2108.5 | 2006.6408 | 1.52m |
| 53971.40245 | 0.0065 | -0.00813 | 2110.5 | 2006.6431 | 1.52m |
| 53971.61272 | 0.0065 | -0.00904 | 2111.0 | 2006.6437 | 1.52m |
| 53972.46836 | 0.0065 | +0.00189 | 2113.0 | 2006.6460 | 1.52m |

length calibration (obtained by taking spectra of an HeAr calibration lamp) and normalization of the spectra were made with MIDAS and STARLINK/DIPSO standard procedures.

A sequence of normalized spectra in the range 4 400 to 5 400 Å and 6 400 to 6 700 Å showing the most interesting features is shown in Figures 3.11 and 3.12 for all the observations. One can see the strong emission Balmer ($H_\alpha$ and $H_\beta$) and HeI lines at $\lambda = 6\,563, 4\,861$ and 6 680 Å, respectively.

The HeI line is observed in emission above the continuum in all the spectra (see Figure 3.12). This emission is persistent during all the observations indicating that it is a very active binary system. Cataclysmic variables (Witham et al., 2007), novae (Williams , 1992) and accreting systems in general usually show Hα and He I in emission. The presence of He I has been associated to the presence of accretion in the form of either wind or accretion disk since long time ago (see Graham 1992 and references therein).

## 3.3 Analysis

### 3.3.1 The Hα emission line

Phenomenologically, the Hα complex is described by the presence of apparently two broad and asymmetric emission lines centered at 6 553 Å and 6 568 Å plus a variable absorption dip in between them.

An excess of emission can be appreciated simply by visual inspection. This is blue-shifted during the interval phase $\phi = 0.15-0.23$ (i.e. before quadrature of the system) and red-shifted during phases $\phi = 0.23-0.33$ (i.e. after quadrature of the system). There is also a variable absorption dip at the centre of the $H_\alpha$ complex, with slightly red-shifting with phase. This is centered at ≈6 560 Å, associated to a velocity of $v \approx -250$ km/s (with respect to the rest-wavelength of Hα at 6 563Å).

We can tentatively identify the $H_\alpha$ excess as arising from an accretion stream between the two components of the binary system. This component is blue-shifted during

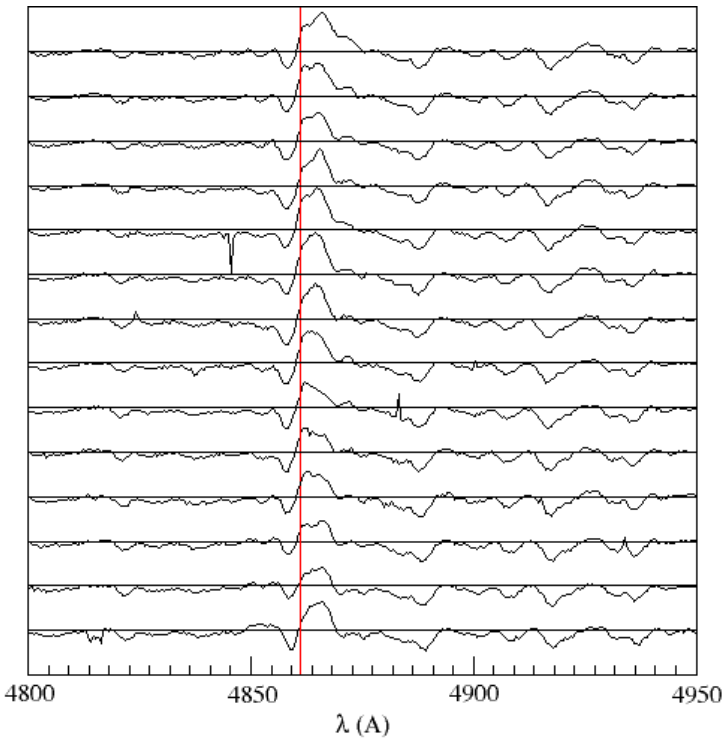


**Figure 3.11**: Blue spectra (4 800-4 950) Å showing the $H_\beta$ emission complex, centered at $\lambda_0 = 4\,861$ Å.

the phase interval $\phi = 0.15-0.25$ (highest peak emission from the blue-shifted component), which can be easily understood as an accretion stream of matter from the primary to the secondary component, evolving from the inferior conjunction of the secondary star ($\phi$=0) to the quadrature phase of both stars ($\phi = 0.25$). Afterwards, this excess becomes red-shifted during $\phi = 0.26 - 0.33$ (highest peak emission from the red-shifted component), and can be understood in the same way but now the accretion stream going outwards from our line of sight.

### 3.3.2 Radial velocity data of the eclipsing binary component

In collaboration with Dr. G. Torres (CfA/USA) we obtained broad spectroscopic data with a lower resolution instrument than TWIN in order to obtain well sampled spectra suitable for reproducing complete radial velocity data (over all the phases) of the system. We have used the CfA Digital Speedometers (Latham , 1992) on the 1.5 m Tillinghast Reflector at the Fred L. Whipple Observatory on Mount Hopkins, Arizona to obtain single order echelle spectra (R = 35 000) in a wavelength window of 45 Å centered at 5 187 Å with a resolution of 8.5 km/s. In total, we took 22 spectra from 2004 September 23 to 2006

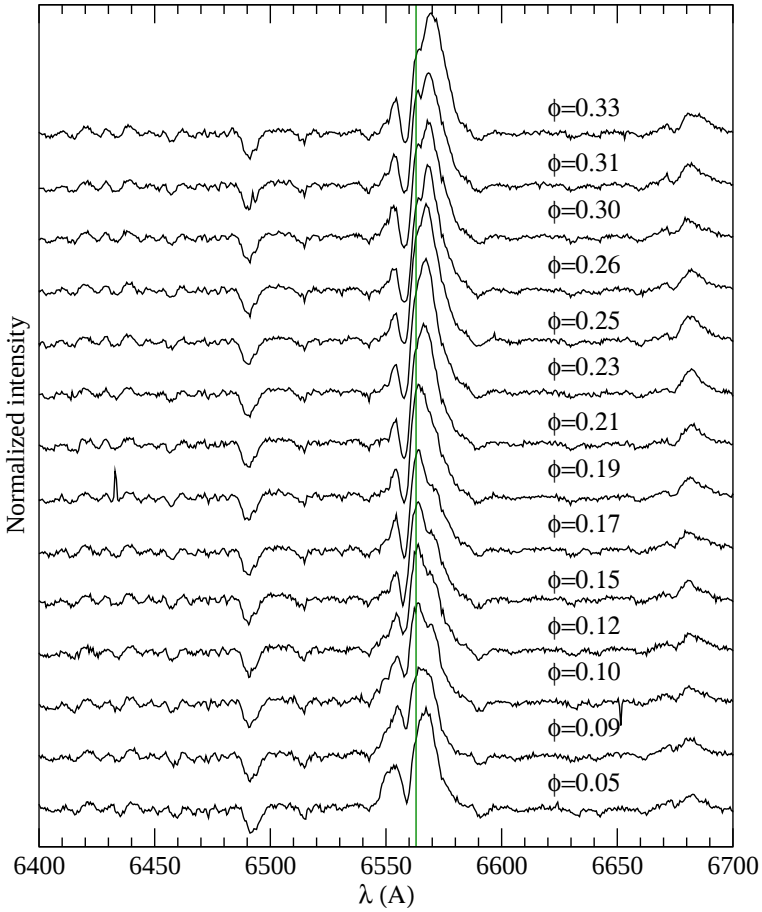


**Figure 3.12**: Red spectra (6 400-6 700) Å showing the prominent $H_\alpha$ and He I emission complexes, centered at $\lambda_0 = 6\,563$ Å and $\lambda_0 = 6\,680$ Å, respectively. The vertical line shows the rest-wavelength $H_\alpha$ emission line (6 563 Å; solid line).

November 5. The lines used are of absorption type, thus presumably being originated from the stellar chromospheres. Therefore, these would allow us to study stellar shifts.

We determined the radial velocities of TYC 2675- 663-1 by cross-correlation of the observed spectra against templates drawn from a library of synthetic spectra calculated by Jon Morse for a grid of Kurucz (1992) stellar atmospheres. The library grid has a spacing of 250 K in effective temperature, $T_{eff}$; 0.5 in log surface gravity, logg; and 0.5 in log metallicity relative to the sun, $[Fe/H]$. For the final radial-velocity determinations we adopted two templates with the $T_{eff}$, logg, and $V_{rot}$ values for both respectively the primary and the secondary component that gave the highest value for the peak of the correlation coefficient, averaged over all the observed spectra, assuming solar metallicity. For the correlation analysis we used **xcsao** (Kurtz & Mink, 1998) running inside the IRAF environment.

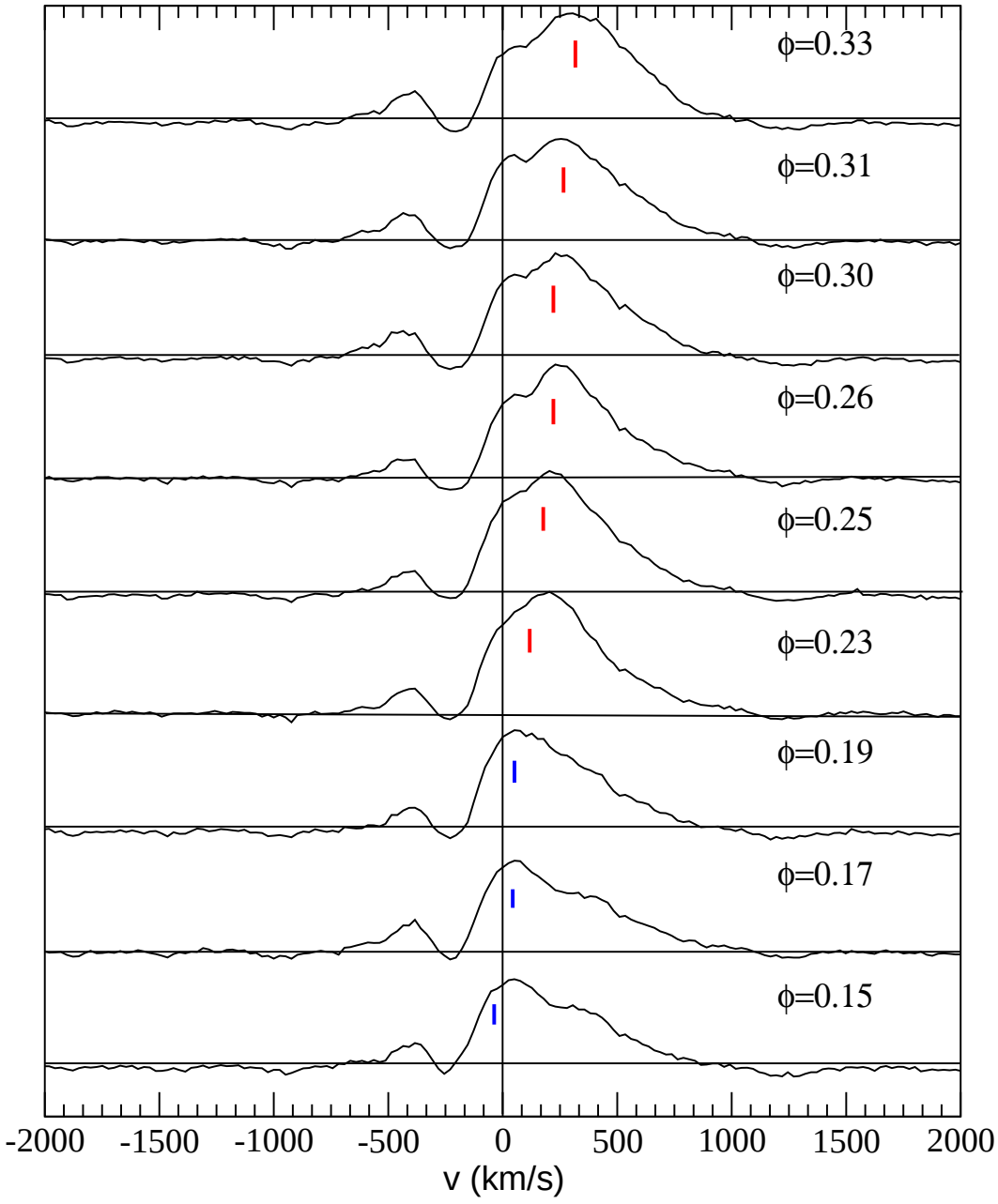


**Figure 3.13**: Red spectra showing the prominent $H_\alpha$ emission complex. Velocities are calculated with respect to $H_\alpha$ rest wavelength ($\lambda_0 = 6\,562.852$ Å). Both emission and absorption features are present (see Section 3.3.1).

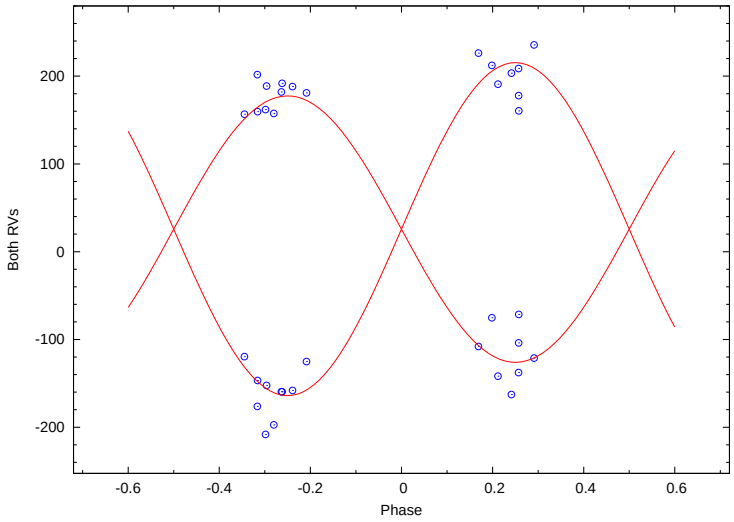


**Figure 3.14**: Radial velocity curves obtained in the Whipple observatory folded with P=0.42233±0.00003 and HJD0(HJD-2 400 000)=52612.48048 d. The fit of the system (explained in Section 3.3.3) is represented as well (red solid line).

These spectra revealed spectroscopic orbit with a period that matched the photometric period and an orbital semi-amplitude of about 152.7±5.9 and 189.1±7.0 km/s for the first and the second component, implying $q = M_2/M_1 = 0.808\pm0.045$). The center mass velocity of the system was found to be $v_\gamma = 26.8\pm4.4$ km/s. Altogether we accumulated 22 spectra yielding the radial velocities reported in Table 3.8, which were calculated using a template with tentative solar values for $T_{eff}$, logg and $V_{rot}$ for the primary and the secondary components, respectively. The parameters of our orbital solution for TYC 2675- 663-1 are reported in Table 3.9 and the corresponding velocity curves are plotted in Figure 3.14.

### 3.3.3 Light curve and radial velocity fitting of the eclipsing binary component

From modeling of both the light curves (in R, V and I filters) and radial velocity data we achieved a full characterization of the orbit (i.e. semi-major axis and inclination) and the components (i.e. radii, temperatures, potentials, velocities, masses). To this end we adjusted a numerical eclipsing binary model to the observations, using the W − D code, based on the Differential Correction Minimization algorithm of Lavenberg-Marquardt. We used the PHOEBE package tool (Prsa & Zwitter, 2005) (in its stable version 29c) with the LC and the RV data altogether for differential correction (DC) fits. The OAN/CAHA photometric data and the radial velocities obtained from the Whipple observatory of both

**Table 3.8**: Radial velocities obtained for the primary (1) and the secondary components (2).

| HJD-2 400 000 | $RV_1$ (km/s) | $RV_2$ (km/s) |
|---|---|---|
| 53271.6872 | 180.87 | -125.13 |
| 53272.7286 | -103.84 | 177.81 |
| 53273.7860 | 188.05 | -158.08 |
| 53275.6659 | -141.83 | 190.85 |
| 53278.6415 | -137.75 | 208.62 |
| 53280.7467 | -162.68 | 203.43 |
| 53281.6124 | -121.20 | 235.58 |
| 53281.7662 | 156.63 | -119.48 |
| 53282.6452 | 182.05 | -159.53 |
| 53301.6292 | 159.51 | -146.73 |
| 53308.6291 | -71.43 | 160.49 |
| 53684.7073 | 201.79 | -176.26 |
| 53686.6018 | -107.92 | 226.31 |
| 53690.6289 | 188.68 | -152.36 |
| 53691.6825 | -75.28 | 212.21 |
| 53693.5844 | 161.95 | -208.17 |
| 53873.9388 | 157.45 | -197.33 |
| 54044.5790 | 191.78 | -159.58 |

the components of the binary system were used to adjust the model.

We first fitted the radial velocity curves for obtaining the mass ratio and the preliminary semi-major axis and masses of the components. These quantities are straightforward to obtain in the case of circular and synchronous orbit from the radial velocity amplitudes ($K_1$ and $K_2$):

$$q = \frac{K_1}{K_2} = \frac{m_2}{m_1} \tag{3.3}$$

$$asini = \frac{P(K_1 + K_2)}{2\pi} \tag{3.4}$$

$$m_{1/2} sin^3 i = \frac{P K_{2/1} (K_1 + K_2)^2}{2\pi G} \tag{3.5}$$

where the indices 1 and 2 correspond to the primary and the secondary values, respectively. We supposed a first tentative value of $i = 90°$ for the inclination to get convergence of our fit. We further fixed the value of the Heliocentric Julian date origin and the period to HJD0(HJD-2 400 000)=52612.48048 d and P=0.42235 d, respectively. The former is referred to the time of occurrence of a primary minimum. By fixing a null small phase shift PSHIFT=0 we could make to coincide the primary minimum with phase zero.

For the light curve fitting we let free the inclination parameter [3]. The code was set in Mode 2 for detached binaries with no constraints on the potentials (except for the luminosity of the secondary component; computed from the other binary observables through a black body prescription, in our case). The simplest considerations were applied for the emission parameters of the stars in the model, that is, stars were considered as black bodies, approximate reflection model (MREF=1) was adopted, the third light was included but its contribution as derived from the fitting was very small (3% of the total flux). Gravity darkening exponents of $g_1 = g_2 = 0.3$ and bolometric albedos to Alb1 = Alb2 = 0.6 were set, as predicted for convective envelopes. Bolometric and $B$,$V$,$I$-bands limb-darkening coefficients were taken from van Hamme (1993). We adopted the mass ratio of $q = M_2/M_1 = 0.900\pm0.061$ from our radial velocity orbit. The temperatures were left free in the fit, because it is possible to obtain the absolute values from the primary and the secondary components through the fitting of the depth of the minima in different filters. We considered that the system has a circular orbit and both the components rotate synchronously ($F_1 = F_2 = 1$), as expected for a binary system with such a short orbital period. The radial velocity of the centre of mass of the binary system was fixed to the value obtained from the radial velocity orbit. Because of the highly asymmetrical primary minimum and strong O-Connell effect in the light curves we fitted two spots over the surface of the primary component to the data and the values obtained are reported in Table 3.9. The values obtained for the orbit and the components parameters are reported in Table 3.9 as well.

With the inclination of the orbital plane, which we found to be $i = 71°\pm4$, the values of the stellar masses, radii and temperatures for the components are $m = 1.4\pm0.2, 1.2\pm0.2\,M_\odot$, $R = 1.26\pm0.25, 0.39\pm0.10\,R_\odot$, and $T = 3\,800\pm30, 3\,400\pm30$ K for the primary and the secondary components, respectively. The bolometric absolute magnitude (see Table 3.9) of the secondary component is $M_{bol2} = 9.13$ and both the temperature and radius are in fair agreement with those expected for an M2 spectral type star. For the primary component, the bolometric absolute magnitude is brighter, with a value of $M_{bol1} = 6.11$, corresponding to a star of K2 spectral type. The temperature obtained for the primary component is cooler (i.e. $3\,800\pm30$ K) than expected (i.e. 4 830 K) and both the mass and the radius obtained (i.e. $1.4\pm0.2\,M_\odot$ and $1.26\pm0.25\,R_\odot$) correspond to an star of F5 spectral type rather than of an K2 spectral type. Because of the direct influence of spots or whatever mechanism responsible for the O-Connell effect, we are confident of the values reported for both the radii and masses (values always coincident from the fitting of several portions of the light curve obtained from different telescopes). This gives us a preliminary spectral classification of F5 and M2 for the primary and the secondary components, respectively. However, the mass obtained for the secondary (i.e.

[3]Corrections for the semi-major axis of the orbit were made in each iteration, supposing the quantity $a \sin i$ fully determined from the fits to the radial velocity data.

**Table 3.9**: Orbital parameters and astrophysical data for the components of the eclipsing binary derived from the best-fitting W-D model. Spots parameters (latitude, longitude, angular radius and temperature factor) over the primary surface are also shown

| Parameters | Value |
|---|---|
| P (days) | 0.4223576±0.00003 |
| i (°) | 71±4 |
| a ($R_\odot$) | 2.98 |
| $M_2/M_1$ | 0.80±0.05 |
| $v_\gamma$ (km/s) | 26.5±1.0 |
| $T_1/T_2$ | 1 |
| $M_2$ ($M_\odot$) | 1.2±0.2 |
| $R_1$ ($R_\odot$) | 1.26±0.25 |
| $R_2$ ($R_\odot$) | 0.39±0.10 |
| $S_1$ [a] | 1.875 |
| $S_2$ | 0.177 |
| $M_{bol1}$ (mag) | 6.11 |
| $M_{bol2}$ (mag) | 9.13 |
| $b_1$ (°) [b] | 57 |
| $b_2$ (°) | 143 |
| $l_1$ (°) [c] | 286 |
| $l_2$ (°) | 189 |
| $\Omega_1$ (°) [d] | 9 |
| $\Omega_2$ (°) | 9 |
| $T_{spot}/T_{surface}$ (1) [e] | 0.5 |
| $T_{spot}/T_{surface}$ (2) | 0.5 |

[a] Roche lobe filling factor; in units of the Roche Lobe surface

[b] Spot latitude (0 corresponds to the $+z$ pole and 180° to the $-z$ pole.

[c] Spot longitude (0 corresponds to the direction towards the other star and it goes to 360° in the counter clock-wise direction.

[d] Spot angular radius.

[e] Numbers smaller than 1 mean that the surface is dimmer than the surface.

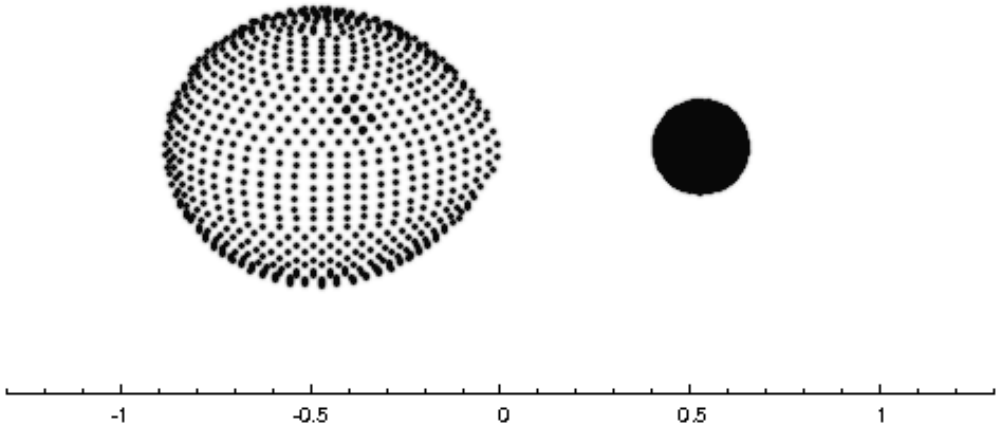


**Figure 3.15**: 3D representation of the TYC 2675- 663-1 binary system obtained from the fitted solution.

$1.2\pm0.2\,M_{\odot}$) disagrees with that corresponding of a star of M2 spectral type (i.e. $0.4\,M_{\odot}$) (Clemens et al., 1998). In Section 3.4 we discuss this issue in the context of similarities found in the literature.

Also interesting are the values reported for the Roche lobe filling factor (1.875 and 0.177 for the primary and the secondary components, respectively), which would indicate over-filling of the Roche lobe for the primary component (see Figure 3.15). This issue would be in agreement with the flaring activity observed at $\phi\approx -0.4$ (see Figure 3.10), the presence of He I $\lambda\,6\,680$ in emission (Graham 1992; Greeley et al. 1999; Takami et al. 2001; Scholz & Jayawardhana 2006) and spectral features of the $H_{\alpha}$ complex (Section 3.3.1) compatible with the presence of winds and accretion in the system (van de Steene et al. 2000; Dupree et al. 2007; Smolinski et al. 1993). All of these features (adding the ones interpreted as the O-Connel effect –asymmetrical minima and different magnitudes between consecutive maxima–) would be indicative of accretion taking in place in the eclipsing binary system as we will discuss in Section 3.4.

### 3.3.4 Distance to the system

During secondary eclipse the secondary star is mostly hidden, and the observed color will be that of the primary star. $(B-V)$ during secondary eclipse is about -0.18, which would correspond to a main secuence star with effective temperature of 15 200 K and spectral type of about B5. This is quite far from the value obtained from the light curve fitting of Section 3.3.3, from which we reported spectral type classification of F5. The B5 spectral type is unlikely because of the high $H_\alpha$ emission observed, if not attributed entirely to accretion processes. Also, the $(B-V)$ is affected by chromospheric activity and is not a good choice for determination of spectral types (Amado et al., 2003).

We thus suppose the primary star being of F5 spectral type and having an absolute V magnitude of $M_V = 3.5$ for the primary (Cox , 2000) and an apparent magnitude of the secondary minimum of V = 11.6; this gives $V - M_V = 8.1$ and a distance around 417 pc (about four times the distance to the Pleiades cluster).

## 3.4 Discussion

In this Section we report on both photometric and spectroscopic properties of TYC 2675- 663-1. The photometric properties involve episodic behaviour in the form of flares, asymmetrical minima and strong and variable O-Connell effect. These properties could be due to chromospheric activity in the surface of the components of this binary system or to accretion processes as previously reported (Liu & Yang 2003; Li et al. 2001; Yang & Liu 2001; Gu et al. 2004; Csizmadia et al. 2004; Kang et al. 2004; Niarchos et al. 1997). The last possibility was confirmed by high resolution spectroscopy revealing broad $H_\alpha$ and HeI lines in emission.

Very broad $H_\alpha$ emission ($\Delta$v$\approx$1 200 km/s) has been detected in the spectra of this binary system. This emission is complex, in the form of several components moving with orbital phase. The line shows a P Cygni profile dominated by absorptions associated to fast moving winds in the system. There are some previous studies showing the same effect in single pulsating stars and binary systems (Smolinski et al. 1993; Dupree et al. 2007; van de Steene et al. 2000; Scholz & Jayawardhana 2006; Graham 1992) on base of the H$\alpha$ emission line. All these features are variable and have properties of typical P Cygni profile. The absorption is too deep to be photospheric, hence the absorption must be produced outside the emission region. This shape is associated with the presence of a stellar wind and/or outflow in the system, typically seen in binary systems constituted by either a high-mass star (Varricatt et al. 2004; Chaty & Filliatre 2005), or a low-mass star (Ioannou et al., 2003) and, surprisingly, in X-rays from Nova like systems (as Cir X–1; Brandt & Schulz 2000). The velocity of the center of the absorption is similar to that of the stellar wind or higher. Similar wind velocities (-250 km/s) were found in other accreting binary

systems (-105 km/s; Smolinski et al. 1993; van de Steene et al. 2000). We can see in Figure 3.12 that the emission HeI line also shows P Cygni profile, thus confirming this feature coming from accretion processes instead of chromospheric ones.

As pointed out by O'Donoghue et al. (2003) if accretion occurs, the determination of the parameters of the components is highly disturbed. They proposed that a proper determination of the parameters of the M components of eclipsing binaries would arise by considering both rotational and accretion $H_\alpha$ components. As we showed in Section 3.3.3, some discrepancies between radii and masses were found and do not agree well with the determined radius/mass relationship for M dwarfs of Clemens et al. (1998). It is known that cataclysmic variables can suffer strongly variable mass transfer rates (Warner , 1995). Although TYC 2675- 663-1 does not seem to be of cataclysmic variable type (i.e. no recognisable planetary nebula is found), this kind of behaviour is noticed (see flare of $\phi \approx -0.4$) and variable asymmetries of the minima already seen in Figures 3.8 and 3.10. This would allow us to understand the large difference of the brightness of consecutive maxima seen in Figure 3.9, not seen in other epochs. The obtained X-ray intrinsic luminosity for TYC 2675- 663-1 is $L(0.2-12\,keV) = (3\pm1)\times10^{+32}\,erg/s$, implying an excess of ≈100% with respect to what is expected for a WUma system. This excess could be explained by the presence of an accretion disk (an excess of 20% was proposed by Retter et al. (2005) for the Algol system). Thus, it is tentative to associate TYC 2675-663-1 with a system undergoing drastic changes, may be becoming a cataclysmic variable in the future. Eventually, X-ray activity in the form of flares is expected to appear in this system.

## 3.5 Conclusions

In this Chapter we report on the discovery of three binary systems (TYC 2675 663 1, TYC 237 363 1 and HD 86222) on basis of their photometric properties, showing soft X-ray emission as seen from ROSAT catalogue. For two of them, the X-ray emission is the expected for highly rotating stars and due to chromospheric activity. For TYC 2675-663-1 the situation is different and an X-ray excess of ≈100% was detected. We performed both photometric and spectroscopic campaigns to unveil the origin of the X-excess and the nature of the components of the binary system as well. This resulted in the discovery of strong O-Connell effect, erratic behaviour in the form of flares and both asymmetrical minima and different brightness of maxima in the light curve. The spectroscopy allowed us to detect strong and broad $H_\alpha$ and He I in emission, with P Cygni shape, due to accretion processes and the presence of winds in the binary system. All these properties point out to this system being candidate of Algol system undergoing drastic changes, may be becoming a cataclysmic variable in the future. Eventually, X-ray activity in the form of flares is expected to appear in this system.

# Chapter 4

# The High-Energy Emission from GRO J1655–40

The origin of the high energy emission (X-rays and $\gamma$-rays) from black holes is still a matter of debate. In Chapters 4 and 5 we present new evidence that hard X-ray emission in the low/hard state may not be dominated by thermal Comptonization. We present an alternative scenario for the origin of the high energy emission that is well suited to explain the high energy emission from GRO J1655–40 and GX 339–4.

In this chapter, we present broadband (3−500 keV) INTEGRAL X-ray spectra and X-ray/optical light curves of the luminous black hole X-ray transient and relativistic jet source GRO J1655−40. Our analysis covers four Target of Opportunity observations of the outburst that started in February 2005. We find that the high energy emission from GRO J1655−40 can be modeled well with an *unbroken* power-law (with photon indices of $\Gamma = 1.72\pm0.03, 2.21\pm0.04$ for the first and the second observations, respectively). These correspond to hard and thermal dominant states, respectively. In contrast to many other black hole spectra, high energy complexity in the form of a break or cut-off is not required for the hard state, contrary to previous expectations for this state. We show for the first time that Comptonization by non-thermal electrons is the dominant process for the high energy emission in the hard state. We discuss our results in terms of models for broad-band emission and accretion flows in stellar-mass black holes.

## 4.1 Motivation

In this study we focus on black hole transients (i.e. binary systems constituted by a star and a black hole as the compact object). These systems usually spend long time in quiescence ($L_X \approx 10^{+33}$ erg/s) and become in outburst ($L_X \approx 10^{+37} - 10^{+38}$ erg/s) every few years. During the outburst, spectral evolution occurs, but always beginning and

ending in the low/hard state (described below).

### 4.1.1 The relativistic Fe $K_\alpha$ line

Emission below 10 keV can be due to a combination of thermal emission from the disk, and non-thermal emission from a corona. It is difficult to study disks through their continuum spectra, so the most pragmatic way to study the disk is to use broad Fe K emission lines. This line (as the reflection component that we will explain later) arises from the fluorescence of the inner disk from an irradiating source of high energy emission (George & Fabian, 1991). Depending on the ionization state of the disk this line is centered at 6.4-6.97 keV. From the study of the profiles of these lines, it can be inferred the spin of the black hole, which can be between zero for an Schwarzchild black hole (Fabian et al., 1989) to a maximally rotating regime in the case of a Kerr black hole (Laor , 1991). In the hard X-ray emission (E$\geq$10 keV) a spectral hump usually appears, called the reflection bump, with the same origin. Thus, both reflection and broad Fe $K_\alpha$ line should appear together during the observations. Nevertheless, both effects are inhibited when a high ionization degree occurs, because the disk becomes a perfect reflector of the $\gamma$-rays (Ross et al., 1999).

Current observations of relativistic lines suggest that a range of black hole spin parameters may be seen (for reviews, see Miller 2007; Nandra et al. 2007). It is therefore important to take relativistic effects into account by fitting spectra with the appropriate line and reflection models. Inner disks can get very close to the black hole (d$\leq$6 $R_g$) and this would imply a very concentrated source for the high energy emission, i.e., the high energy source has to be centrally compact.

### 4.1.2 The states of the black holes and related behaviour

In the most accepted picture for the black hole states (Tanaka & Lewin, 1995) the classification arises from the characterization of X-ray emission (usually a multicolor black body with an inner disk temperature of T $<$ 1 keV) and hard X-ray emission (E$\geq$20 keV), the last best phenomenologically described by a power-law. The high/soft state is characterized by strong disk emission ($>$ 25%) and an steep power-law ($\Gamma > 2.4$). The low/hard state has almost no disk emission and the power-law dominates the spectrum ($>$ 75%). During the Steep Power Law state (also called Very/High state) both disk and power-law emission are important, although $\Gamma$ is steep. During the evolution along the outburst some transitional states appear, called intermediate (Homan & Belloni, 2005) with characteristics of both low/hard and high/soft states, depending on the case.

Grove et al. (1998), on the basis of CGRO observations, proposed that the high/soft state of black holes is associated with an unbroken powerlaw, usually understood as non-thermal origin of the high energy emission. On the other hand, the low/hard

state was associated with an spectral cut-off at 100 keV (coinciding with the kinetic temperature of the thermal distribution of the -inverse- Comptonizing electrons), implying a thermal origin for the high energy emission.

### 4.1.3 The standard model

Sunyaev & Titarchuk (1980) proposed a thermal corona being the source of the high energy emission from black-holes. Some years later, Esin et al. (1997) proposed the standard disk plus coronae model. In this model, the inner disk goes inwards while the outburst evolves from the low/hard to the high/soft states. An advection dominated accretion flow (ADAF) corona fills the inner regions of the disk, providing the (inverse) Comptonizing electrons. The disk provides the photons to be Comptonized. This was considered to be the source of the high energy emission during the last 30 years.

However, the above mentioned model has several drawbacks. The first one is that the standard model can not explain the QPOs (Quasi Periodic Oscillations) behaviour. QPOs are the highest frequency oscillations in black holes (typically between 140 and 450 Hz) which are commensurate with Keplerian orbital frequencies at the ISCO (Inermost Stable Circular Orbit). X-rays QPOs appear in the low/hard state, are maintained in the intermediate states and are quenched in the high/soft state (see review by van der Klis (2004)). Also, there is an strong coupling between hard X-rays and radio emission, difficult to understand without taking into account hard X-ray emission from a jet. As can be seen in a recent review from Fender et al. (2004), black holes in the low/hard state show radio emission in the form of a steady jet with a low value for the Lorentz factor ($\Gamma < 1.4$). During the intermediate state the radio emission is variable and $\Gamma$ is higher. In the Steep Power Law state the radio emission is optically thin with a high value of $\Gamma > 2$. In the high/soft state the radio emission is quenched. While the proposed scenario in Fender et al. (2004) would be consistent with the first point of the standard model proposed by Esin et al. (1997), the source of the high energy emission in the low/hard state is still debated. The base of jets have been proposed to be the source of the high energy emission (Markoff et al. 2001, 2003, 2005). Nevertheless, the model of Markoff is only dedicated to hard X-ray domain ($E < 100$ keV).

### 4.1.4 The alternative to the standard model

Coppi (1999) developed the EQPAIR hybrid thermal/non-thermal (inverse) Comptonization model. This model can explain the excess (with respect a pure thermal model) of the high energy emission already observed in black hole states during the high/soft state ($E > 200$ keV). The physical mechanism of this model is that (inverse) Comptonization from a hybrid thermal and non-thermal distribution of particles (leptons) is the source of the high energy emission. The most important consequences of this model

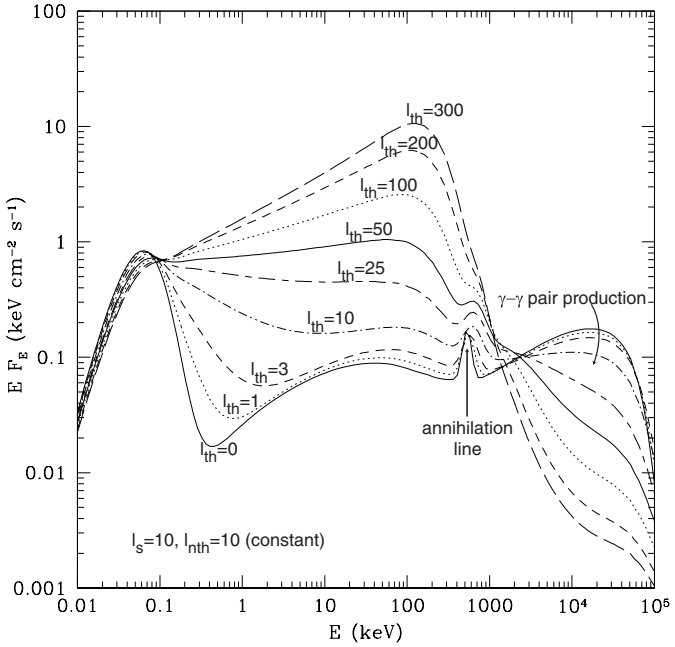


**Figure 4.1**: The transition from a non-thermal plasma ($l_{th} = 0$) to a thermally dominated plasma ($l_{th}/l_{nth} = 30$. The black-body spectrum has $T_{bb} = 15\,eV$. Figure adapted from Coppi (1999).

are both the disappearing of high energy cut-offs when the distribution of particles is highly non-thermal and the presence of the anihilation line at 511 keV. This line results from the anihilation of relativistic $e^+e^-$ pairs in mildly relativistic and non-thermal distributed plasmas. INTEGRAL and GLAST are key missions in the detection of this line. Several attemps have been attempted to detect this line from microquasars but still there are not fiducial detections (Guessoum et al., 2006). We think that this line, if detected, would confirm the hypothesis of the source of the high energy emission being highly concentrated and relativistic. These conditions would be the typical of the base of a jet. Although this model seems to be very promising it deals only with static coronae and, as shown in Beloborodov et al. (1999), if particles of the plasma acquire high velocities ($v/c \geq 0.2$), the high energy radiation is highly anisotropic.

## 4.2 Introduction

GRO J1655–40 is a black hole X-ray binary whose parameters are well known. Also called Nova Scorpii 1994, the source was discovered with the Burst and Transient Source Experiment on board the Compton Gamma Ray Observatory (CGRO) on 1994 July 27 (Zhang et al., 1994). The optical counterpart was discovered soon after by Bailyn

et al. (1995) ($V\sim$14.4 mag). Subsequent optical studies regarding the properties of the light curve during the outburst and quiescent period showed that the system is a low-mass X-ray binary composed of a blue subgiant (spectral type F4 IV) as the secondary and a black hole as the primary ($m_{\rm BH} = 7.02\pm0.22 M_{\odot}$; Orosz & Bailyn 1997). The system is located at a distance of 3.2 kpc as measured by Tingay et al. (1995). Although Foellmi et al. (2006) have suggested a smaller distance, their parameters imply that the donor star would not fill its Roche lobe. Bailyn et al. (1995b) established the orbital inclination of the system as $\simeq 70^{\circ}$ (see also Orosz et al. 1997; van der Hooft et al. 1998); an independent determination made by Kuulkers et al. (1998) based on X-ray flux dips constrained the inclination of the system to be $60^{\circ} - 75^{\circ}$. The inclination of the inner disk may be as high as $85^{\circ}$, indicating a slight misalignment with the binary system (Hjellming & Rupen, 1995).

GRO J1655–40 has displayed some of the most extreme behavior and phenomena yet observed from any black hole X-ray transient. Strohmayer (2001) discovered a pair of high-frequency quasi-periodic oscillations at 300 and 450 Hz in power spectra from the 1996/1997 outburst of the source. If the higher frequency is associated with the Keplerian frequency at the innermost stable circular orbit (ISCO; Shapiro & Teukolsky 1983), located at $R_{ISCO} = 6\ R_g$ for a Schwarzschild black hole or $R_{ISCO} = 1.25\ R_g$ in the case of a maximal Kerr black hole with $a = 0.998$ (where $R_g = GM/c^2$ is the gravitational radius and $a = cJ/GM^2$; see Bardeen et al. 1972; Thorne 1974), the frequency observed indicates that GRO J1655–40 harbors a spinning black hole. This suggestion is broadly consistent with spin estimates based on fits to skewed Fe K emission lines ($a \geq 0.9$ as per $r \leq 1.4\ R_g$; Miller et al. 2005). GRO J1655–40 has also ejected extremely relativistic radio jets (Hjellming & Rupen, 1995). Finally, unbroken power-law emission (i.e., without a cutoff) from GRO J1655–40 has been detected out to 800 keV (Tomsick et al., 1999), offering a crucial insight into high-energy processes in black hole systems.

High-energy processes and the periods of correlated behavior known as "states" in black hole binaries are the focus of this paper. Three active states are commonly recognized in the soft X-ray domain (see Remillard & McClintock 2006): the nonthermal-dominant or hard state (formerly called low/hard), the thermal-dominant state (formerly called high/soft), and the steep power law state. In addition, there are transitions between these states, which are often referred to as intermediate states. In the hard state, the soft X-ray emission is very weak and the spectrum is dominated by some kind of nonthermal emission that is broadly consistent with a power law at higher energies ($\gtrsim$20 keV). It has been known for a long time that black hole spectra in the hard state are exponentially cut off at $\sim$100 keV (see Grove et al. 1998 and references therein). A radio jet is usually inferred in this state from flat radio spectra (see Fender et al. 2004 for a unified model of X-ray states and radio emission in black hole X- ray transients). In the thermal-dominant

state, the disk dominates the X- ray emission. Although high-energy emission ($\gtrsim$20 keV) is also seen in this state, it is weaker and generally steeper and extends up to 800 keV without any break (Grove et al., 1998). In the steep power law state, these emission components are combined-both the disk and the nonthermal power law are strong, although the disk no longer follows the $L \propto T^4$ relation that is observed in the soft state (Kubota et al. 2001; Saito et al. 2007).

Several models have been proposed to explain the physical conditions in the innermost accretion flow and the nature of hard X-ray emission in the various states, but a clear picture has not yet been achieved. At low mass accretion rates, hard X-ray emission may arise in an inner region filled by a hot ($kT_e \sim$100 keV), radiatively inefficient, advection- dominated accretion flow (ADAF; Narayan 1996; Esin et al. 2001). A recent study by Yuan & Zdziarski (2004) shows that the ADAF scenario is not able to explain the relatively high luminosities that have been observed in the hard states of some black hole X-ray binaries. Alternatively, some recent models suggest that direct synchrotron emission, synchrotron self- Comptonization in a jet, or both may dominate the hard X-ray emission (Markoff et al. 2001, 2003, 2005). Both at low and at high mass accretion rates, thermal Comptonization in a corona (fed by seed photons from the disk) may also be an important source of hard X-ray emission (see, e.g., Frontera et al. 2003). An alternative source of Comptonization that is less reliant on the disk is bulk motion Comptonization (BMC; Ebisawa et al. 1996; see also Titarchuk & Shrader 2002 for a comoving Comptonizing medium). In this case, the Comptonization is due to bulk motion of an almost free-falling (convergent accretion) flow close to the black hole.

A thermal distribution of the Comptonizing particles (electrons) necessarily leads to a turnover in the emitted spectrum around kT; therefore, thermal Comptonization should lead to a turnover near the electron temperature of the corona, $kT_e$. Synchrotron emission and a nonthermal electron distribution do not necessarily predict such a turnover, however, and this difference provides an observational tool to distinguish which processes dominate the hard X-ray emission in different black hole states. The high-energy sensitivity of the International Gamma- Ray Astrophysics Laboratory (INTEGRAL) is especially well suited to this purpose.

In this paper, we report on observations of GRO J1655–40 made with INTEGRAL during the outburst that began in February of 2005 (Markwardt & Swank, 2005). In Section 4.3, we describe our observations, and in Section 4.4 we show the light curves obtained with the JEM-X, ISGRI, SPI, and OMC instruments on board INTEGRAL and with the Rossi X-Ray Timing Explorer (RXTE) and discuss the possible origin of their evolution. In Section 4.5, we present our spectral analysis made with JEM-X, ISGRI, and SPI. Finally, in Section 4.6 we discuss our results in the context of the different models and theories present in the literature.

## 4.3 INTEGRAL observations

The data cover the first part of the 2005 outburst and were obtained with INTEGRAL using the following instruments: the Spectrometer on INTEGRAL (SPI; Vedrenne et al. 2003), the INTEGRAL Soft Gamma-Ray Imager (ISGRI; Lebrun et al. 2003), the Joint European X-Ray Monitor (JEM-X; Lund et al. 2003), and the Optical Monitoring Camera (OMC; Mas-Hesse et al. 2003). ISGRI is optimized for 15 keV to 10 MeV imaging, and SPI is optimized for high-resolution spectroscopy in the 18 keV to 8 MeV band. The former provides an angular resolution of $12'$ full-width at half-maximum (FWHM) and an energy resolution $E/\Delta E$ of $\approx$12 (FWHM) at 100 keV. SPI provides an angular resolution of 2.8° (FWHM) and an $E/\Delta E$ of 430 FWHM at 1.3 MeV. JEM-X has a fully coded field of view (FOV) of 4.8° diameter and an angular resolution of $3'$ FWHM. JEM-X has medium-resolution spectral capabilities in an energy range of 3-35 keV. The OMC is an optical monitor with an FOV of 5°×5° and an astrometric resolution of better than $< 1$ arcsec and performs optical photometry in the V band down to 18th magnitude.

Our program consisted of four Target of Opportunity (ToO) observations of 100 ks each, spread from 2005 February 27 to April 11 (we refer to these as epochs 1–4 below; see Table 4.1 for more details). The difference in the exposure times between the INTEGRAL instruments given in Table 4.1 (JEM-X, ISGRI, and SPI) are due to differences in dead time and variations in efficiency along the fields of view. The dithering pattern used during the observations was 5×5 (a square of 25 pointings separated by 2.17° centered on the main target of the observation); this is the best pattern in order to minimize background effects for the SPI and ISGRI instruments in crowded fields. Data reduction (in the case of JEM-X, ISGRI, and SPI) was performed using the standard Offline Science Analysis (OSA, ver. 5.1) software package available from the INTEGRAL Science Data Centre (ISDC; Courvoisier et al. 2003). For SPI, because of the lower angular resolution and crowded field of view in gamma rays at this position of the sky [(l,b)=(344.98°,+2.46°); see Figure 4.2], we used a nonstandard procedure in the analysis of the data, described by Deluit (2005) and Roques & Jourdain (2005). For the same reason, in the case of the OMC we used a standard pipeline available in OSA version 6.0 for extraction of fluxes. For the OMC, all the public data available from the ISDC were downloaded (this resulted in only a slight increase in the amount of data). Because of the steep fall in response in the case of JEM-X, and because of its reduced FOV ($\approx$5° of diameter), we limited the pointing radius with respect to GRO J1655–40's position to be within 4°. In the case of SPI and ISGRI, with large fully coded fields of view (16°×16° for SPI and 8.3°×8° for ISGRI), pointing selections were not necessary. In total, 199 individual pointings (or Science Windows-each having an exposure time lasting from 1800 to 3600 s and following a 5×5 dither pattern on the plane of the sky; Courvoisier et al. 2003) were used for both SPI and ISGRI, 96 pointings for JEM-X, and 66 pointings for OMC.

**Table 4.1**: LOG of observations.

| Epoch number | INTEGRAL revolution & MJD (days) | Start & End Date (yyyy/mm/dd) | JEM-X [s] | ISGRI [s] | SPI [s] |
|---|---|---|---|---|---|
| 1 | 290 | 2005/02/27-28 | 44504.83 | 69212.87 | 90849.58 |
| | 53428.20-53429.50 | | | | |
| 2 | 295-296 | 2005/03/16-18 | 43641.93 | 71827.16 | 92584.05 |
| | 53445.10-53447.80 | | | | |
| 3 | 299 | 2005/03/26-28 | 44673.42 | 69848.25 | – |
| | 53455.80-53457.00 | | | | |
| 4 | 304 | 2005/04/10-11 | 46037.85 | 67883.58 | – |
| | 53470.00-53471.33 | | | | |

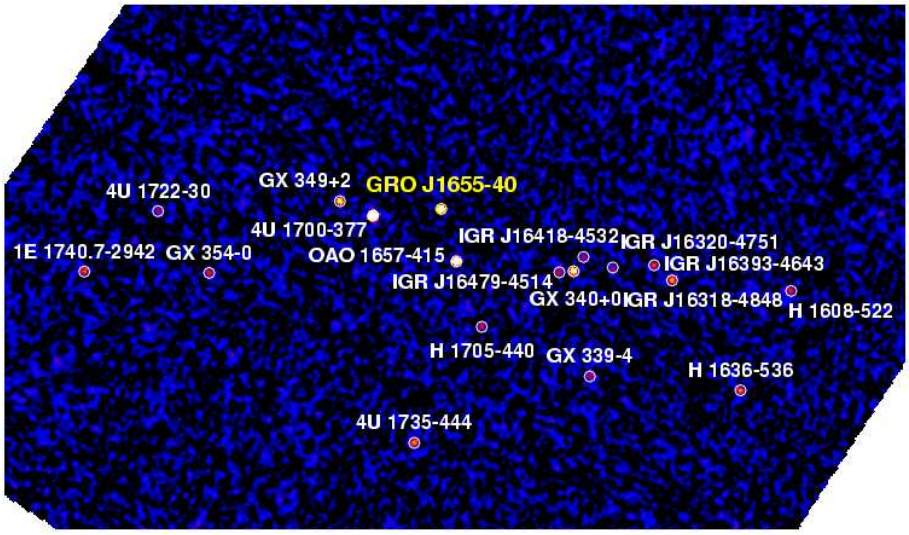


**Figure 4.2**: Mosaic significance image (obtained in revolution 295) of the GRO J1655-40 region as seen with ISGRI in the $20 - 40$ keV energy range. Besides the target, several other high energy sources are visible.

### 4.3.1 Extraction of Light Curves

GRO J1655–40 was covered with INTEGRAL as part of the Galactic Bulge Monitoring Program (Kuulkers et al., 2007). Precisely at the start of this program, GRO J1655–40 was reported to have become active (Markwardt & Swank, 2005). The subsequent outburst of GRO J1655–40 was also followed with the RXTE All-Sky Monitor (ASM) and with a dense program of pointed RXTE Proportional Counter Array (PCA) observations (Homan , 2005). In Figure 4.3, we show the ISGRI (20-60 and 60-150 keV), ASM (2-12 keV), and OMC (optical) light curves. The light curve derived from ISGRI in the 20-60 and 60-150 keV energy bands had 1800 s exposures (about 150 counts/s corresponds to 1 crab on-axis in the 20-60 keV energy band; see Appendix A of Kuulkers et al. 2007).

GRO J1655–40 was observed at a large off-axis angle (≈15° from the center of the FOV, so in the partially coded FOV of ISGRI and not visible with the X-ray monitor JEM-X).

Since GRO J1655–40 is located in a very crowded field for the OMC, in the flux extraction process we forced the photometric aperture to be centered at the source coordinates, which were taken from the OMC Input Catalogue (Domingo et al., 2003). The typical limiting magnitude of the OMC in the Galactic bulge is between $V = 15$ and $V = 16$ ($3\sigma$). This value depends strongly on sky background and source contamination. In our case [l,b)=(344.98°,+2.46°], we can confidently reach limiting magnitudes down to $V = 16$ ($3\sigma$). For each INTEGRAL pointing, the OMC monitors the sources in its FOV by means of "shots" of variable integration time. Typical values in the range 10-200 s (currently 10, 50, and 200 s) are used to optimize sensitivity and to minimize readout noise and cosmic-ray effects. For the faintest objects, several 200 s exposures in the same pointing can be combined during data analysis on the ground. We obtained one photometric point by combining several 200 s OMC shots. To increase the signal-to-noise ratio, we combined the individual photometric points of every pointing and calculated the final photometric points by taking running averages in order to minimize the dispersion.

### 4.3.2 Extraction of Spectra

For JEM-X and ISGRI, individual spectra were obtained for each pointing. The spectra were then combined to obtain an averaged spectrum per epoch using the `spe pick` OSA tool and standard procedures (see Chernyakova 2005; Chernyakova et al. 2005) to rebin the response matrices. In the case of SPI, we directly derived one spectrum per revolution. The SPI spectra were extracted over an energy range of 23-800 keV (with 26 logarithmic bins) using the SPIROS package within OSA, applying maximum likelihood optimization statistics (Skinner & Connell, 2003). Because of the crowdedness of the field and the low spatial resolution of the instrument (sources separated by less than 2.8° cannot be resolved), it was necessary to apply special techniques to extract spectra (see Roques & Jourdain 2005; Deluit 2005). These included accounting for variability of the sources present in the FOV. The background [1] was determined by using flat fields from particular INTEGRAL revolutions (revolution 220 in our case –the publicly available flat field closest in time to our period of observations), and the use of background method 3 (determination of the background based on some specific flat-field INTEGRAL observations). Because SPI is a high-resolution spectrograph in its energy range (20-8000 keV) with a reduced

[1] Due to the fact that JEM-X, ISGRI and SPI are detectors based in coded mask optics, the detection of sources is made in basis of a deconvolution process, taking also into account background, in an iterative process called IROS (Iterative Removal Of Sources). In OSA 5.1 the spectra obtained are always background subtracted and it is not necessary to apply in XSPEC any background correction to the obtained spectra. The light curves obtained are also background subtracted. However, in JEM-X analysis it is possible to skip the level of background subtraction. We refer to the Roques et al. 2005b, Goldwurm et al. 2003, Westergaard et al. 2003 and Dubath et al. 2005 for more details.

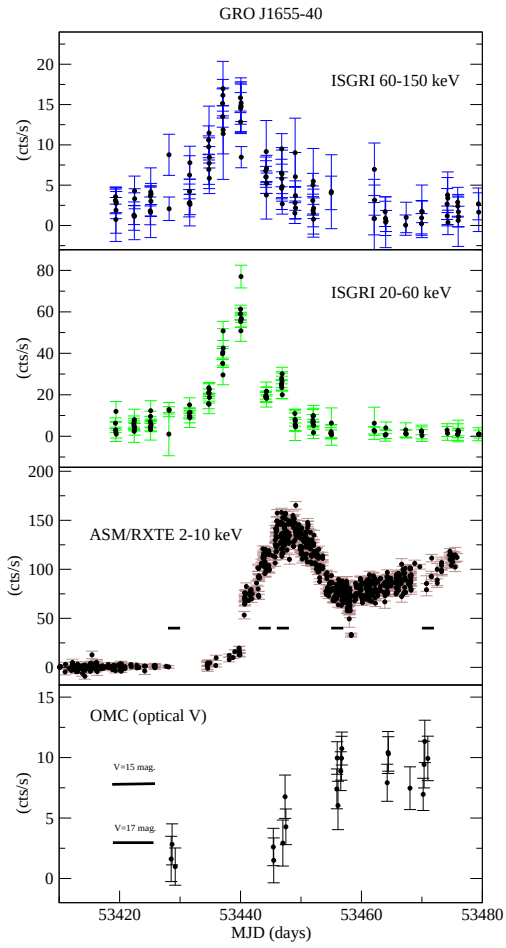


**Figure 4.3**: Light curves obtained with ISGRI from the INTEGRAL Galactic Monitoring Program in two energy bands (60-150 keV and 20-60 keV), together with the OMC (optical) light curve. The horizontal lines in the OMC panel show the equivalent magnitudes of the fluxes. In the third panel, the ASM/RXTE (2-12 keV) light curve is shown in the same period. The horizontal lines indicate the time intervals (one revolution each) over which the INTEGRAL spectra were obtained.

number of detectors (namely, 19), it is not optimized for the detection of sources without taking into account previous information about their spatial distribution. Thus, we used as an input catalog of sources those obtained from ISGRI in the (20-40) keV mosaic images (see Figure 4.2).

The signal from GRO J1655–40 was too soft to detect any emission in the last two epochs with SPI. We combined single-revolution SPI spectra from each epoch, since there was no significant evolution and in order to increase the signal-to-noise ratio. This resulted in one SPI spectrum in revolution 290 and another one combining revolutions 295 and 296. The same was done for the low-energy instruments (JEM-X and ISGRI), thus yielding four spectra, namely, one for each epoch, as can be seen in Table 4.1. We applied 2% systematic errors to the JEM-X, ISGRI, and SPI spectra. We restricted ourselves to the energy ranges 5-30, 23-600, and 23-800 keV for the JEM-X, ISGRI, and SPI spectral analysis, as recommended by Lubiński et al. (2005). The SPI and ISGRI spectra were rebinned at high energies ($\gtrsim$200 keV) with the FTOOLS grppha procedure to reach a detection level of $3\sigma$.

## 4.4 Analysis of light curves

Figure 4.3 shows the GRO J1655–40 light curves obtained with ISGRI (from the INTEGRAL Galactic Bulge Monitoring Program; Kuulkers et al. 2007) in two energy bands (60-150 keV and 20-60 keV), together with that from OMC (optical). The public RXTE ASM (2-12 keV) light curve for the same period of time is also shown for comparison.

The light curves in Figure 4.3 show the first month of outburst of GRO J1655–40. For a full outburst light curve, see Brocksopp et al. 2006), where the X-ray light curve obtained by Swift is shown jointly with that obtained in the optical and ultraviolet band using the Ultraviolet/Optical Telescope (UVOT) on board Swift. In Figure 4.4, we show the RXTE PCA light curve in the 2-60 keV range plus the evolution of the hardness ratio (calculated as the ratio of the 9.4-18.2 keV and 2.8-5.7 keV count rates) during the entire outburst, taken from Homan et al. (2007). The light curves were made from 520 RXTE observations, with one (averaged) data point for each observation. The horizontal lines shown in Figures 4.3 and 4.4 indicate the time intervals (100 ks each, in four observations) over which our average spectra were obtained. Note that black hole transients usually begin and end their outbursts in the hard state (see Nowak 1995; Fender et al. 2004; Homan & Belloni 2005), and the 2005 outburst of GRO J1655–40 is no exception. As can be seen in Figure 4.3, the beginning of the outburst started at high energies (20-150 keV) rather than with softer X-rays (2-10 keV). Moreover, as can also be seen from the hardness ratios in Figure 4.4, the observations of epoch 1 correspond to the hard state (see § 5).

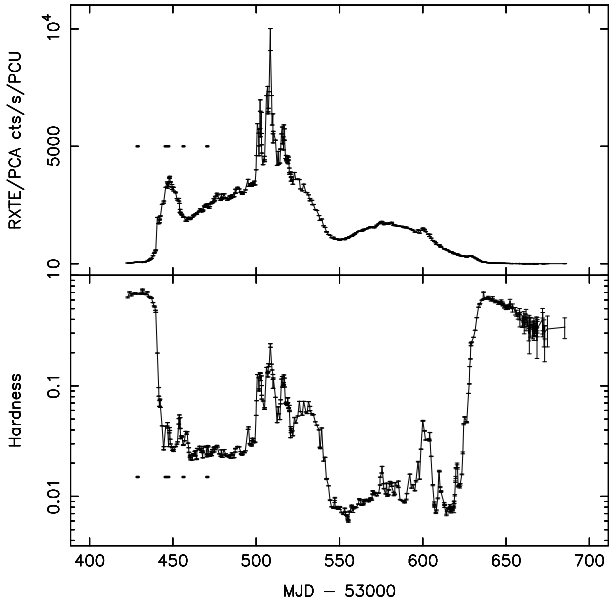


**Figure 4.4**: RXTE PCA light curves in the 2-60 keV band (top) and hardness ratio calculated as the ratio of the 9.4-18.2 keV and 2.8-5.7 keV count rates (bottom). The curves were made from 520 RXTE observations, with one (averaged) data point from each observation. Data taken from Homan et al. (2007) (in preparation).

The other three epochs were during a period when the source spectrum was much softer. However, it should be noted that it was only later in the outburst that the softest spectra (corresponding to the thermal-dominant state) were observed (see Figure 4.4).

The first indications of an impending outburst of GRO J1655–40 came from RXTE PCA bulge-scan observations on 2005 February 19 (Markwardt & Swank, 2005). On February 20, observations made with the PANIC instrument on the Magellan 6.5 m Baade Telescope at Las Campanas Observatory revealed a J- band (near-infrared) magnitude of 13.2±0.1 (Torres et al., 2005), indicating that GRO J1655–40 was brighter by ≈0.5 mag in J relative to its magnitude in quiescence (J = 13.7-14; Greene et al. 2001). On the same date, a radio detection of the source was reported (Rupen et al., 2005).

As can be seen from Buxton & Bailyn (2005) and Brocksopp et al. (2006), the optical light curve behaves differently from the X-ray. The optical behavior consists of an increase in flux up to a constant level at MJD 53,455. This behavior can also be seen with the OMC, because the flux in the optical light curve was increasing, reaching a constant and detectable value ($V \sim 15$ mag) at MJD 53,455. Then the optical flux became constant. It is also interesting to note the rapid increase of the radio emission at MJD≈53,450, coinciding with our epoch 3 of observations and also with the beginning of the plateau in both the optical and infrared light curves.

## 4.5 Spectral analysis of INTEGRAL data

We performed fits to the combined JEM-X, ISGRI, and SPI spectra for each of the four epochs (see Table 4.1) using XSPEC Arnaud 1996 version 11.3. All errors quoted in this work are 90% confidence errors, obtained by allowing all variable parameters to float during the error scan. In all fits, we fixed the value of the column density to $N_H = 8.0{\times}10^{21}$ atoms/$cm^2$, as obtained by Díaz Trigo et al. (2007) using XMM-Newton data for GRO J1655–40 during the same outburst.

Our main aim in these fits is to characterize the broad continuum as seen with INTEGRAL and its wide energy coverage. To account for uncertainties in relative instrument calibrations, we fixed the JEM-X multiplicative calibration constant to 1 and let those for ISGRI and SPI free to vary in the fit for the different data sets, as shown in Table 4.2.

In Figures 4.7, 4.8, 4.9, 4.10 and 4.11 below, we show spectra from each epoch because these provide a convenient way to see the evolution of the source during our observations. We fitted the spectra with several models, and the derived parameters are presented in Table 4.2. We modeled the spectra with simple and phenomenological disk plus power-law models and common Comptonization models described in Section 4.2. We find that the former are very successful (see Section 4.5.1.1) and that there is no evidence of any spectral break in the data up to ≈600 keV (see Section 4.5.1.2). Although a simple power law provides marginally acceptable fits for the first two epochs, it was necessary to include an iron line and edge components in the fits for the last two epochs (Section 4.5.2).

### 4.5.1 Fits to Epochs 1 and 2

#### 4.5.1.1 Fits with a Pure Power Law

We initially performed fits with a phenomenological power-law model (powerlaw in XSPEC). In the first epoch, the source spectra cover energy ranges of 5-20 keV for JEM-X and 23-600 keV for both ISGRI and SPI. In fitting the power-law model, we obtained a reduced $\chi^2$ of $\chi^2_\nu = 1.26$ with $\nu = 63$ ($\nu$ being the number of degrees of freedom in the fit). The presence of a multicolor disk component was not significantly required in our fit. The value obtained for the photon index is $\Gamma = 1.72{\pm}0.03$, common for black holes in a hard spectral state.

For the second epoch of observations, the source spectra extend over the energy ranges of 5-30, 23-500, and 23-400 keV for JEM-X, ISGRI, and SPI, respectively. This time, the presence of emission from a disk was significant, and we added an absorbed multicolor disk component (Mitsuda et al., 1984) to the power law [phabs(diskbb+powerlaw) in XSPEC]. We obtained $\chi^2_\nu = 1.38$ with $\nu = 88$. The value obtained for the inner disk

**Table 4.2**: Parameters Obtained for the Best Fits of the Joint JEM-X, ISGRI, and SPI Spectra.

| Parameter | Epoch 1 | Epoch 2 | Epoch 3 | Epoch 4 |
|---|---|---|---|---|
| | | Powerlaw | | |
| $\Gamma$ | – | – | – | 4.7±0.6 |
| $N_{pow}$ [ph/keV/s/cm$^2$] at 1 keV | – | – | – | 580±60 |
| | | eqpair | | |
| $\Gamma_p$ | 0.6±0.3 | ≈0 | – | – |
| $\Gamma_{min}$ | 1.3 (f) | 1.3 (f) | – | – |
| $\Gamma_{max}$ | 1000 (f) | 1000 (f) | – | – |
| $l_s$ | 10 (f) | 10 (f) | – | – |
| $l_h/l_s$ | 0.8±0.3 | 1.2±0.6 | – | – |
| $l_{nth}/l_{th}$ | 0.8±0.1 | 0.2±0.3 | – | – |
| $\tau$ | 1±0.5 | 4±1 | – | – |
| Refl [$\Omega/2\pi$] | 0(f) | 0 (f) | – | – |
| $kT_{in}$ (keV) | 0.5(f) | 1.25±0.02 | – | – |
| $R_{in}$ (keV) [GM/c$^2$] | 6 (f) | 6 (f) | – | – |
| $R_{out}$ (keV) [GM/$c^2$] | 100 (f) | 100 (f) | – | – |
| | | diskbb | | |
| $kT_{in}$ [keV] | – | 1.25±0.02 | 1.28±0.02 | 1.27±0.17 |
| $N_{bb}$ [($R_{in}$[km]/D[10kpc])$^2$×cos$\theta$] | – | $1321^{+72}_{-67}$ | 710±40 | 500±60 |
| | | gaussian | | |
| $E_{gauss}$ [keV] | – | – | 6.7±0.3 | 6.7±0.9 |
| $\sigma$ [keV] | – | – | 0.63±0.15 | 0.8±0.5 |
| $N_{gauss}$ [ph/cm$^2$/s] | – | – | 0.017±0.008 | 0.05±0.03 |
| | | edge (Fe XXV) | | |
| $E_{edge}$ [keV] | – | – | 8.64±0.20 | 8.6±0.9 |
| $\tau$ | – | – | 0.20±0.05 | 0.20±0.10 |
| | | edge (Fe XXVI) | | |
| $E_{edge}$ [keV] | – | – | 9.278 (f) | 9.278 (f) |
| $\tau$ | – | – | ≤0.02 (f) | ≤0.02 (f) |
| | | pexriv | | |
| Photon index | – | – | 2.50±0.23 | – |
| $E_f$ [keV] | – | – | 1000.0 (f) | – |
| R [$\Omega/2\pi$] | – | – | ≤0.30 | – |
| Fe abundance | – | – | 2.8 (f) | – |
| cos(i) | – | – | 0.45 (f) | – |
| $T_{disk}$ [K] | – | – | 1.2E+07 (f) | – |
| xi [$4\pi F_{irr}/n$] | – | – | 5000 (f) | – |
| $N_{pexriv}$ [ph/keV/cm$^2$/s] | – | – | 3.8±1.5 | – |

**Table 4.2**: (Continued.)

| Parameter | Epoch 1 | Epoch 2 | Epoch 3 | Epoch 4 |
|---|---|---|---|---|
| | | Instrumental normalization factors | | |
| $C_{JEM-X}$ | 1.0 (f) | 1.0 (f) | 1.0 (f) | 1.0 (f) |
| $C_{ISGRI}$ | 1.1±0.1 | 1.0±0.1 | $0.46^{+0.11}_{-0.15}$ | 0.39±0.14 |
| $C_{SPI}$ | 1.4±0.1 | 1.1±0.1 | – | – |
| $\chi^2_\nu$ | 1.21 | 1.44 | 2.62 | 2.73 |
| $\nu$ | 57 | 83 | 19 | 22 |

Notes to Table 4.2
[1]Parameters fixed in the fits are denoted by 'f'.
[2]We fixed the value of the column density to $N_H = 8.0\times10^{21}$ atoms/$cm^2$
as obtained by Díaz Trigo et al. (2007) using XMM-Newton data of GRO J1655−40 during the same outburst.
[3]The models used are `constant×eqpair` in epoch 1, `constant×phabs(diskbb+eqpair)` in epoch 2,
`constant×phabs(diskbb + gaussian + pexriv)edge×edge` in epoch 3 and
`constant×phabs(diskbb + gaussian + powerlaw)edge×edge` in epoch 4 (see text for details).

temperature is $kT_{in} = 1.25\pm0.01$ keV. The spectrum is softer, with a photon index of $\Gamma = 2.21\pm0.04$.

For the last two epochs, in fitting with the phenomenological power law (plus a multicolor disk blackbody component), the spectra showed large negative residuals at ≈10 keV, compatible with the presence of Fe edges. The presence of positive residuals in the 6-8 keV range is consistent with the presence of a broad Fe emission line. In Section 4.5.2, we go into more detail about the fits for both these epochs.

#### 4.5.1.2 Fits with Thermal Comptonization Models

As explained in Section 4.2, all models involving thermal Comptonization processes as the origin of the high-energy emission seen in black hole transient systems predict an energy turnover at the electron temperature of the corona. So, in order to assess the role of Comptonization during our observations, we fitted with the thermal Comptonization model of Titarchuk (1994) (compTT in XSPEC), which deals with the special case of high temperatures, small opacities, or both (so that relativistic effects are taken into account). We also performed fits using the BMC model of Ebisawa et al. (1996) (see also Titarchuk & Shrader 2002 for a comoving Comptonizing medium), which deals with the Comptonization due to bulk motion of the almost free-falling (convergent accretion) flow close to the black hole. Moreover, we fitted with a phenomenological and multiplicative model with a high-energy cutoff (highecut in XSPEC) in order to find any turnover energy in our data that could be in agreement with Comptonization's playing the major role in the high-energy emission from GRO J1655–40.

We thus fitted the spectra from the first two epochs [2] with the following models: `phabs(diskbb+powerlaw)highecut` (hereafter model 1), `phabs(diskbb+compTT)` (model 2), and `phabs(bmc)highecut` (model 3). In the case of the first epoch, the presence of a multicolor disk component was not significantly required. We assumed a spherical geometry for the Comptonizing medium for model 2 in all our fits.

For epoch 1, we obtained the following statistics for the three models: $\chi^2_\nu = 1.13, 1.17, 1.13$ ($\nu = 61, 60, 59$), respectively. We find that when fitting the data with a cutoff power law (model 1), while showing slightly better statistics, the high-energy cutoff cannot be well constrained (values between 5 and 54 keV are compatible with the data). The obtained folding energy is over 253 keV. We made separate JEM-X + ISGRI and JEM-X + SPI fits to see if a break is possible in one of the two data sets. For the former, we obtained unconstrained values for the cutoff and folding energies, in the range of 5-38 keV and over 238 keV, respectively. In the second data set there was not any break in the data either. We conclude that the cutoff features found are of instrumental origin and not physically meaningful. Thus, there is not any real cutoff in our data. This conclusion is also supported by the fact that the parameters of optical depth and electron temperature ($\tau$ and $kT_e$) when fitting with model 2 are unconstrained as well. This model clearly is not a good description of the high-energy spectrum ($\gtrsim$20 keV). Model 3, while yielding the lowest residuals, does not allow us to constrain the values of the parameters (neither `bmc` nor `highecut` component). Thus, this model does not represent a physical description of the data. The fact that model 3 provides slightly better statistics than the power-law model described in Section 4.5.1.1 is due to the fact that it is a convolution of both soft and hard emission components, taking into account the physical conditions in the inner region of the accretion disk.

We derive from fitting all these models that the high energies cannot be reproduced solely with photons that are thermally upscattered by a Comptonizing corona. In order to take this into account, we fitted the spectrum of epoch 1 with the hybrid Comptonization model EQPAIR (Coppi , 1999), which is appropriate for very hot plasmas. This model describes the physics and emission properties of hybrid plasmas, where the particle energy distribution is approximately a Maxwellian plus a power law. The model treats a hot plasma cloud, mainly modeled as a spherical corona around the compact object, illuminated by soft thermal (Maxwellian) and nonthermal (either power-law or monoenergetically distributed) electrons that lose energy by Compton, Coulomb, and bremsstrahlung interactions. This model was shown to be successful in accounting for the high-energy spectra of Cygnus X-1 and other black hole candidates in different spectral

[2] As we explained in Section 4.5.1.1 the presence of significant residuals compatible with broad Fe emission line, edges and likely reflection could distort our undertanding of the continuum. Thus, we do not use last two epochs in our study of the continuum models. Moreover, the spectra in these epochs do not show significant emission at high ($\gtrsim$150 keV) energies.

states and over a broad energy band, ranging from soft X-rays to gamma rays (see, e.g., McConnell et al. 2000, 2002; Cadolle et al. 2006; Malzac et al 2006).

For epoch 2 of our observations, we obtained the following statistics for the three models: $\chi^2_\nu = 1.47, 1.45, 2.07$ ($\nu = 86, 87, 86$), respectively. Again, model 1 does not show a break or cutoff below 500 keV (i.e., the values of both cutoff and folding energies cannot be constrained), and model 3 is not a proper fit to the data, because of the bad statistics. In this epoch, the values obtained for the optical depth of the Comptonizing medium and the temperature of the electrons ($\tau$ and $kT_e$) cannot be constrained. Thus, the data show that thermal Comptonization is not the main process generating the emission at high energies ($\gtrsim$20 keV). As in epoch 1, we tested the model of Coppi (1999) optimized for very hot coronae (see description in the previous paragraph), this time coupled with a `diskbb` component to describe the soft emission from the accretion disk.

#### 4.5.1.3 Fits with the EQPAIR Nonthermal Comptonization Model

The EQPAIR model takes into account angle dependence, Compton scattering (up to multiple orders), photon pair production, pair annihilation, and bremsstrahlung, as well as reflection from a cold disk. As noted by Coppi (1999), if a spectrum extends up to 500 keV, high-energy emission from a nonthermal population of electrons is clearly present.

As can be seen in Figures 4.5 and 4.6, showing fits of both epochs 1 and 2 with a single power law (see description in Section 4.5.1.1), a small deficit of counts in the ISGRI spectra (red) above 200 keV with respect to SPI (green) is clearly present. Moreover, the large bins of the ISGRI spectra in this range indicate that the source was not detected above 200 keV. This could be a consequence of the fact that SPI is optimized for spectroscopy up to 1 MeV, while ISGRI has poorer sensitivity above 200 keV. Taking these considerations into account, we limit our analysis of the ISGRI data to the energy range 23-200 keV.

The EQPAIR model allows one to inject a nonthermal electron distribution with Lorentz factors between $\Gamma_{min}$ and $\Gamma_{max}$ and a power-law spectral index $\Gamma_p$. The cloud is illuminated by soft thermal photons emitted by an accretion disk. These photons serve as seeds for Compton scattering by both thermal and nonthermal electrons. The system is characterized by the power (i.e., luminosity) $L_i$ supplied by its different components. We express each of them dimensionlessly as a compactness parameter, $\mathrm{l}_i = \mathrm{L}_i\sigma_\mathrm{T}/(\mathrm{Rm}_e\mathrm{c}^3)$, where R is the characteristic dimension and $\sigma_\mathrm{T}$ is the Thomson cross section of the plasma. Thus, $\mathrm{l}_s$, $\mathrm{l}_{th}$, $\mathrm{l}_{nth}$ and $\mathrm{l}_h = \mathrm{l}_{th} + \mathrm{l}_{nth}$ correspond to the power from the soft disk entering the plasma, thermal electron heating, electron acceleration, and the total power supplied to the plasma. The total number of electrons (not including $\mathrm{e}^+\mathrm{e}^-$ pairs) is determined by $\tau$, the corresponding Thomson optical depth, measured from the center to the surface

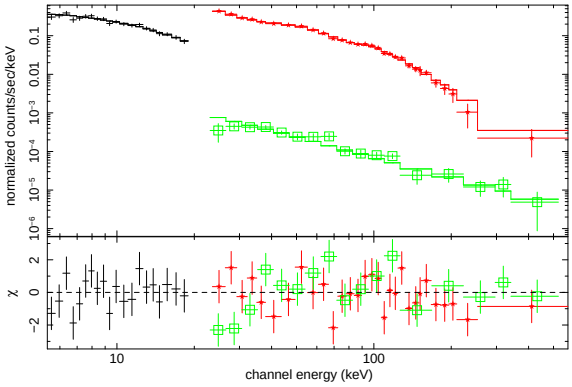


**Figure 4.5**: Fitted INTEGRAL spectra, corresponding to epoch 1 (hard state) with a simple phenomenological power-law model (see Sections 4.5.1.1 and 4.5.1.3 for detailed information about this fit.) JEM-X (black), ISGRI (red), and SPI spectra (green) are shown.

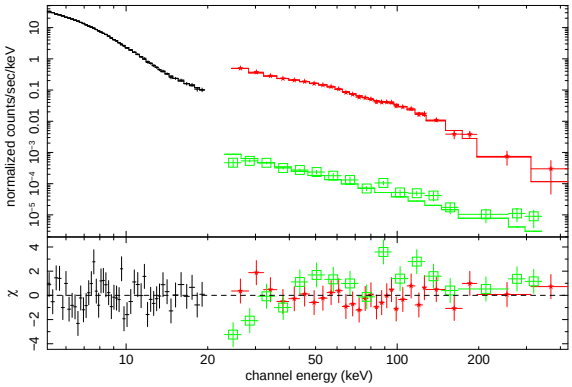


**Figure 4.6**: Same as Figure 4.5, but for epoch 2 (thermal-dominant state).

of the scattering region. We considered the source to be moderately compact and fixed $l_s = 10$, as broadly reported for other sources with similar characteristics.

The disk spectrum incident on the plasma is modeled with a multicolor disk blackbody as given by the `diskbb` model in XSPEC (Mitsuda et al., 1984). The temperature of the inner edge of the accretion disk was fixed to $kT_{in} = 0.5\,keV$. The limits of the accretion disk were fixed at $R_{max} = 100R_g$ and $R_{min} = 6R_g$. We attempted to fit the spectra of both epochs 1 and 2, fixing the reflection covering factor to zero.

For epoch 1 of our observations, we first performed a fit with nonthermal electrons injected with a power-law distribution of Lorentz factors from $\Gamma_{min} = 1.3$ to $\Gamma_{max} = 1000$. The upper and lower limits $\Gamma_{min}$ and $\Gamma_{max}$ were kept fixed while fitting the power-law index $\Gamma_p$. This resulted in an acceptable fit, with $\chi_\nu = 1.21$ ($\nu = 57$). The unfolded

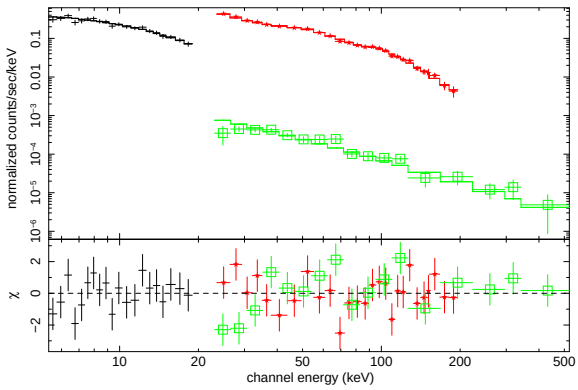


**Figure 4.7**: Same as Figure 4.5, but fitted with the EQPAIR Comptonization model of Coppi (1999) `eqpair` in XSPEC). Details about the fitting and the parameters obtained are in Section 4.5.1.3 and Table 4.2.

broadband spectrum and residuals are shown in Figure 4.7. The best-fit parameters are presented in Table 4.2; $l_h/l_s$ is about unity, that is, intermediate between what is found in the hard state (4-10) and the thermal-dominant state ($\leq$0.4) (Ibragimov et al., 2005). The heating of the plasma is dominated by the nonthermal acceleration ($l_{nth}/l_{th}\approx$1). We also fitted the spectra of this epoch considering a monoenergetically distributed population of nonthermal injected electrons instead. The reduced $\chi^2$ thus obtained is slightly better ($\chi_\nu = 1.19$, $\nu = 57$). The values obtained for $l_h/l_s$ and $l_{nth}/l_{th}$ remained unchanged, except for an increase in the Thomson scattering depth (from 1.0$\pm$0.6 to 2.7$\pm$0.4) The increase in the optical depth lends support to the scenario of Comptonization through injected nonthermal electrons being the dominant mechanism, in the sense that if this is done by electrons with a monoenergetic distribution, then having a denser cloud would produce the same effect as taking into account a broader distribution (both in energy and spatially). Thus, we conclude that in order to reproduce the spectrum of epoch 1, we have to consider an almost pure distribution of nonthermal accelerating particles.

As in epoch 1, we tested the model of Coppi (1999) optimized for very hot coronae in the observations of epoch 2, this time coupled with a `diskbb` component to describe the soft emission from the accretion disk. We performed a fit with nonthermal electrons injected with a power-law distribution of Lorentz factors from $\Gamma_{min} = 1.3$ to $\Gamma_{max} = 1000$. The upper and lower limits $\Gamma_{min}$ and $\Gamma_{max}$ were kept fixed while fitting the power-law index $\Gamma_p$. This resulted in an acceptable fit, with $\chi_\nu = 1.44$ ($\nu = 83$). The unfolded broadband spectrum and residuals are shown in Figure 4.8. The best-fit parameters are presented in Table 4.2; $l_h/l_s$ is again about unity. However, the heating of the plasma by nonthermal particles is practically nil ($l_{nth}/l_{th}\approx$0). The situation does not improve if one considers a monoenergetic distribution of the nonthermal accelerated electrons. This is

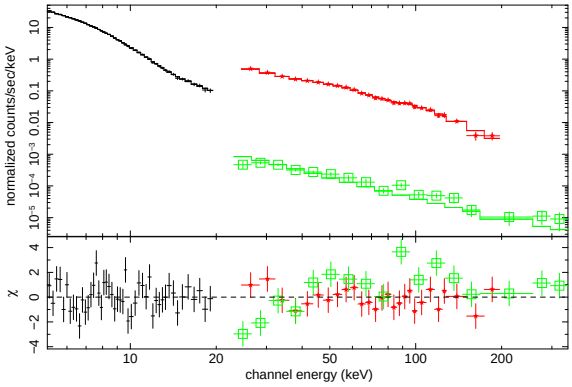


**Figure 4.8**: Same as Figure 4.7, but for epoch 2, considering also the soft emission from an accretion disk (`diskbb` in XSPEC).

not surprising, since as claimed by Coppi (1999), a very good spectrum extending above 200 keV is mandatory in order to disentangle a likely population of nonthermal particles in the source. In the case of our observations, the large bin at ≈200 keV shows that the source was not detected above this energy. We conclude that while in epoch 2 of our observations a break is not observable in the high- energy data ($\gtrsim$20 keV), the energy coverage is not great enough to test for the presence of nonthermal processes. This is due to the fact that in this period the spectrum became very soft, as compared with epoch 1, with radiation detected to ≈200 keV as much.

### 4.5.2 Fits to Epochs 3 and 4

#### 4.5.2.1 Fits with Iron Emission Line and Absorption Edges

As can be seen from the shape of the residuals (Figure 4.9), fits with the simple multicolor disk model of Mitsuda et al. (1984) and a power law do not yield formally acceptable fits to the last two epochs. The presence of large residuals at 6-8 keV and around 10 keV require us to take into account an iron emission line, iron absorption edges, and likely disk reflection components. These features are theoretically required in very ionized mediums such as the close vicinity of a black hole (see Ueda et al. 1998 for a prior detection of Fe absorption lines and edges in GRO J1655–40 in the context of observations of the 1996 outburst, and George & Fabian (1991) and Laor (1991) for a description of the Fe line profile produced in accretion disks around black holes). The reflection component takes into account the physics due to the continuum produced by a source of hard X- rays Compton-reflected by an accretion disk (Gilfanov et al., 2000).

We fitted our spectra with the following XSPEC model:
`phabs(diskbb+powerlaw+gaussian)edge*edge`. The results and the folded and unfolded

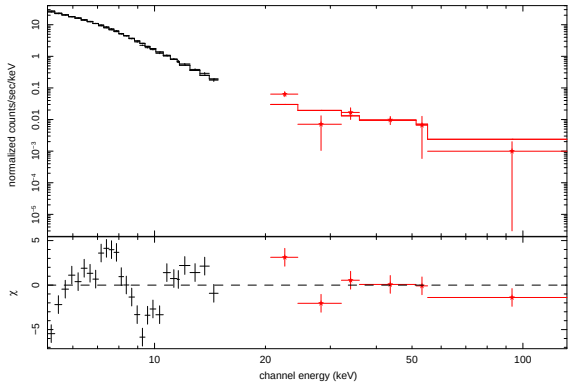


**Figure 4.9**: Fitted INTEGRAL spectra, corresponding to epoch 4 (thermal dominant state). The model used consists of a pure power law plus emission from an absorbed multicolor accretion disk (Mitsuda et al., 1984). In this period we note a change in the properties of the accretion outflow with respect to epochs 1 and 2 (see Section 4.5.1.1 and 4.6 for details).

spectra are shown in Table 4.2 and in Figures 4.10 and 4.11, respectively. Regarding the Gaussian Fe emission line component, we constrained the line center to lie at 6.4-6.97 keV, which is the allowed range by the different ionization states of Fe. Also, we constrained the width ($\sigma$) of the emission line to be 1 keV as a fiducial maximum value in order to obtain convergence of our fits. Regarding the two iron absorption edges, one was fixed at 9.278 keV, which corresponds to Fe $XXVI$ and is expected to appear, given the likely range of temperatures and ionization.

Fitting this model to the spectra for epochs 3 and 4 we obtained better results than fitting with a power-law model (plus an absorbed multicolor disk), that is, $\chi^2_\nu = 9.99$, with $\nu = 21$ and $\chi^2_\nu = 2.73$, with $\nu = 22$ for the third and fourth epochs, respectively. Although the fit was unacceptable for epoch 3, because of large residuals around $\approx$10$-$20 keV, which could be due to reflection [3], the fit was reasonable for epoch 4. The multicolor disk component gave an inner disk temperature of $kT_{in} = 1.27\pm0.17$ keV for the fourth epoch, for which we also obtained a very soft photon index ($\Gamma = 4.7\pm0.6$).

We substituted the `pexriv` reflection model for the power-law component for the third epoch. This is a power law with an exponential cutoff to take into account reflection effects in the spectrum. In fitting with `pexriv`, we imposed an overabundance of Fe of 2.8 with respect to the solar value and $\cos i = 0.45$, the latter implying an inclination of 63° for the reflection medium, namely, the disk (as found by Díaz Trigo et al. 2007 based on XMM- Newton and INTEGRAL data for the same period of observation). The

[3] It is important to notice that Díaz Trigo et al. (2007) did not find reflection signatures in the analysis of joint XMM and INTEGRAL data corresponding to our fourth epoch. The disagreement could be due to the $20-30$ keV removed bin in their study, made in order to improve the statistics for the joint spectrum obtained in this period.

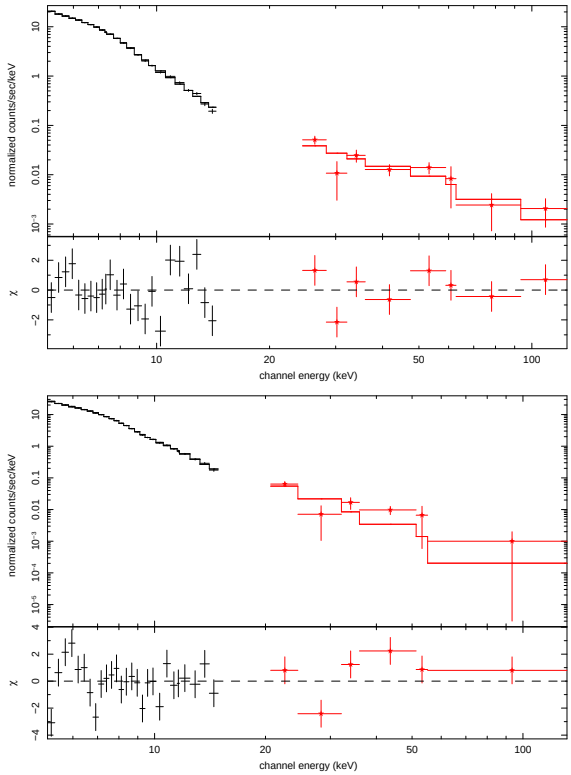


**Figure 4.10**: Fitted INTEGRAL spectra, corresponding to epochs from 3 (top) and epoch 4 (bottom). These spectra were fitted with an absorbed multicolor disk (Mitsuda et al., 1984) plus a simple power-law, iron emission line and edges for both epochs (and reflection in the case of epoch 3). Details about the fitting and the values of the parameters obtained are in Section 4.5.2 and Table 4.2. JEM-X (black) and ISGRI (red) are shown.

disk temperature that produced the smallest residuals was $T_{disk} = 1.2{\times}10^{+07}$ K, so we fixed this value in our fits. This value is consistent with having very ionized material in the accretion disk. Also, in order to properly fit the high-energy part of the spectrum ($\gtrsim$20 keV), it was necessary to fix the `pexriv` e-folding energy to a very high value, namely, 1000 keV, implying a nondetection of any cutoff up to $\approx$200 keV.

As a result of this fit for epoch 3, we obtained a reflection covering factor of $R{\leq}0.3$. Actually, this quantity (R) approximately measures the solid angle subtended by the reflecting medium as seen from the source of the primary radiation, R$\approx\Omega_{refl}/2\pi$, so that R = 1 for an isotropic point source above an infinite, optically thick slab. We fixed the ionization parameter to a very high value, consistent with a very highly ionized medium, $x_i = 4\pi F_{ion}/n$=5000 erg×cm/s (where $F_{\rm ion}$ is the 5-20 keV irradiating flux and n is the density of the reflector; see Done & Nayakshin 2001).

In order to estimate the source luminosity in each of our observations, we used a power law plus an absorbed multicolor disk to model all the epochs. The contribution of

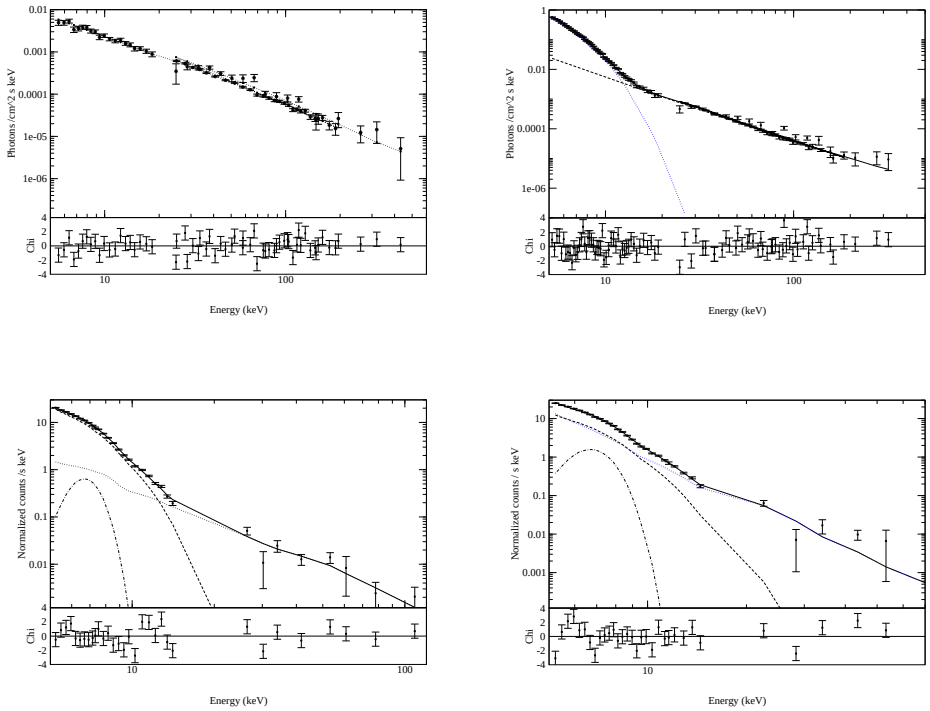


**Figure 4.11**: Unfolded spectra from epochs 1–4 (top left to bottom right). The solid line shows the total model (see the text and Table 4.2 for details), the dash-dotted line the iron K$\alpha$ emission line, the long-dashed line the accretion disk component and the short-dashed line the power law (`pexriv` in the third epoch).

the iron emission and absorption effects together only account for less than 10% of our data in the last two epochs. The unabsorbed flux in the 5-100 keV energy range, $\mathrm{F_X}(5-100)$, is $1.4{\times}10^{-9}, 1.2{\times}10^{-8}, 1.0{\times}10^{-8}, 1.0{\times}10^{-8}$ erg cm$^{-2}$ s$^{-1}$ for epochs 1-4, respectively. For a distance of 3.2 kpc (Tingay et al., 1995), these fluxes give luminosities in the 5-100 keV energy range, $\mathrm{L_X}(5-100)$, of $1.7{\times}10^{36}, 1.5{\times}10^{37}, 1.2{\times}10^{37}, 1.2{\times}10^{37}$ erg/s. The unabsorbed fluxes in the 5-600 keV energy range are $\mathrm{F_X}(5-500) = 3.7{\times}10^{-9}, 1.2{\times}10^{-8}$, $1.0{\times}10^{-8}, 1.0{\times}10^{-8}$ erg s$^{-1}$ cm$^{-2}$, giving luminosities of $\mathrm{L_X}(5{-}600)_X = 4.6{\times}10^{36}, 1.5{\times}10^{37}$, $1.2{\times}10^{37}, 1.2{\times}10^{37}$ erg/s for epochs 1-4, respectively. Even if we take the broader energy range as more indicative of the true source luminosity, these values represent only 0.5%, 1.5%, 1.3%, and 1.3% of the Eddington limit ($L_{\mathrm{EDD}} = 9.4{\times}10^{38}$ erg/s for a black hole of $7\,M_\odot$), respectively.

## 4.6 Discussion

We have performed fits to four epochs of INTEGRAL broadband spectra of the stellar-mass black hole GRO J1655–40 during its 2005 outburst. We find that GRO J1655–40 was in the hard state in the first epoch, based on a low photon index (i.e., 1.72±0.03) and the absence of a strong thermal disk component. The source evolved to a state that resembles the thermal- dominant state, in the classification scheme of Remillard & McClintock (2006). These results are in agreement with the previous study of this outburst by Brocksopp et al. (2006). However, Saito et al. (2007), on the basis of their analysis of RXTE PCA data for this source, showed that the luminosity of the accretion disk deviates from the $L \propto T^4$ relation typical of thermal-dominant states during our other three observations (epochs 2, 3, and 4). So, the state observed may not be a true thermal-dominant state, or nonthermal effects may need to be modeled to describe the accretion disk's emission (Kubota et al., 2001).

For the two later epochs, we found that our data are best fitted by adding an iron emission line and edges to the model, consisting of an absorbed multicolor disk (Mitsuda et al., 1984) plus a power-law component. Although the obtained fits were not formally acceptable ($\chi^2_{red}$ of 9.99 and 2.73 for epochs 3 and 4, respectively), the fit in the fourth epoch was improved by $\Delta\chi^2_{red} = 4.8$. Also, the shape of the residuals using the model consisting of a multicolor disk blackbody plus a power law shows a clear excess in the 6-8 keV range and a drop around 10 keV, features that can only be explained by the presence of an iron emission line and Fe edges. The spectrum in the third epoch shows an excess of absorption in the 10-20 keV energy range with respect to that expected taking into account the edges obtained in Díaz Trigo et al. (2007) based on XMM-Newton and INTEGRAL spectra (see Section 4.5.2). This excess could be explained by the presence of reflection, but the situation is still unclear. We attempted to deal with this feature in epoch 3 by fitting with a broken power law model (`pexriv` in XSPEC), but there is no clear evidence for a break in this spectrum. We conclude that for GRO J1655–40, it is difficult to study reflection features. This may be due to the high inclination of the source, which could alter the shape of such features through scattering. The presence of these features in the spectra of epochs 3 and 4 may reveal differences in the disk outflow properties with respect to any outflow in epochs 1 and 2. In fact, our spectrum obtained in epoch 3 precedes a Chandra observation revealing a line-rich spectrum (Miller et al, 2006) by only 3 days.

Assuming a value of 63° for the inclination (Díaz Trigo et al., 2007) and a distance of 3.2 kpc (Tingay et al., 1995), the disk normalization factor (in fits made only with a power-law model plus a multicolor absorbed disk) gives an inner disk radius [4] of

[4] This radii are measured from infinity, using the formula:
$R_{in} = D \times (diskbb_{norm}/cos(i))^{0.5}$
where $R_{in}$ is in km and D is in units of 10 kpc. This formula is inferred without taking into account

16.5±0.2 km for the second epoch (the first epoch was in a hard state and had no significant contribution from the disk, as shown in Section 4.5.1.1). Since $R_g = 10.4$ km is the value of the gravitational radius for a $7\,M_\odot$ black hole, we find that the matter arrives at an inner radius of $\approx 1.6 R_g$ in the second epoch. This value is consistent with the value predicted for a maximally rotating black hole, as explained in Section 4.2 ($R_{ISCO} = 1.25\ R_g$), and is similar to that obtained by Tomsick et al. (1999). By analyzing RXTE data, Tomsick et al. (1999) found inner radius values $R_{in}$ of $10.9^{+2.6}_{-2.6} - 21.9^{+5.2}_{-5.2}$ km, depending on the value adopted for the disk inclination. Of course, values of the inner disk radius inferred from continuum fits are suspect and must be viewed with caution. A number of effects (Merloni et al., 2000) can serve to distort the observed inner disk parameters (see Saito et al. 2007 for a determination of more realistic values for the radii, since these are not affected by a strong power-law component). According to Merloni et al. (2000), the main effect seems to be that the opacity is dominated by electron scattering rather than free-free absorption. The net result is that the derived temperature given by the parameter $\mathrm{kT_{in}}$ overestimates the effective inner temperature by a factor of 1.7 or more (Shimura & Takahara, 1995).

The most interesting issue regarding our INTEGRAL observations of GRO J1655–40 is undoubtedly the presence of very significant and unbroken high- energy emission up to 500 keV in the hard state of GRO J1655–40, as noticed from the first epoch. Grove et al. (1998) made a comparative measurement of a number of systems with data from the OSSE instrument on CGRO and found that many of these systems showed a cutoff at high energies around ∼100 keV in the hard state. [5] Since then, several studies have tried to measure cutoffs in the spectra, which could manifest the validity of Comptonization by thermal electrons playing the major role in the high-energy emission of black holes in the hard state. In our work we did not find such a break, and the presence of a nonthermal population of relativistic electrons was inferred from the fitting of our spectrum in the hard state.

Our finding is that nonthermal processes are the most important in explaining the high-energy emission of the hard state of GRO J1655–40. In addition, there is not any break in the data indicating that the high- energy emission is mainly produced by thermal Comptonization, as previously claimed. Moreover, nonthermal Comptonization is the main source of the high- energy emission in the second epoch (thermal-dominant state). This condition for the thermal-dominant state has been broadly reported in the literature since Grove et al. (1998).

gravitational effects from the General Relativity Theory. If gravitational corrections would be taken into account, then smaller co-moving radius would be obtained.

[5] CGRO/OSSE integration times were very long (of order of weeks), so different states would be mixed. This is not an issue for INTEGRAL, since exposures for each obtained spectrum are around two days and it is not hoped to have noticeable high energy evolution with this timing, as infrerred from the light curves.

**Table 4.3**: Values for the components of Comptonization models in previous studies.

| Source | Γ | State | $E_{cut-off}$(keV) | $E_{max}$(keV) | $T_e$ (keV) | $\tau$ | Reference |
|---|---|---|---|---|---|---|---|
| IGR J17497–2821 | 1.67±0.06 | LH | 195±50 | ≈200 | $35^{+200}_{-9}$ | $1.45^{+0.5}_{-1.4}$ | 1 |
| GX 339–4 | 1.4 − 1.6 | LH | 50 − 200 | ≈200 | – | – | 2 |
| | 1.92±0.05 | IS | 72±8 | ≈200 | – | – | 3 |
| XTE J1550–564 | 1.70±0.01 | LH | 115±5.6 | | – | – | 4 |
| | 1.53±01 | LH | 460±300 | | – | – | 4 |
| Cyg X–1 | 1.9±0.1 | LH | ≈150 | ≈600 | $67^{+8}_{-6}$ | 1.98±0.22 | 5 |
| | 2.1 | IS | ≈100 | ≈1000 | 20 − 65 | 0.55 − 1.36 | 6 |
| | 1.65 − 2.0 | LH | 130 − 250 | ≈150 | – | − 1 | 7 |
| GRO J1655–40 | 1.35±0.03 | LH | 100 − 200 | ≈600 | | | 8 |
| | 1.72±0.03 | LH | – | ≈500 | – | | 9 |

Notes to Table 4.3

[1]Values are listed for several sources in several states close to the hard state. Also values for the high-energy cutoffs and/or break energies (if present) are reported.

[2](LH) Hard state; (IS) intermediate state.

[3]REFERENCES: (1) Walter et al. (2007); (2) Miyakawa et al. (2007); (3) Belloni et al. (2006); (4) Yuan et al. (2007); (5) Cadolle et al. (2006); (6) Malzac et al (2006); (7) Wilms et al. (2006); (8) Shaposhnikov et al. (2006); (9) this work.

In Table 4.3, we summarize the references showing breaks in the high- energy emission of several black hole candidates in the hard and intermediate states. One contemporaneous study by Shaposhnikov et al. (2006) of the hard state of GRO J1655–40 used INTEGRAL observations covering a period of time slightly prior to that of our first epoch. They pointed to the presence of a cutoff around 200 keV in their ISGRI and SPI spectra as a manifestation of thermal Comptonization's being the main source of the high-energy emission. However, their sensitivity at energies $\gtrsim$200 keV is not high enough to disentangle the emission of a nonthermal population of electrons. As also noted by Coppi (1999), if a spectrum extends up to 500 keV, high-energy emission from a nonthermal population of electrons is clearly present. The finding of such a contribution in the high-energy emission has been reported before for the Cyg X-1 system (Malzac et al 2006; Cadolle et al. 2006 [both in the intermediate state]), and it may be present in GRS 1915+105 (Zdziarski et al. 2001; Rodriguez et al. 2004 [both in the thermal-dominant state]). With our study, we extend the list of sources showing high-energy emission from nonthermal electrons with GRO J1655–40, this time in the hard state. Joinet et al. (2006) also reported the detection of a nonthermal population of electrons in the hard state of GX 339-4. However, they also indicated the presence of a cutoff in the spectrum.

From Table 4.3, it can be seen that while some cutoffs appear to be close to the upper boundaries of the high-energy instruments used, others appear to be physically meaningful. The latter correspond to the systems GX 339-4 and Cyg X-1, both having known low inclination angles of i≈45° and i≈35°, respectively. GRO J1655–40 is a very high inclination system, with an inner disk that could have an inclination of i = 85° (see

Section 4.2). Comptonization of soft photons through thermal and/or nonthermal electrons seems to be highly isotropic to an observer external to the system if the electrons do not acquire outflow velocities $v/c \gtrsim 0.2$ (Beloborodov et al., 1999), so in principle this should not depend on the inclination angle of the system. But other processes, such as reflection, could depend on the viewing angle, being almost unobserved for high- inclination systems such as GRO J1655–40 (as pointed out above with our fitting of epoch 3). So, GRO J1655–40 in the hard state would be an excellent source for the study of Comptonization processes, without any apparent disturbance from other high-energy mechanisms (including soft emission from a disk). If these hypotheses are correct, we would have discovered that Comptonization of black hole transients in the hard state occurs mainly through nonthermal relativistic electrons. This conclusion is also supported by the study of Malzac et al (2006) of Cyg X-1 in the intermediate state, because, while they found a high-energy cutoff around 100 keV, they also point to the presence of high-energy emission from a nonthermal population of electrons in a state close to the hard state (in the case of Joinet et al. (2006), in the hard state of GX 339-4).

## 4.7 Conclusions

GRO J1655−40 is a black hole transient discovered on July 1994 with the CGRO satellite (Zhang et al., 1994). It is a LMXB with a black hole of mass $m_{BH} = 7.02 \pm 0.22 M_{\odot}$ (Orosz & Bailyn, 1997). The inclination of the system is $\approx 70^{\circ}$ (van der Hooft et al., 1998) although the inclination of the inner disk could be as high as 85°.

This system may harbor a maximal spinning black hole (a≥0.9), indicating an inner radius of $r \leq 1.4\,R_g$ (Miller et al., 2005). Strong QPOs are detected (300-450 Hz) (Strohmayer , 2001) and extremely relativistic radio jets have been detected in radio (Hjellming & Rupen, 1995).

Tomsick et al. (1999) did the first detection of unbroken powerlaw emission up to 800 keV during the low/hard state. We did INTEGRAL observations during the 2005 outburst detecting the source up to 500 keV during the low/hard state. In this work, the low/hard state spectrum was modeled using both simple models like a power-law, and using EQPAIR. The lack of a break in fits with the simple power-law implies that non-thermal Comptonization may dominate the hard X-ray spectrum. Additional modeling with EQPAIR confirms that non-thermal Comptonization is best able to explain the observed spectrum. This work suggested thermal Comptonization processes not being the main source for the high energy emission of GRO J1655−40. However, more work is needed to unveil the source of the high energy emission, and INTEGRAL observations are planned for a broad sample of black hole transients.

# Chapter 5

# The High-Energy Emission from GX 339–4

## 5.1 Introduction

GX 339–4 (also called V821 Ara) is a black hole X-ray binary of recurrent type (i.e. this source undergoes frequent outbursts followed by very faint states) with few episodes in quiescence (Kong et al., 2000). Hynes et al. (2003) determined, on the basis of optical spectroscopic observations, that this source has an orbital period of 1.7 days and a mass function $f(M) = 5.8 \pm 0.5\, M_{\odot}$ (since $f(M) \propto M sin^3(i)$, this represents a lower limit to the black hole mass). The distance and the spectral type of the secondary star are uncertain. Hynes et al. (2004) established the distance to be 6-15 kpc depending on the spectral type of the secondary (a subgiant), being later than F spectral type. Therefore, this black hole transient is a low-mass X-ray binary (LMXB). Slightly later, on the basis of binary parameters determination, Zdziarski et al. (2004) suggested the distance to be $\gtrsim$7 kpc, consistent with Hynes et al. (2004). The inclination of this binary system is known to be low, from the small emission-line velocity amplitudes observed. Wu et al. (2001) determined a plausible value for the inclination of i = 15° from spectroscopic data. This value is consistent with the fits to relativistic line models (Miller et al. 2004a,b; Miller 2006a).

GX 339–4 harbors a highly spinning black hole. This relies on the fact that very small inner disk radius of $2 - 3\,\mathrm{R_g}$ was found, implying a dimensionless spin parameter of $a > 0.8 - 0.9$ (Miller , 2006a) (where $R_g = GM/c^2$ and $a = cJ/GM^2$; see Bardeen et al. 1972; Thorne 1974). Relativistic radio jets with $v/c > 0.9$ have recently been detected (Gallo et al., 2004) during a transition from the low/hard to the high/soft state, therefore increasing the list of known microquasars showing similar radio and X-ray properties. A radio jet is usually reported in the low/hard state of GX 339–4, for which Fender et al.

(1999) reported a quenching of the radio emission during the high/soft state (by a factor of $\geq$25 compared to the low/hard state). The low/hard state would be associated by a steady state of the outflow (Corbel et al. 2000; Fender 2001; Gallo et al. 2003). It was also proposed that during state transitions the radio emission results in one or more discrete ejection events, as already observed by Gallo et al. (2004) during their detection of jets. GX 339–4 shares X-ray timing and spectral properties with the classical black hole Cyg X-1, although the former exhibits more frequent state changes and a larger dynamic range of soft X-ray luminosity (Tanaka & Lewin 1995; Zdziarski et al. 1998; Nowak et al. 1999).

Since its discovery more than 30 years ago by Markert et al. (1973), the source has been extensively studied with several optical, infrared, X-ray and $\gamma$-ray observatories. At higher energy its emission has been studied by all the major observatories, i.e., *GRANAT/SIGMA* (Grebenev et al. 1993; Bouchet et al. 1993), *CGRO/OSSE* (Grabelsky et al., 1995), *CGRO/BATSE* (Harmon et al. 1994; Rubin et al. 1998), *ASCA* (Wilms et al. (1999)), *Ginga* (Ebisawa et al. 1993; Ueda et al. 1994) and *RXTE* (e.g. Zdziarski et al. 2004; Belloni et al. 1999). Homan et al. (2005) presented a multi-wavelength study of the 2002 outburst and suggested a non-thermal jet origin for the optical/near-infrared emission in the low/hard state, while the accretion disk dominates in the high/soft state. This source is very intriguing in the optical, since its photometric optical behavior shows a very low amplitude modulation superposed by some flickering events. In addition to the QPOs detected in X-rays (usually appearing in the low/hard state and maintained in the intermediate states, while quenched in the high/soft state; see e.g. Belloni et al. 2005), this source also shows optical QPOs (f$\approx$0.064 Hz; Motch et al. 1982; Steiman-Cameron et al. 1997). A very interesting issue is also the occurrence of optical states corresponding to the X-ray states (Motch et al. 1983, 1985). These studies point out the presence of strong erratic optical and X-ray fluctuations on time scales from 20 milliseconds to seconds, as well as 7 to 20 second quasi-periodic oscillations in the low/hard state, while in the high/soft state the object does not show outstanding optical and X-ray variability. This kind of variability is difficult to explain if optical radiation comes from reprocessing of X-rays and seems to demand optical activity originated in the base of a jet.

The timing and spectral properties of GX 339–4 require a re-interpretation of the standard classification scheme of the black hole states. The behavior of GX 339–4 supports the view that, as reviewed by Homan et al. (2001) and van der Klis (2006) X-ray states are important, but they are not a simple function of the luminosity. As claimed by Homan et al. (2005), another variable apart from $\dot{M}$ drives black hole state transitions and at least two factors must drive state transitions; the second factor may be, e.g., the compactness of the corona (Homan et al., 2001). Black hole X-ray transients and related states (Tanaka & Lewin 1995; Chen et al. 1997; McClintock & Remillard 2003) provide

an excellent opportunity to investigate the importance of irradiation and non-thermal processes in the X-$\gamma$-ray spectra of X-ray binaries. Black hole binary outbursts typically begin and end in the low/hard state, with a high-energy spectrum that can be roughly described by a powerlaw with a spectral index $\Gamma$ varying in the range 1.4-2.1. At some point in the outburst (coinciding with the presence of radio outflows) the source transits to the high/soft (or thermally dominated) state, characterized by a quenching of the radio emission. Then, the luminosity is dominated by the disk thermal component peaking at a few keV and the high energy powerlaw is much softer ($\Gamma \geq 2.4$). The transition between low/hard and high/soft states usually occurs by crossing through various intermediate states (hard and soft intermediate states; Miyamoto et al. 1991a; Belloni et al. 1997; Homan & Belloni 2005, see van der Klis 2006 for a review). The transition between these states occurs very rapidly; they were found in *EXOSAT* observations by GX 339–4 by Mendez & van der Klis (1997). The spectral slope for the hard component is $1.5 - 2.5$ in these intermediate states. The Very/High (hereafter VH) state was first observed in GX 339–4 (Miyamoto et al., 1991a), when very peculiar X-ray variability was detected with *Ginga/LAC* (6 Hz QPO, 10-60 s duration dips and "flip-flops"). Miyamoto et al. (1991b) even proposed a jet model in order to account for the observed time variability in this state, on the basis of the size of the Comptonizing coronae inferred from observations of GX 339–4 in the VH state (Miyamoto et al., 1991a). Recent studies (Homan et al. 2001; Mendez & van der Klis 1997; Wolt & van der Klis 2007) point out that the VH state is really an intermediate state but at different luminosity level.

While the physical nature of the soft component is commonly associated with an optically thick accretion disk, there is no consensus about the origin of the hard powerlaw component, where a powerlaw is probably a simplification of a much more complex reality. The energy spectra include also additional components, important for the physics of accretion, such as the Fe $K_\alpha$ fluorescence feature (see, e.g., Miller 2007; Reynolds & Nowak 2003) and Compton reflection bump, both being different aspects of the same physical origin (i.e. fluorescence of the Fe atoms and Compton back-scattering, respectively, both being the most obvious reactions of an irradiated disk by a high-energy source; George & Fabian 1991). An extremely high ionisation may inhibit the formation of emission and absorption lines in the inner disk, which would explain the lack of Fe $K_\alpha$ fluorescence emission line in some systems. One important parameter to measure is the presence/absence of a high energy cut-off in the spectrum, for which observations at energies $> 20$ keV are necessary. It is known since a long time (Sunyaev & Trümper 1979; Grove et al. 1998) that the spectrum in the low/hard state does show a cut-off around 100 keV. This cut-off was interpreted as being consequence of the thermal (inverse) Comptonization of photons from the disk on a distribution of electrons thought to represent a corona (whose geometry is a matter of debate).

**Table 5.1**: *INTEGRAL* Observations Log and effective exposure times of the *INTEGRAL* and *XMM-Newton* observations.

| Epoch number | INTEGRAL (yyyy/mm/dd) | XMM/EPIC-pn [s] | JEM-X [s] | ISGRI [s] | SPI [s] | INTEGRAL rev. |
|---|---|---|---|---|---|---|
| 1 | 2007/01/30-02/01 | – | 50 784.59 | 85 265.02 | 98 324.29 | 525 |
| 2 | 2007/02/17-19 | 15 754 | 45 036.14 | 73 356.11 | 85 564.62 | 531 |
| 3 | 2007/03/04-06 | 16 702 | 49 186.59 | 93 095.65 | 107 732.7 | 536 |
| 4 | 2007/03/16-18 | – | 50 965.92 | 82 634.55 | – | 540 |
| 5 | 2007/03/29-31 | 18 294 | 63 647.40 | 93 654.59 | – | 544 |

In this Chapter we report on spectral analysis of simultaneous *INTEGRAL* and XMM/EPIC-pn data, during five and three Target of Opportunity observations of GX 339–4, respectively, occurring between 2007 January 30 and March 31. During these observations GX 339–4 began in a low/hard state and evolved to softer intermediate states. Fits with both phenomenological and EQPAIR models are presented in Section 5.3 and we end with the discussion of the results in Section 5.4.

## 5.2 Observations

In 2006 November, X-ray activity of GX 339–4 was detected with the Rossi X-ray Timing Explorer (RXTE; Swank et al. (2006)). The source had an almost constant flux until end of December 2006, when the hard (15-50 keV) X-ray flux increased by a large amount. It reached its brightest level since 2004 November, as detected by SWIFT/BAT (Krimm et al., 2006). At the end of January 2007, observations were triggered with the *INTEGRAL* satellite (Miller et al., 2007). During following months, the source underwent an evolution from the low/hard to softer states, as shown in preliminary results reported in Caballero-García et al. 2007b,c,d,e,f. Observations in radio with ATCA during February 4 to 18 revealed that the source was undergoing a series of plasma ejection events (Corbel et al., 2007). Our *INTEGRAL* observations cover 5 Target of Opportunity observations of ≈130 ks each, spread from 2007 January 30 to March 31. We carried out a series of ToO observations with the *XMM-Newton* satellite, simultaneous with the second, third and fifth *INTEGRAL* observations. Details about the dates and exposure times appear in Table 5.1.

### 5.2.1 INTEGRAL

Our program consisted of 5 ToO observations with *INTEGRAL*, of ≈130 ks each, spread from 2007 January 30 to March 31 (we will refer to these as epochs 1–5 below; see Table 5.1 for more details). The differences in the exposure times between the *INTEGRAL* instruments given in Table 5.1 (JEM-X, ISGRI and SPI) are due to the difference in the dead times and variation in the efficiency along the fields of view. The dithering pattern used during the observations was 5×5 (square of 25 pointings separated by 2.17 degrees centered on the main target of the observation); this is the best pattern in order to minimize background effects for the SPI and ISGRI instruments in crowded fields. Data reduction (in the case of JEM-X, ISGRI and SPI) was performed using the standard Off-line Science Analysis (OSA) 7.0 software package available from the *INTEGRAL* Science Data Centre (ISDC).

Because of the steep fall in response in the case of JEM-X, and because of its reduced FOV (≈5° of diameter), we limited the pointing radius with respect to the GX 339–4 position to be within 4°. In the case of SPI and ISGRI, with large Fully Coded Fields of Views (FCFOV) (16°×16° for SPI and 8.3°×8° for ISGRI), pointing selections were not necessary. In total, 254, 149 and 105 pointings (or Science Window – each having exposure times lasting from 1800 to 3600 s and following a 5×5 dithering pattern on the plane of the sky) data were used for SPI, ISGRI and JEM-X, respectively. The difference in the number of pointings between SPI and ISGRI is due to the fact that in epoch 4 and 5 the source was too weak in hard X-rays ($E > 20$ keV) to be detected with SPI. Due to the fact that SPI is a high resolution spectrograph in its energy range (20-8 000 keV), it is not optimized for the detection of sources without taking into account previous information about the spatial distribution of them. Thus, we used as an input catalog of sources those obtained from the ISGRI in the (20-40) keV mosaic images.

The signal from GX 339–4 was too soft to detect any emission in the last two epochs with SPI. We combined single revolution SPI spectra from epochs 1–3, considering that there was no significant evolution, in order to increase the signal to noise ratio. The same was done for the low energy instruments (JEM-X and ISGRI), thus obtaining five spectra, namely one for each epoch, as can be seen in Table 5.1. We applied 2% systematic errors to the JEM-X, ISGRI and SPI spectra. We restricted our analysis in the energy ranges of $5-20$, $18-200$ and $23-800$ keV for the JEM-X, ISGRI and SPI spectral analysis, respectively, as recommended by the OSA cookbook. The SPI and ISGRI spectra were rebinned at high energies ($\gtrsim$200 keV) with the FTOOL `grppha` procedure to reach the detection level of $3\sigma$ per spectral bin.

### 5.2.2 XMM/EPIC-pn

The *XMM-Newton* Observatory (Jansen et al., 2001) includes three 1 500 $cm^2$ X-ray telescopes each with an *European Photon Imaging Camera* (EPIC; 0.1–15 keV) at the focus. Two of the EPIC imaging spectrometers use MOS CCDs (Turner et al., 2001) and one uses pn CCDs (Strüder et al., 2001). The *Reflection Grating Spectrometer* (RGS; 0.35–2.5 keV, Den Herder et al., 2001) are located behind two of the telescopes. In addition, there is a co-aligned 30 cm diameter Optical/UV Monitor telescope (OM, Mason et al., 2001), providing coverage simultaneous with the X-ray instruments.

GX 339–4 was observed by *XMM-Newton* for 16.8 ks on 2007 February 19 (hereafter called Obs 1 and coinciding with *INTEGRAL* Epoch 2), for 17.8 ks on 2007 March 5 (hereafter called Obs 2 and coinciding with *INTEGRAL* Epoch 3) and for 20 ks on 2007 March 30 (hereafter called Obs 3 and coinciding with *INTEGRAL* Epoch 5). Refer to Tables 5.1 and 5.2 for details.

The thin optical blocking filter was used with the EPIC camera. The EPIC pn camera was operated in burst mode due to the high count rate of the source (from $\gtrsim$6700 $s^{-1}$ to $\gtrsim$3000 $s^{-1}$ for Obs 1 to 3, respectively). For the same reason, the EPIC MOS cameras were not operated. The individual RGS1 and RGS2 CCD chips were read out sequentially. This reduces the frame time from 4.8 to 0.6 seconds (4.8/8) and consequently the pile-up by almost an order of magnitude. All the X-ray data products were obtained from the *XMM-Newton* public archive and reduced using the Science Analysis Software (SAS) version 7.1.0. In pn burst mode, only one CCD chip (corresponding to a field of view of $13'6 \times 4'4$) is used and the data from that chip are collapsed into a one-dimensional row ($4'4$) to be read out at high speed, the second dimension being replaced by timing information. The duty cycle is only 3%. This allows a time resolution of 7 $\mu$s, and photon pile-up occurs only for count rates above 60 000 $s^{-1}$. Only single and double events (patterns 0 to 4) were selected. Ancillary response files were generated using the SAS task `arfgen`. Response matrices were generated using the SAS task `rmfgen`.

PN Charge Transfer Inneficiency (CTI) rate dependency has been observed for count rates $> 200 - 300$ cts/s, i.e. for very bright sources CTI correction over predicts the CTI losses. This can result in an up to 2% apparent gain shift most visible for spectral features like edges or lines [1]. Hereafter, we applied 2% systematic errors to the EPIC-pn spectra reported below. We used pn data in the 0.7–10 keV energy range.

[1] For details see: http://xmm.esac.esa.int/external/xmm_sw_cal/calib/index.shtml (EPIC Calibration Status Document), page 4.

**Table 5.2**: *XMM-Newton* Observation Log data.

| INTEGRAL epoch number | XMM Observation ID | XMM UTC Start time (hh:mm ; yyyy/mm/dd) | XMM UTC End time (hh:mm ; yyyy/mm/dd) |
|---|---|---|---|
| 1 | – | – | – |
| 2 | 0410581201 | 00:03 ; 2007/02/19 | 04:44 ; 2007/02/19 |
| 3 | 0410581301 | 11:15 ; 2007/03/05 | 16:12 ; 2007/03/05 |
| 4 | – | – | – |
| 5 | 0410581701 | 14:34 ; 2007/03/30 | 20:07 ; 2007/03/30 |

## 5.3 Spectral analysis of INTEGRAL and XMM-Newton data

We performed fits to the combined JEM-X, ISGRI and when available SPI and XMM/EPIC-pn spectra, for each of the five epochs (see Table 5.1) using XSPEC (Arnaud , 1996) v.11.3. All errors quoted in this work are 90% confidence errors, obtained by allowing all variable parameters to float during the error scan. The hydrogen column density was set to be free when XMM/EPIC-pn data were available and fixed at $N_H = 0.5 \times 10^{22}$ atom $cm^{-2}$ (Dickey & Lockman, 1990) when only *INTEGRAL* data were available.

Our main aim with these fits is to characterize the broad continuum thanks to the broad *XMM-Newton* and *INTEGRAL* spectral coverage. To account for uncertainties in relative instrument calibrations, we fixed JEM-X multiplicative calibration constant to 1 and let that of ISGRI and SPI free to vary in the fits for the different data sets as shown in Table 5.4. In the case of using both INTEGRAL and XMM/EPIC-pn spectra, we fixed the EPIC-pn multiplicative constant to 1 and let that of JEM-X, ISGRI and SPI free to vary, in order to account for cross-calibration uncertainties as well [2]. The presence of an XMM/EPIC-pn instrumental line was clear in the spectra of epochs 2 and 3 and we added a gaussian emission line centered at 2.28 keV and 2.25±0.03 keV, respectively. For epoch 5 two absorption instrumental lines arised, centered at 1.82 keV and 2.14 keV, respectively. These lines are compatible with instrumental Si and Au edges of the XMM/EPIC-pn detector.

[2]We restricted the values of the multiplicative constants to be ≈1±20%, 1±30%, 1±60% for JEM-X, ISGRI and SPI relative to XMM/EPIC-pn in order to obtain reliable fits. When XMM/EPIC-pn data was not available, the same ratio between the constants was preserved.

### 5.3.1 Fits of joint XMM/EPIC-pn and INTEGRAL spectra with phenomenological models

We performed preliminary fits to the spectra of every single epoch with the phenomenological model consisting of a multicolor disk black body (`diskbb` in XSPEC) of Mitsuda et al. (1984) plus a powerlaw in order to describe the high-energy emission. As shown below, this seems to be a good phenomenological description for epochs 2, 4 and 5. Details about the fits and the parameters obtained can be seen below and in Table 5.4. We shall show that a reflection hump plus a cut-off at around 66 keV is necessary to properly describe the high-energy spectrum of epoch 1. Particularly interesting are the presence of a broad and skewed Fe $K_\alpha$ line plus the reflection hump observed in epoch 3. All these issues are discussed below both phenomenologically and physically.

In epoch 1 a model consisting of `constant*phabs(powerlaw)` was not a good description of the data ($\chi^2_\nu = 35$, $\nu = 98$). The situation improved dramatically ($\chi^2_\nu = 2.35$, $\nu = 96$) when a cut-off was included in the model (i.e. `constant(powerlaw)highecut`; $E_c = 40 - 70$ keV). Nevertheless, some low-energy positive residuals at E$\approx 6 - 7$ keV remained and in the form of an edge at $\approx$10 keV indicating the presence of a broad Fe $K_\alpha$ line and reflection. When an absorption Fe edge at E = 9.6$\pm$0.2 was added, the statistics improved by $\Delta\chi^2_\nu = 0.95$. Additional improvement was made by including a broad Fe gaussian line centered at $E_{Fe} = 6.4 - 6.97$ ($\Delta\chi^2_\nu = 0.1$) [3]. Taking all these considerations into account, we decided to substitute the simple powerlaw in the fits by a reflected `pexriv` powerlaw. We fitted with a `constant*phabs(gaussian + pexriv)` model, which includes reflection of a high-energy distribution of photons in the form of a powerlaw. We obtained relatively good statistics ($\chi^2_\nu = 2.7$; $\nu = 93$). The `pexriv` component included a cut-off powerlaw with a folding energy at $E_f = 66\pm2$ keV for the epoch 1. In this epoch, if the cut-off powerlaw is substituted by a flat powerlaw (i.e. with no cut-off) the fit largely worsened ($\chi^2_\nu = 8.5$; $\nu = 86$). Thus, we have concluded that there is a cut-off in the spectrum of epoch 1 ($\Delta\chi^2_\nu = 5.8$; thus 90% of probability of being significant) which is not caused by reflection. For the epoch 1 addition of a multi-color disk component (`diskbb`) improved the fit by $\Delta\chi^2_\nu = 1.2$.

In epoch 2 a model consisting of `constant*phabs(diskbb + powerlaw)` was not a good description of the data ($\chi^2_\nu = 3.05$, $\nu = 150$). Low-energy positive residuals in the form of an excess near 1 keV were detected in the XMM/EPIC-pn spectrum and the fit improved largely when considered ($\chi^2_\nu = 1.9$, $\nu = 144$). This feature is detected in a number of X-ray binaries and has been preciously modeled either as an emission line, or as an edge, and its nature is unclear (e.g. Kuulkers et al. 1997; Sidoli et al. 2001; Boirin

[3] The detection of a broad Fe $K_\alpha$ line is very low, and can be understood by the fact that JEM-X is not well suited for the detection of this feature, as we will show in the fits for epoch 3, for which this line was clearly detected with XMM/EPIC-pn.

et al. 2003; Díaz Trigo et al. 2007). If the feature has astrophysical origin, it would be consistent with a blend of Ne IX and Ne X emission, or Fe L.

In epoch 3 a model consisting of `constant*phabs(powerlaw + diskbb)` was not a good description of the data ($\chi^2_\nu = 17$, $\nu = 147$). Positive residuals centered at $\approx 1, 6 - 7, 20 - 30$ keV arised. As in epoch 2, we included a a gaussian emission line centered at $\approx$1 keV and the fit largely improved ($\chi^2_\nu = 9.0$, $\nu = 144$). Residuals compatible with a broad and skewed Fe $K_\alpha$ line plus the reflection bump arised (see Figure 5.2) and we took these features into account by fitting with a `constant*phabs(refsch + diskline + gaussian + diskbb)` model getting a significantly improved fit ($\chi^2_\nu = 2.5$, $\nu = 147$). The `diskline` model takes into account line emission from a relativistic accretion disk (Fabian et al., 1989) and `refsch` is the corresponding reflected powerlaw convolved with the relativistic disk line profile (Magdziarz & Zdziarski, 1995). We fixed the inner disk inclination to 20° and the ionization parameter to $x_i = 500\,\mathrm{erg}\,cm/s$. The obtained value for the emissivity index profile was rather steep ($q = 4.6 \pm 0.8$) and the reflection covering factor significantly different from zero ($\Omega/2\pi = 0.45 \pm 0.11$). The former indicates that the primary source is very close to the black hole. Comparable emissivity indices ($\approx$7) have been observed from a number of Seyfert galaxies (e.g. Fabian et al. 2004, 2005) and are indicative of a primary source very close to the black hole. The presence of a broad and skewed Fe $K_\alpha$ has been also understood as high-energy emission originating close to the black hole (see Miller 2008 for relativistic fits of this line for GX 339–4).

In epoch 4 a model consisting of `constant*phabs(diskbb + powerlaw)` was a good description of the data ($\chi^2_\nu = 1.7$, $\nu = 46$). Eventually, in epoch 5 a model consisting of `constant*phabs(diskbb + powerlaw)` was not a good description of the data and an excess at $\approx$1 keV arised ($\chi^2_\nu = 2.6$, $\nu = 97$). When including an emission gaussian line centered at $\approx$1 keV, the fit largely improved ($\chi^2_\nu = 1.8$, $\nu = 94$).

The values obtained for the fitted parameters with the best phenomenological fit are shown in Table 5.4 and the fitted spectra are shown in Figure 5.1 and 5.3. We refer to Section 5.3.2, where fits of the same spectrum are shown with EQPAIR Comptonization model. In Table 5.3 and in Figures 5.5, 5.6 and 5.7 we show the evolution of the outburst. In Section 5.4 we discuss the evolution of the spectra regarding hardness and evolution of states in black holes.

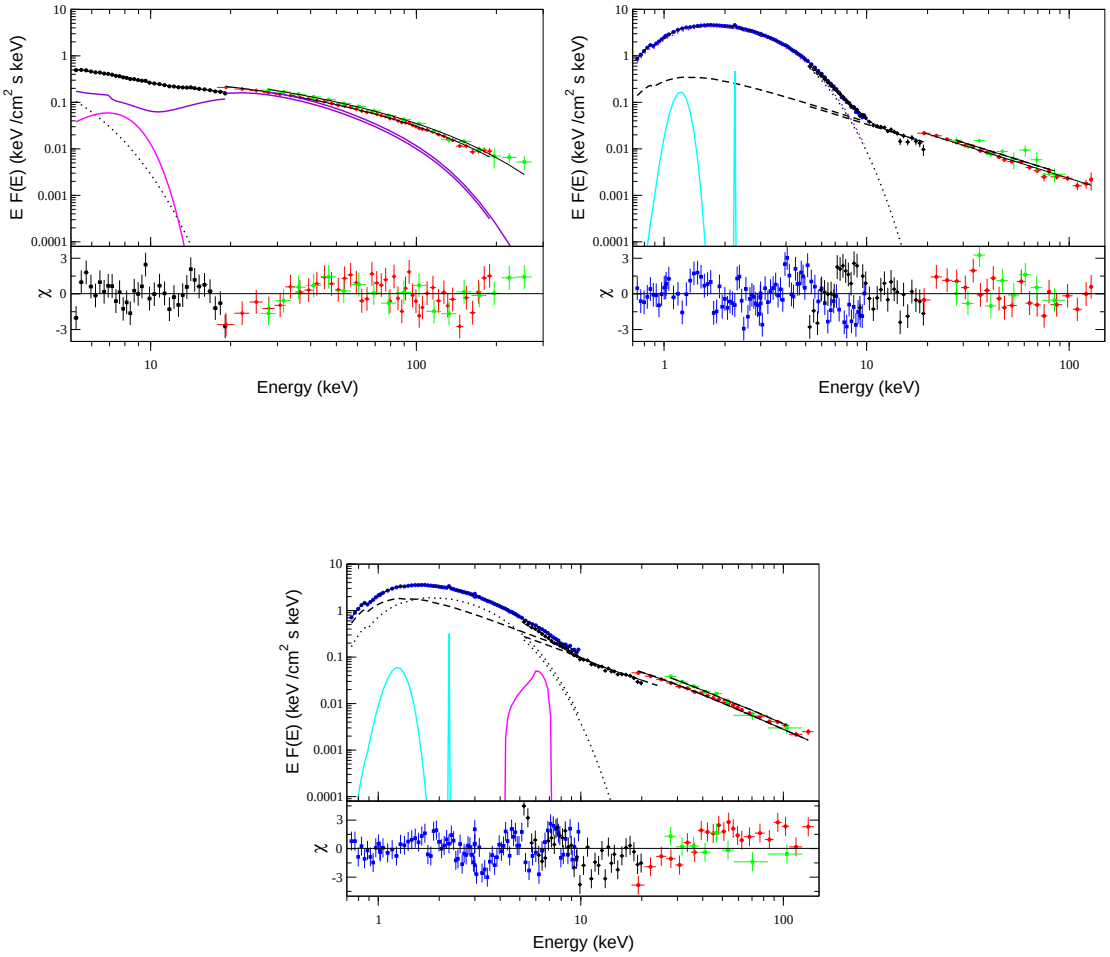


**Figure 5.1**: Unfolded INTEGRAL and XMM/EPIC-pn spectra (blue, black, red and green for the XMM/EPIC-pn, JEM-X, ISGRI and SPI data, respectively) from epochs 1 to 3 (upper-left to lower-right) fitted with descriptive phenomenological models. The continuum line shows the total model (see the text Section 5.3.1 and Table 5.4 for details), the dotted, violet and dashed lines show the accretion disk, the reflection and the powerlaw components, respectively, and the magenta line represents relativistically broadened FeK$_\alpha$ emission from a disk. The cyan colored gaussian lines mean instrumental XMM/EPIC-pn effects.

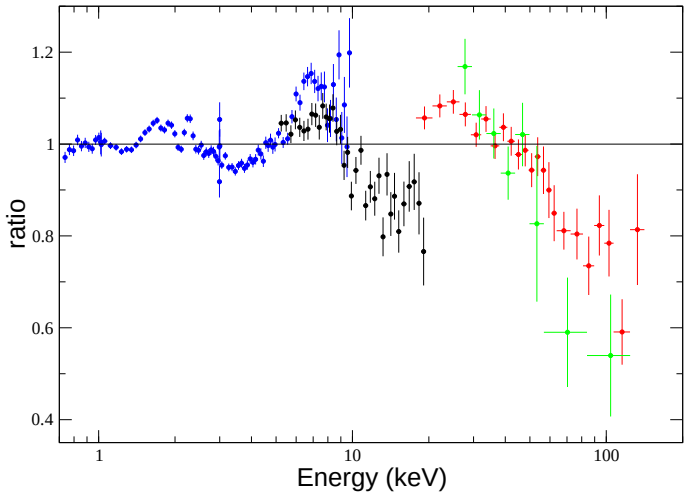


**Figure 5.2**: The plot above shows the data/model ratio obtained when the *INTEGRAL* and *XMM-Newton* data of epoch 3 is fitted with a phenomenological disk plus power-law model. A relativistically broadened Fe K$_\alpha$ line is clearly present. The curvature at high energy is a clear signature of disk reflection.

**Table 5.3**: Luminosities and parameters (with $\Gamma$ and $E_c$ being the photon index and the cut-off energy, respectively, for the high-energy powerlaw component).

| Epoch number | $L_{disk}$ [erg/s] | $L_{pow}$ [erg/s] | $L_{total}$ [erg/s] | $\Gamma$ | $E_c$ [keV] | $F_{disk}/F_{pow}$ |
|---|---|---|---|---|---|---|
| 1 | $3.0\pm0.7\times10^{36}$ | $1.9\pm0.4\times10^{38}$ | $1.9\pm0.5\times10^{38}$ ($0.3L_{Edd}$) | $1.46\pm0.03$ | $66\pm2$ | 0.02 |
| 2 | $3.1\pm0.7\times10^{38}$ | $4.7\pm1.1\times10^{37}$ | $3.6\pm0.8\times10^{38}$ ($0.5L_{Edd}$) | $2.33\pm0.02$ | – | 7.0 |
| 3 | $1.3\pm0.4\times10^{38}$ | $2.2\pm0.6\times10^{38}$ | $3.5\pm1.0\times10^{38}$ ($0.5L_{Edd}$) | $2.78\pm0.10$ | – | 0.6 |
| 4 | $4.4\pm0.6\times10^{36}$ | $1.2\pm0.2\times10^{37}$ | $1.6\pm0.2\times10^{37}$ ($0.02L_{Edd}$) | $2.24\pm0.04$ | – | 0.4 |
| 5 | $1.1\pm0.2\times10^{38}$ | $2.9\pm0.5\times10^{37}$ | $1.5\pm0.3\times10^{38}$ ($0.4L_{Edd}$) | $2.72^{+0.06}_{-0.03}$ | – | 4.0 |

Notes to Table 5.3

[1]Disk luminosities reported for epoch 4 are underestimated because XMM/EPIC-pn ($0.6-10$ keV) data was not available.

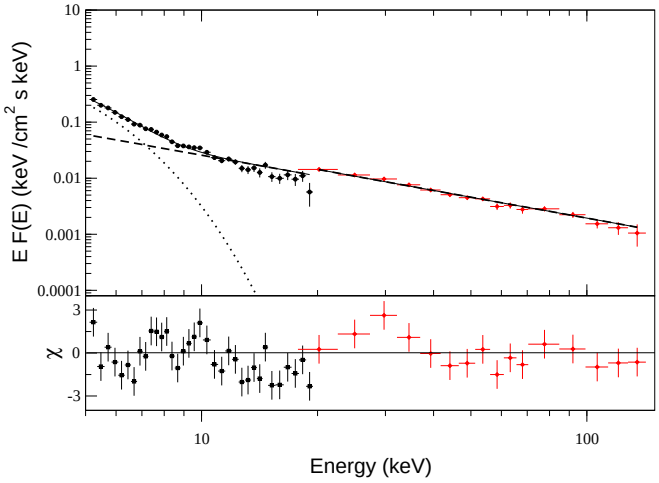


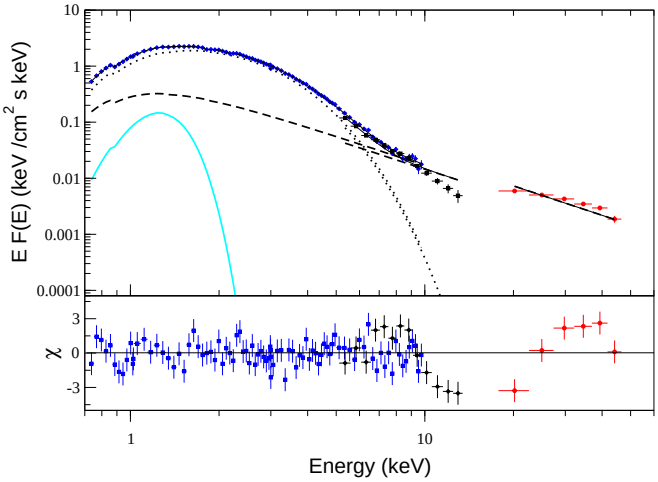


**Figure 5.3**: For epochs 4 and 5 spectral evolution occurred in the form of a gradual softening. See Section 5.3.1 for more details.

**Table 5.4**: Parameters obtained for the best fits of the joint XMM/EPIC-pn, JEM-X, ISGRI and SPI spectra (see text for details).

| Parameter | Epoch 1 | Epoch 2 | Epoch 3 | Epoch 4 | Epoch 5 |
|---|---|---|---|---|---|
| | | Powerlaw | | | |
| $\Gamma$ | – | 2.33±0.02 | – | 2.24±0.04 | $2.72^{+0.06}_{-0.03}$ |
| $N_{pow}$ [ph/keV/s/cm$^2$] at 1 keV | – | $0.89^{+0.06}_{-0.03}$ | – | 0.45±0.07 | $0.90^{+0.15}_{-0.03}$ |
| | | Reflected powerlaw | | | |
| $\Gamma$ | 1.46±0.03 | – | 2.78±0.10 | – | – |
| $E_f$ [keV] | 66±2 | – | 0 (f) | – | – |
| $\Omega/2\pi$ | 0.02±0.02 | – | 0.45±0.11 | – | – |
| N $[ph/keV/cm^2/s]$ | 0.94±0.06 | – | 6.23±0.22 | – | – |
| | | phabs | | | |
| $N_H$ [cm$^{-2}$] | $0.5\times10^{22}$ (f) | $0.467\pm0.008\times10^{22}$ | $0.59\pm0.01\times10^{22}$ | $0.5\times10^{22}$ (f) | $0.47\pm0.02\times10^{22}$ |
| | | diskbb | | | |
| $kT_{in}$ [keV] | 0.67±0.13 | 0.891±0.003 | $0.915^{+0.011}_{-0.007}$ | 0.91±0.04 | 0.698±0.005 |
| $N_{bb}$ $[(R_{in}[km]/D[10kpc])^2\times\cos\theta]$ | $179^{+69}_{-26}$ | $2\,292^{+13}_{-20}$ | $983^{+50}_{-73}$ | $651^{+267}_{-187}$ | $2\,511^{+99}_{-83}$ |
| | | gaussian$_1$ (emission ins.) | | | |
| $E_{gauss}$ [keV] | – | 2.28 (f) | 2.25±0.03 | – | – |
| $\sigma$ [keV] | – | 0(f) | 0(f) | – | – |
| $N_{gauss}$ [ph/cm$^2$/s] | – | 0.012±0.007 | 0.015±0.006 | – | – |

**Table 5.4**: (Continued.)

| | Epoch 1 | Epoch 2 | Epoch 3 | Epoch 4 | Epoch 5 |
|---|---|---|---|---|---|
| | | | gaussian$_2$ (absorption ins.) | | |
| $E_{gauss}$ [keV] | – | – | – | – | 1.82±0.04 |
| $\sigma$ [keV] | – | – | – | – | $< 0.1$ |
| $N_{gauss}$ [ph/cm$^2$/s] | – | – | – | – | 0.02±0.01 |
| | | | gaussian$_3$ (absorption ins.) | | |
| $E_{gauss}$ [keV] | – | – | – | – | 2.14±0.06 |
| $\sigma$ [keV] | – | – | – | – | $0.07^{+0.03}_{-0.05}$ |
| $N_{gauss}$ [ph/cm$^2$/s] | – | – | – | – | $0.011^{+0.005}_{-0.007}$ |
| | | | Broad gaussian$_4$ (Fe) | | |
| $E_{gauss}$ [keV] | 6.55±0.15 | – | 6.9±0.4 | – | – |
| $\sigma$ [keV] | 1.63±0.20 | – | – | – | – |
| $N_{gauss}$ [ph/cm$^2$/s] | $0.035^{+0.004}_{-0.007}$ | – | 0.013±0.001 | – | – |
| | | | Broad gaussian$_5$ ($\approx$ 1keV) | | |
| $E_{gauss}$ [keV] | – | 1.18±0.02 | 1.20±0.05 | – | 1.13±0.05 |
| $\sigma$ [keV] | – | 0.09±0.01 | 0.14±0.03 | – | 0.16±0.05 |
| $N_{gauss}$ [ph/cm$^2$/s] | – | 0.07±0.01 | 0.04±0.01 | – | 0.08±0.03 |

**Table 5.4**: (Continued.)

| | Epoch 1 | Epoch 2 | Epoch 3 | Epoch 4 | Epoch 5 |
|---|---|---|---|---|---|
| | | Intrumental normalization factors | | | |
| $C_{XMM/EPIC-pn}$ | – | 1.0 (f) | 1.0 (f) | – | 1.0 (f) |
| $C_{JEM-X}$ | 1.0 (f) | 0.89±0.01 | 0.81±0.06 | 1.0 (f) | 0.85±0.03 |
| $C_{ISGRI}$ | 1.35±0.02 | 1.39±0.02 | 1.20±0.07 | 1.30±0.12 | 1.36±0.03 |
| $C_{SPI}$ | 1.57±0.02 | 1.56±0.04 | 1.50±0.11 | – | – |
| $\chi^2_\nu$ | 1.50 | 1.9 | 2.53 | 1.72 | 1.77 |
| $\nu$ | 91 | 144 | 147 | 46 | 94 |

Notes to Table 5.3

[1]Parameters fixed in the fits are denoted by 'f'.

[2]EPIC-pn instrumental absorption features are implemented in XSPEC with negative gaussian profiles.

[3]The models used are `constant*phabs(diskbb+gaussian+pexriv)` for epoch 1,
`constant*phabs(gaussian+gaussian+diskbb+powerlaw)` for epoch 2,
`constant*phabs(refsch+diskline+diskbb+gaussian+gaussian)` for epoch 3,
`constant*phabs(diskbb+powerlaw)` for epoch 4 and
`constant*phabs(diskbb+gaussian+gaussian+gaussian+powerlaw)` fo epoch 5. See text in Section 5.3.1 for more details.

### 5.3.2 Fits to the low/hard state with the EQPAIR model: thermal versus non-thermal Comptonization

In this Section we study what kind of particles constitute the plasma (kinematics and geometry) responsible for the Comptonization of the photons from the accretion disk in the low/hard state observed during epoch 1. In this sense, we applied the EQPAIR Comptonization model (developed by Coppi 1999) because it deals with both thermal and non-thermal distributed particles in the plasma.

The model (EQPAIR) takes into account angle dependence, Compton scattering (up to multiple orders), photon pair production, pair annihilation, bremsstrahlung, as well as reflection from a cold disk. This model incorporates both line smearing due to relativistic motion in the disk (as in the `diskline` model in XSPEC; Fabian et al. 1989) and ionized Compton reflection (i.e. `pexriv` model in XPSEC; Magdziarz & Zdziarski 1995). we considered reflection from a concentrated high-energy central source, so we froze the emissivity index ($\beta$) from the `diskline` model to a fiducial positive value (+3) in all our fits (where $J(r) \propto r^{-q}$). In this scenario very small values for the reflection covering factor (R) would be expected.

The `eqpair` model provides the injection of a non-thermal electron distribution with Lorentz factors between $\Gamma_{min}$ and $\Gamma_{max}$ and a powerlaw spectral index $\Gamma_p$. The cloud is illuminated by soft thermal photons emitted by an accretion disk. These photons serve as seed for inverse Compton scattering by both thermal and non-thermal electrons. The system is characterized by the power (i.e. luminosity) $L_i$ supplied by its different components. We express each of them dimensionlessly as a compactness parameter, $\mathrm{l}_i = \mathrm{L}_i\sigma_\mathrm{T}/(\mathrm{Rm}_e\mathrm{c}^3)$, where R is the characteristic dimension and $\sigma_\mathrm{T}$ the Thompson cross-section of the plasma. Thus, $\mathrm{l}_s$, $\mathrm{l}_{th}$, $\mathrm{l}_{nth}$ and $\mathrm{l}_h = \mathrm{l}_{th} + \mathrm{l}_{nth}$ correspond to the power in soft disk entering the plasma, thermal electron heating, electron acceleration and the total power supplied to the plasma. The total number of electrons (not including $\mathrm{e}^+\mathrm{e}_-$ pairs) is determined by $\tau_\mathrm{T}$, the corresponding Thompson optical depth, measured from the center to the surface of the scattering region. If we consider injection from pairs $\mathrm{e}^+\mathrm{e}_-$, then the total optical depth of the thermalized scattering electrons/pairs is expected to be $\tau_\mathrm{T} \geq \tau_\mathrm{P}$.

We first performed fits with with a model constituted by `constant*phabs(eqpair)` in both cases of thermal and non-thermal dominated plasmas. Overall, we obtained a good description of the high-energy spectrum but with worse description of the data at lower energy bins ($\mathrm{E} < 20\,\mathrm{keV}$) ($\chi^2_\nu = 3.51, 3.60$, respectively). Residuals in the form of a broad Fe $\mathrm{K}_\alpha$ line arised that led us to fit with the model `constant*phabs(gaussian+eqpair)` with $\mathrm{E}_\mathrm{Fe} = 6.4 - 6.97\,\mathrm{keV}$ and $\sigma_\mathrm{Fe} = 1.5{\pm}0.3, 1.4{\pm}0.8\,\mathrm{keV}$, respectively. This improved the fits in both cases ($\chi^2_\nu = 1.8, 1.7$, respectively). Slight improvement was made by including a multi-color disk component of Mitsuda et al. (1984) (`constant*phabs(diskbb+gaussian+eqpair)`) leading to our final fits ($\chi^2_\nu = 1.3, 1.2$, respectively). The inner disk temperatures

derived are $T_{in} = 0.57\pm0.03, 0.8\pm0.5$ keV.

We considered the source of soft photons to be moderately compact, by fixing $l_s = 10$, as commonly reported for other sources with similar characteristics. We made fits with a plasma constituted by single $e^-$, injected with Lorentz factors from $\Gamma_{min} = 1.3$ to $\Gamma_{max} = 100$. The obtained power-law injection indices obtained are $\Gamma_p = 0, 4.04\pm0.21$, for thermal dominated and non-thermal dominated plasma, respectively, indicating dominance of low-relativistic particles in the latter case. The limits of the accretion disk were fixed to $R_{max} = 100\,R_g$ and $R_{min} = 2\,R_g$, corresponding to a maximally rotating black hole. We attempted to fit the reflection covering factor by fixing the inclination angle to a fiducial value of $i = 20°$. The ionisation was find to be low, and the best result was obtained by setting the ionisation parameter to zero ($x_i = 0$). The reflection covering factor was found to be $R = \Omega/2\pi = 0.10\pm0.06, 0.12\pm0.18$. This value (R) approximately measures the solid angle subtended by the reflecting medium as seen from the source of the primary radiation, so that $R = 1$ for an isotropic point source above an infinite optically thick slab. The values obtained for the reflection covering factor were rather low, as expected for a low/hard state (Nowak et al., 2002). Opacity was found to be $\tau_p = 2.5\pm0.3, 2.34\pm0.08$ as previously reported by Nowak et al. (2002) and by Wilms et al. (2006) for Cyg X–1. The compactness ratio (photons coming from a corona against photons from the disk) was found to be $l_h/l_s = 6.3\pm1.8, 13.0\pm0.8$ for thermal and non-thermal cases, respectively. The value found for the non-thermal case is high, even more than previously found for Cyg X–1 during the low/hard state (Wilms et al. 2006; Ibragimov et al. 2005).

Overall, the statistics obtained for thermal dominated and non-termal dominated plasma was $\chi^2_\nu = 1.3, 1.2$ ($\nu = 83, 84$), thus both being formally acceptable fits. In Section 5.4 we will discuss the implications of these results in the context of a jet dominated scenario.

The broad-band spectrum, residuals and best fit paramaters (correponding to both thermal and non-thermal dominated plasma) are presented in Table 5.5 and in Figure 5.4.

## 5.4 Discussion

### 5.4.1 Results

Our *INTEGRAL* and *XMM-Newton* observations of GX 339–4 cover the spectral evolution from the low/hard state to softer intermediate states. This spectral evolution involves very significant spectral changes which are strongly correlated. The changes in the spectral shape are strongly correlated with the ratio of the powerlaw to the disk luminosity. In Tables 5.3 and 5.4 we summarize the values for the photon indices of the powerlaw (analyzed in Section 5.3.1) and un-absorbed luminosities of both the powerlaw

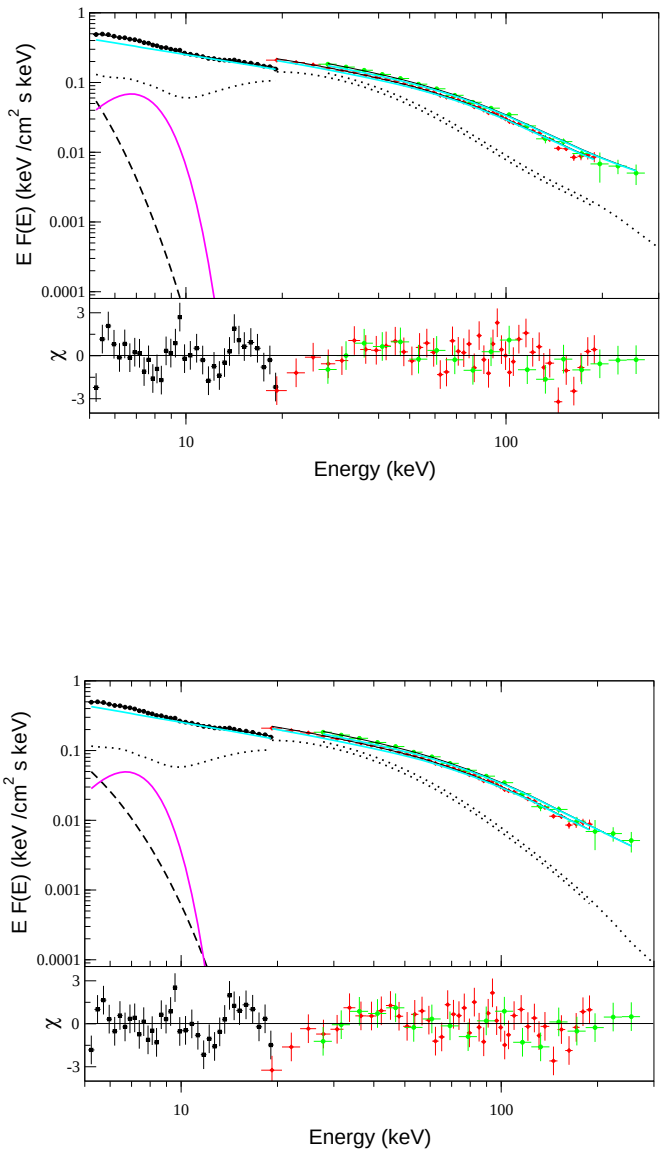


**Figure 5.4**: Fitted unfolded INTEGRAL spectra, corresponding to epoch 1 (low/hard state), fitted with the model EQPAIR for thermal dominated (top) and non-thermal dominated (bottom) plasma (see Table 5.5 for details). Cyan line shows the inverse Comptonized component, magenta line the relativistically broadened Fe $K_\alpha$ line, dashed and dotted lines the multi-color black body disk component and the reflection component, respectively. The residuals of these fits are also shown (black, red and green for JEM-X, ISGRI and SPI, respectively).

**Table 5.5**: Model parameters for both the EQPAIR thermal dominated and non-thermal dominated population of electrons applied to epoch 1 (see Section 5.3.2 to get more details). These models represent XSPEC local minima and the errors must be taken with caution.

| Parameter | EQPAIR single $e^-$ | EQPAIR with pairs |
|---|---|---|
| $l_s$ | 10(f) | 10(f) |
| $l_h/l_s$ | 6.3±1.8 | 13.0±0.8 |
| $l_{nth}/l_h$ | 0.43±0.05 | 1(f) |
| $\tau_p$ | 2.34±0.08 | 2.5±0.3 |
| pairinj | 0(f) | 0(f) |
| $\Gamma_{\rm p}$ | 0 | 4.05±0.21 |
| $\Gamma_{\rm min}$ | 1.3(f) | 1.3(f) |
| $\Gamma_{\rm max}$ | 100(f) | 100(f) |
| Refl $[\Omega/2\pi]$ | 0.10±0.06 | 0.12±0.18 |
| $\beta$ | 3(f) | 3(f) |
| xi $[4\pi F_{\rm irr}/n]$ (erg×cm/s) | 0(f) | 0(f) |
| $C_{\rm JEM-X}$ | 1(f) | 1(f) |
| $C_{\rm ISGRI}$ | 1.34±0.02 | 1.39±0.03 |
| $C_{\rm SPI}$ | 1.54±0.03 | 1.59±0.03 |
| $\chi^2_\nu$ | 1.3 | 1.2 |
| $\nu$ | 83 | 84 |

and the disk (assuming a distance to the source of 8.5 kpc). In the first epoch the source was in the so-called low/hard state, with almost no disk contribution in the spectrum. It showed a cut-off at $E_c = 66\pm2$ keV in the powerlaw. The cut-off disappeared in the second epoch and the powerlaw emission decreased notably, being only the 1/7 of the disk luminosity. In the third epoch the spectrum hardened again considerably (the powerlaw luminosity being 1.7 times higher than the disk luminosity, the latter decreased by 50% with respect to the second epoch). The total luminosity remained more or less unchanged during epochs 2, 3 and 5 (the latter decreased by 10%), coinciding with *XMM-Newton* simultaneous observations. The luminosities obtained for all the epochs [4] were $\gtrsim$10 percent the Eddington luminosity (considering a black hole of $6M_\odot$).

The main features of the low/hard state (epoch 1) are a rather flat photon index ($\Gamma\approx1.5$) and the clear presence of a high-energy cut-off at 66±2 keV. Both being typical characteristics of low/hard state. This value for the photon index resemble that found previously (Belloni et al. 2006; Grove et al. 1998) in low/hard states and the value for the cut-off that found by Belloni et al. (2006) during a hard intermediate state. During epochs 2 and 3 the spectra are characterized by a flat (plus reflection features in the case of epoch 3) and steeper high-energy emission ($\Gamma\approx2.5$). In the classification scheme of Homan & Belloni (2005), these would correspond to the soft intermediate state. These values resemble those reported previously by Nespoli et al. (2003) ($\Gamma = 2.44\pm0.10$) and Belloni et al. (2006) ($\Gamma = 2.3$) during soft intermediate states of GX 339–4 as well. The spectrum

[4] Underestimated for epochs 1 and 4 because XMM data was not available.

during epoch 5 is characterized by flat and very steep high energy emission ($\Gamma \approx 3.0$). As can be seen in Figure 5.6 and 5.7 the hardness ratio (defined as HR=(2-10) keV)/(0.2-2) keV) of the XMM/EPIC-pn light curve is very soft in epoch 5. This value for the photon index keeps epoch 5 in the soft intermediate state as well, as considered from the classification scheme of Homan & Belloni (2005). The luminosity in the (20-100) keV energy range is very low in epoch 5 and resembles that found in ultrasoft states for other sources, as Cyg X–3 (Beckmann et al., 2007).

### 5.4.2 The source of the high-energy emission in black holes during the low/hard state

Figure 5.5 (Krimm et al., 2006) shows the evolution of the outburst observed with *SWIFT/BAT* and *RXTE/ASM* in the 15–50 keV and 2–12 keV energy ranges, respectively. The observation of epoch 1 occurred close to the maximum of the peak in the outburst near December 18 (MJD 54 087.04). This was the brightest peak of the outburst since 2004 November, after the two previous and fainter episodes occurring in 2005 April and from 2006 January to April. The source was in a low/hard state and we observe a very strong signal up to 300 keV (detection level of $3\sigma$). The high-energy emission during the low/hard state observed is best described by reflection in a disk (Magdziarz & Zdziarski, 1995) of a cut-off powerlaw distribution of incident photons. The powerlaw distribution shows a folding energy at $E_f = 66 \pm 2$ keV. This reflection component disappears in epoch 2, while it returns in epoch 3. The origin for the cut-off in the powerlaw of epoch 1 has been usually understood as sign of an underlying corona with (inverse) Comptonizing electrons distributed thermally. However, in fits with EQPAIR model (Coppi , 1999), as shown in Section 5.3.2, this cut-off can be well reproduced by considering a non-thermal dominated distribution of (inverse) Comptonizing electrons, dominated by particles with low Lorentz factors ($\Gamma = 1.3$). Low values for the Lorentz factor ($\Gamma < 1.4$ in radio) are expected for the electrons consituting the corona being the base of a jet during the low/hard state, from radio observations (Fender et al., 2004). Our finding contrasts with that of Joinet et al. (2006). They found that a hybrid thermal dominated model was the best one for describing GX 339–4 in the low/hard state during the 2004 outburst, with the presence of a cut-off around $200 - 300$ keV. However, their combined spectrum spands data from several INTEGRAL revolutions (from 166 to 175) and spectral evolution could occur.

From our fits with EQPAIR model we obtain a value for the low/hard state of the coronal compactness very high (i.e. $l_h/l_s = 13.0 \pm 0.8$) compared to what is usually found in the low/hard state ($l_h/l_s = 4 - 8$; Wilms et al. 2006; Ibragimov et al. 2005). This would imply that the source of the high-energy emission is more compact than the source of the soft photons (namely the disk). This scenario would be consistent with the high-energy emission coming from the base of a jet, as previously considered in theoretical studies

by Fabian et al. (1982) and Miyamoto et al. (1991b). Markoff et al. (2005) suggested an alternative scenario, invoking that synchrotron self Comptonization occurring at the base of a jet would be responsible of the X-ray and $\gamma$-ray emission, thus connecting with the radio emission detected in the low/hard state. They interpreted the curvature seen in the spectrum during the low/hard state (specifically, a hardening above 10 keV, usually understood as a reflection hump) not as being due to reflection, rather being caused by self-synchrotron Comptonization from the base of a jet. However, this picture lacks of being inclination dependent. We propose in this Chapter that pure (inverse) Comptonization from low-relativistic and non-thermal dominated population of particles are the responsible for the high energy emission observed at E $>$ 10 keV during the low/hard state. Thus, reflection is not the main process responsible for the high energy emission observed in black holes. However, for some systems it is known the lack of such spectral features (no spectral humps or hardening a above 10 keV). For XTE J1118+480, the lack of any discernible break or hardening near 10 keV was used to argue for the lack of reflection component (Miller et al. 2002b). GRO J1655−40, another black hole transient system with low inclination orbit (as XTE J1118+480; both having jet line emission almost perpendicular to our line of sight) is another system which lacks of high energy spectral features (Díaz Trigo et al. 2007; Caballero-García et al. 2007a). Although low reflection covering factors are expected to be small if the hard energy emission comes from the base of a jet, this is not the only explanation of the spectral features found in the fits for GRO J1655–40 by Caballero-García et al. (2007a). We propose that, because particles responsible for the high energy emission are non-thermal and relativistic, high energy emission resulting from (inverse) Comptonization with these particles is highly anisotropic, then being dependent of the jet inclination of the system. Beloborodov et al. (1999), Malzac et al. (2001) proposed beaming effects for the high-energy emission in these conditions for the Comptonizing plasma (in the direction of the plasma velocity). GX 339–4 is a low-inclination system (with the jet pointing in the direction of our line of sight) and high-energy emission would point directly to us (contrary to the case of GRO J1655–40).

### 5.4.3 Evolution of softer states and plasma ejection events

Summarizing, the spectral evolution in the first three epochs reveals very interesting behavior of both the soft (E $<$ 20 keV) and hard (E$\gtrsim$20 keV) X-ray emission. GX 339–4 underwent a state transition from a pure low/hard state to a softer one (likely evolving through different soft intermediate states). In comparison to what was observed in 2002 (Gallo et al. 2004; Fender et al. 2004) we would have expected several radio flares to be triggered by the transitions (from low/hard to softer in epochs 1 and 2 and between soft intermediate states in epochs 2 and 3). Corbel et al. (2007) reported radio activity in the form of plasma ejection events coinciding with our transition observed from epochs 1

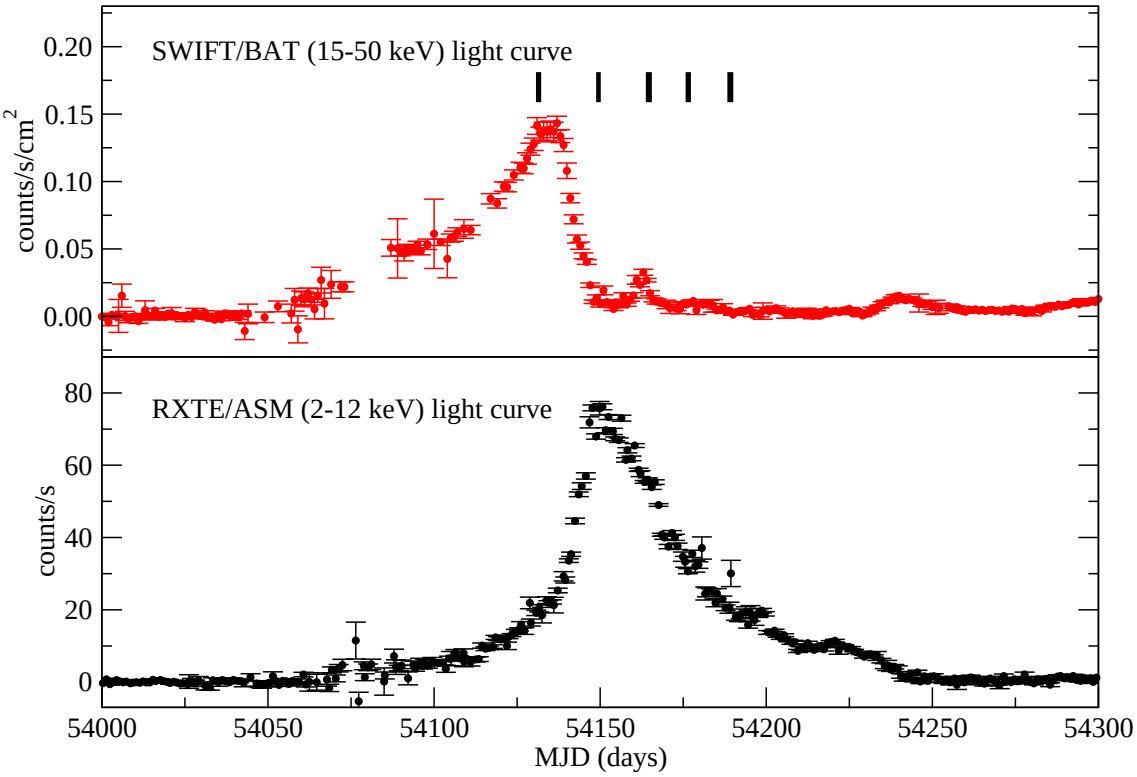


**Figure 5.5**: Swift/BAT and RXTE/ASM daily light curves of GX 339–4 during the overall outburst in 2007 (red and black dotted lines, respectively), illustrating the spectral evolution between the different states. Intervals of time in which the INTEGRAL observations were undertaken are also shown (black lines).

to 2. This state transition is accompanied by the change of the spectral shape in epoch 3. Belloni et al. (2006) noticed a spectral transition of the high-energy emission of GX 339–4 in the form of a disappearance of a high-energy cut-off at $72^{+10}_{-6}$ keV. Their observations were made using both RXTE and INTEGRAL during a fast state transition ($< 10$ h) occuring in 2004 from hard to soft intermediate states. This situation resembles that of our observations of epochs 2 and 3 using *XMM-Newton* and *INTEGRAL* data (although with inverted order). As we reported in Section 5.3, we do find a cut-off in the spectrum of epoch 1 at 66±2 keV, thus very close to the value reported by Belloni et al. (2006). However, due to the low signal of the spectrum in epoch 3 at high energies, we could not point out the presence of a clear cut-off in epoch 3. Nevertheless, the spectrum of epoch 3 is well described taking into account reflection and a skewed Fe K$_\alpha$ line, as in epoch 1, thus pointing out a common origin for the high energy emission. It seems that the source of the high energy emission (i.e. the base of the jet), reappeared during our observation

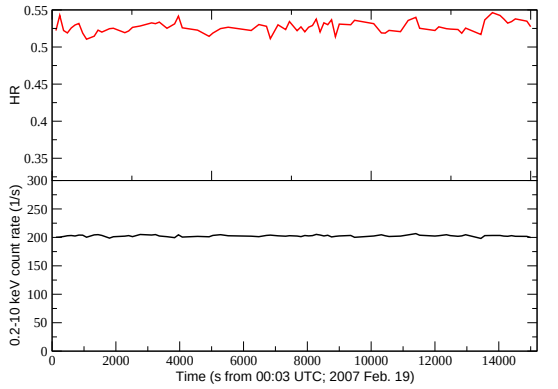


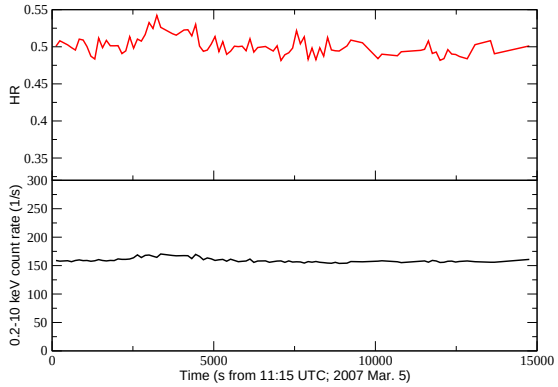


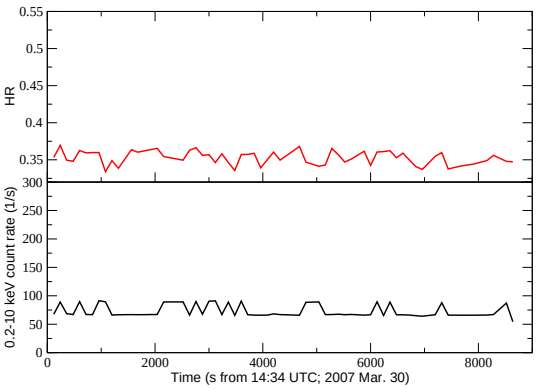


**Figure 5.6**: *Upper panels:* hardness ratio (counts in the 2.0–10 keV band divided by those between 0.2–2 keV) for epochs 2, 3 and 5. The binning is 120 s for all panels.*Lower panels:* 0.2-10 keV EPIC pn background subtracted light curve of GX 339–4 for epochs 2 (upper-left panel), 3 (upper-right panel) and 5 (bottom panel).

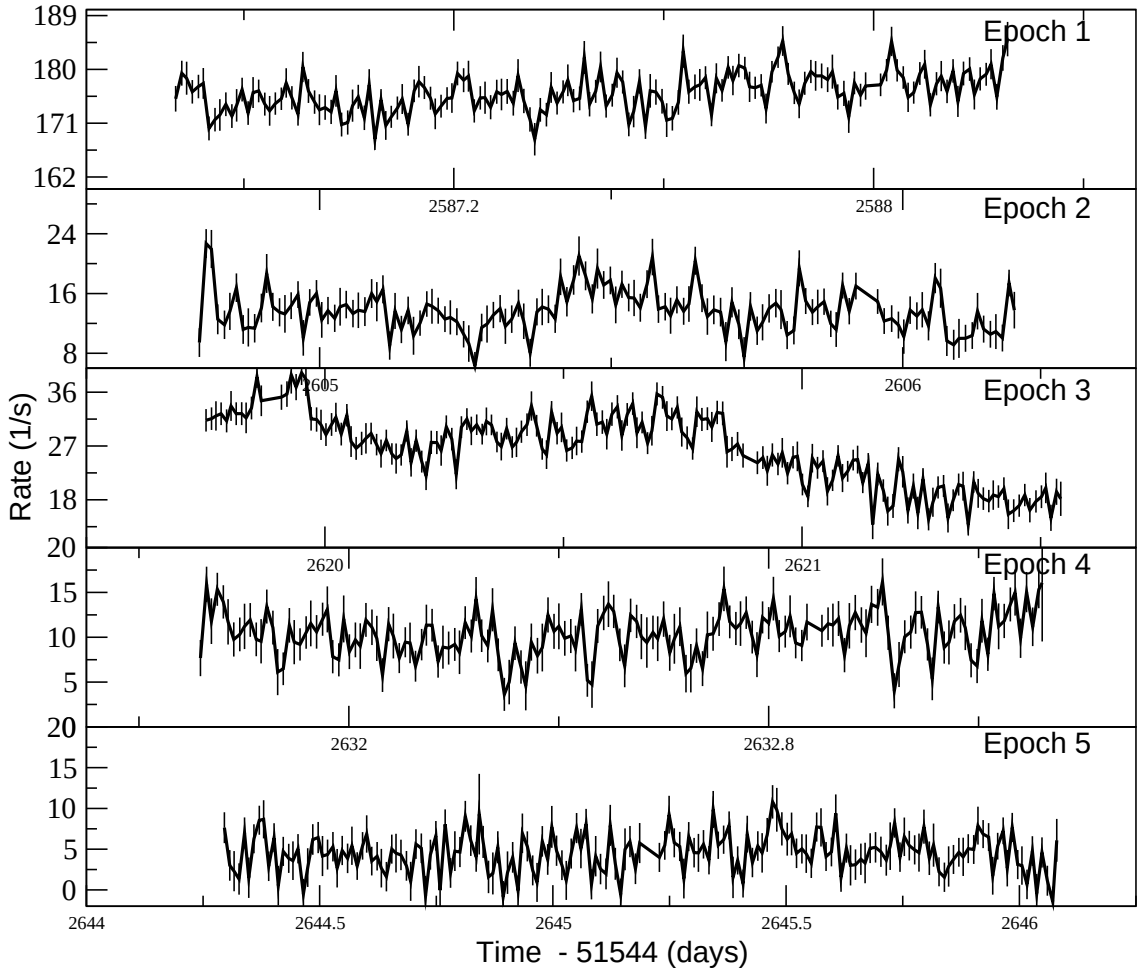


**Figure 5.7**: ISGRI/INTEGRAL (20-200 keV) light curve during all the observations (from Epoch 1 to 5). The binning is 1 000 s for all panels.

of epoch 3 and was quenched during epoch 2. Belloni et al. (2006) also noticed softening of the disk black body emission as occurring in our epoch 2. This behavior could in principle be understood as a sudden increase of accretion rate in epoch 3. Nevertheless, the existence of anticorrelations between hard and soft X-rays and between flux and hardness show that the spectral variability cannot be due to simple variability of absorption with an underlying intrinsic spectrum of constant shape and strength. One possibility is that the high-energy source was undertaking sudden changes and could be understood as a series of plasma ejection events in the softer states. This scenario was proposed earlier by Rodriguez et al. 2003, 2006, 2007 for similar spectral behavior ocurring in XTE J1550–564 and GRS 1915+105 and interpreted as ejection of material from the corona. However, our

detection of a skewed Fe $K_\alpha$ line during epoch 3 would indicate the presence of the primary high energy radiation originating close to the black hole. Moreover, in the low/hard state, the hard-energy emission spectrum is consistent with high-energy emission coming from a steady long-extended jet structure rather than a corona. This kind of high-energy emission would be strongly beamed (in the direction of the plasma velocity) and could explain the reason of not being observed for high-inclination systems, such as GRO J1655−40 (see Caballero-García et al. 2007a). Eventually, the very soft spectrum of epoch 5 is consistent with a transition to a very soft intermediate state as those observed previously for other systems (e.g. Cyg X–3; Beckmann et al. 2007) and would indicate that the source of the high energy emission is being diluted.

## 5.5 Conclusions

In this Chapter we studied the high-energy emission from GX 339–4 undergoing spectral changes from the low/hard state to softer intermediate states. During the low/hard state, high energy emission was detected up to ≈300 keV with spectral signatures (spectral cut-off at 66±2 keV) that allowed us to give insights into the high-energy emission processes occurring in GX 339–4 during the low/hard state:

- reflection is not the main process responsible for the high energy emission observed in black holes,
- this cut-off can be well reproduced by considering a non-thermal dominated distribution of (inverse) Comptonizing electrons, dominated by particles with low Lorentz factors ($\Gamma = 1.3$),
- the coronal compactness found is very high ($l_h/l_s = 13.0 \pm 0.8$), meaning that (inverse) Comptonizing electrons are distributed in a very compact corona, may be the base of a jet and
- high energy emission resulting from (inverse) Comptonization with these particles is highly anisotropic, then being dependent of the jet inclination.

All these characteristics point out to the high-energy emission from the base of an jet during the low/hard state.

During the soft intermediate states spectral evolution occurred in the form of an appearing/disappearing of both the reflection component and skewed Fe $K_\alpha$ line plus gradual softening of the source to a very soft intermediate state. These issues allowed us to give insights into the high-energy emission processes occurring in GX 339–4 during the soft intermediate states:

- high-energy source was undertaking sudden changes and could be understood as a series of plasma ejection events very close to the black hole in the soft intermediate states and
- the very soft spectrum of last epoch would be constistent with the source of the high energy emission (the base of the jet) being more diluted.

# Chapter 6

# General conclusions and future work

## 6.1 General conclusions

In this thesis we use the spectral capabilities of the INTEGRAL satellite and the photometric capabilities of its OMC camera for the study of two kind of celestial objects emitting in X-rays. INTEGRAL provides high-energy spectroscopy from X-rays to $\gamma$-rays (covering an spectral energy range of $E = 3 - 8\,000$ keV) and OMC is a CCD camera operating in the Johnson V band, capable of providing continuous monitoring of the scientific targets included in the *OMC Input Catalogue*. The spectral capabilities of *INTEGRAL* have allowed to study the high-energy emission from two black hole transients (i.e. GRO J1655–40 and GX 339–4) and have provided new insights into the physics of the high energy emission (X-rays and $\gamma$-rays) of this kind of objects. OMC, the optical monitor on-board INTEGRAL, has allowed us to perform a multi-wavelength analysis of TYC 2675- 663-1, revealing that it is a binary system with properties dominated by accretion. While the black hole transients studied in this thesis correspond to dedicated observations from an observer accepted program, TYC 2675- 663-1 was studied as part of an OMC serendipitious program.

We describe the process of compilation of sources of scientific interest included in the *OMC Input Catalogue*, constituted by $\gtrsim$541 000 sources. The sources with high-energy emission have higher priority to be observed than the remainder and this allowed us to obtain continuous photometry for TYC 2675- 663-1. TYC 2675- 663-1 is the optical counterpart of 1RXS J200912.0+323344 and both its photometric and spectral properties are typical of a binary system with properties controlled by accretion. Moreover, we have discovered that TYC 237 363 1, HD 86222, TYC 1306 -153 -1 and TYC 2674 -5404 -1 are the optical counterparts of 1RXS J095156.0+004722, 1RXS J095706.3-012019,

1RXS J054101.8+203624 and 1RXS J200219.0+333912 as well. The two former are binary systems as well and the X-ray emission is of that expected for highly rotating stars and due to chromospheric activity.

For TYC 2675- 663-1 the situation is different and an X-ray excess of ≈50% have been detected. We have performed both photometric and spectroscopic campaigns with observatories on-ground to unveil the origin of the X-ray excess and the nature of the components of the binary system as well. This has resulted in the discovery of a strong O-Connell effect, erratic behaviour in the form of flares and asymmetrical minima plus different maxima depths in the light curve. The spectroscopy has allowed us to detect strong and broad $H_\alpha$ and He I in emission, with P Cygni profile, due to accretion processes in the binary system. All these properties point out to this system being candidate of Algol system undergoing drastic changes, may be becoming a cataclysimic variable in the future. Eventually, X-ray activity in the form of flares is expected to appear in this system.

High-energy emission from black holes is still a matter of debate. With the study of GRO J1655–40 and GX 339–4 we present new evidence that hard X-ray emission in the low/hard state may not be dominated by thermal Comptonization. We present an alternative scenario for the origin of the high energy emission that is well suited to explain the high energy emission from GRO J1655–40 and GX 339–4. The great sensitivity of INTEGRAL has allowed us to detect the high-energy emission from these black hole candidates during the low/hard state in short time intervals. This issue is very important because state evolution is important for this kind of systems.

With GRO J1655-40 we have realized of an high-energy powerlaw emission (with the lack of any exponential cut-off), which would mean that thermal processes do not play an important role in the high-energy emission from this kind of objects during the low/hard state. Thermal Comptonization was thought to be the source of the high-energy emission in the low/hard state during for last 30 years. Instead, our finding would be consistent with the high-energy emission coming from (inverse) Comptonization by the non-thermal particles (leptons) at the base of a jet.

For GX 339–4 the situation a priori seems to be totally different for that of the GRO J1655–40. GX 339–4 shows a high-energy power-law emission with an exponential cut-off at 66±2 keV during the low/hard state. However, this exponential cut-off is due to the dominance of low-relativistic particles responsible for the (inverse) Comptonization of photons from the disk. With this finding, the connection between radio and hard X-ray emission seems to be close to the end, since it is known that radio emission during the low/hard state comes from the low/relativistic particles at the base of a jet.

State transitions have also been detected to occur within our INTEGRAL observations in short periods of time (days). Reflection and relativistic Fe $K_\alpha$ line [1], are

[1] both being aspects of the fluorescence of the high-energy emission by the inner regions of the disc.

found to be correlated with the spectral hardness. This would indicate fluctuation of the high-energy primary source. Fluctuations of the high-energy source have been detected previously, but not correlated with appearance/disappearance of the relativistic Fe $K_\alpha$ line.

The different orbital inclination of the binary systems GRO J1655–40 (almost edge-on) and GX 339–4 (almost face-on) gives very different high-energy spectral characteristics. First and foremost, the cut-offed powerlaw is a good description only for GX 339–4 (the face-on system). Moreover, the relativistic Fe $K_\alpha$ line and reflection are found to be null in the case of GRO J1655–40, while for GX 339–4 these are clearly detected during the soft intermediate state. This would be a consequence of the high-energy radiation being highly collimated in the direction of a stream perpendicular to the disc.

Overall, our findings would mean that the previous scenario proposed for the origin of the high-energy emission in black hole transients is not due to (inverse) thermal Comptonization by the electrons of a corona that fills the inner region of the disc (as proposed in the ADAF scenario). Non-thermal (inverse) Comptonization (by low relativistic particles in the low/hard state) in a compact corona seems to be a better description to the data. This would imply that relativistic effects from the base of a jet should have to be taken into account in the high-energy emission of black holes.

## 6.2 Trabajo futuro

Los resultados de este trabajo proporcionan nuevos datos para entender la física de los procesos de emisión en alta energía de los agujeros negros. También dan lugar a nuevos interrogantes (algunos con carácter general y otros más específicos) relacionados con este marco. Mi trabajo futuro consistirá en la extensión del mismo estudio presentado en esta tesis pero ampliándolo a una muestra más amplia de agujeros negros (tanto galácticos como extragalácticos) y utilizando datos de otros satélites, tanto en rayos X como $\gamma$ (*XMM-Newton*, *CHANDRA*, *Suzaku*, *INTEGRAL*, *GLAST*...). En lo siguiente detallo mi plan de trabajo futuro en cuanto a continuación de la explotación de los datos a obtener con el satélite *INTEGRAL*.

### 6.2.1 Probando los estados de los agujeros negros

Las binarias de rayos X con agujero negro presentan diferentes modos de variabilidad correlacionada en un rango multi-longitud de onda durante sus períodos de erupción, denominados *estados*. El conocimiento preciso de los estados puede proporcionar una cantidad significativa de información, i.e.: la naturaleza de los procesos de emisión a alta energía en los agujeros negros y su eficiencia asociada, la fracción de energía acretada y canalizada en radiación frente a la luminosidad mecánica (i.e. *jets*), y la naturaleza de los

diferentes tipos de AGNs observados (e.g. *radio quiet* frente a *radio loud*). Observaciones ya realizadas en multi-longitud de onda han dado ya valiosas pistas. Una expectativa muy simple – la de que el radio interno del disco (o los cambios en el mismo) podrían dar lugar a la transición entre estados y a la actividad de los *jets* – ahora parece ser una visión incorrecta. A lo largo de las transiciones entre estados el radio interno del disco parece no cambiar apreciablemente. Sin embargo, una relación muy sólida parece haber emergido como resultado de otros trabajos: la emisión en rayos X y la emisión en radio procedente del *jet* está estrechamente correlacionada. Esta conexión, denominada conexión *jet*-disco, es indirecta – las correlaciones flujo-flujo observadas las muestran sólo en el espectro más duro. La corona, fuente emisora de rayos X duros, podría jugar un papel importante en la definición de estados y las propiedades de los *jets*, por lo que *INTEGRAL* podría dar valiosas pistas al respecto.

Las definiciones de los estados están tomadas de observaciones en rayos X blandos. En orden de ritmo de acreción de masa creciente, los estados pueden ser: *low/hard*, *intermediate*, *high/soft* y *very/high*. La misma secuencia ha sido también definida como: *jet* activa, *intermediate*, *thermal-dominant* y *steep power law*, basada en ambos casos en propiedades en radio y en rayos X. **La situación en rayos X duros es muy diferente**. En un examen de varias observaciones hecho con el satélite *CGRO* por Grove et al. (1998), se identificaron sólo dos estados en rayos X duros: cuando el disco de acreción no está claramente detectado en rayos X blandos, una ley de potencias contínua y sin cortes exponenciales es la que mejor describe el espectro en rayos $\gamma$/rayos X duros; éste es el denominado estado *broken* en rayos $\gamma$. Cuando aparece una componente procedente del disco de acreción que domina el espectro en rayos X blandos, entonces la ley de potencias parece extenderse hasta los 200 keV sin ningún corte exponencial; éste es el denominado estado *powerlaw* en rayos $\gamma$.

*Cómo se conectan los estados en rayos $\gamma$ con los estados en rayos X blandos, y si realmente hay o no dos estados en rayos $\gamma$ han sido las cuestiones centrales en nuestro trabajo de investigación.* Nuestras observaciones con *INTEGRAL* muestran que hay una complejidad adicional a esta interpretación, y sugieren que estados en rayos $\gamma$ no se corresponden de forma unívoca a los estados en rayos X. El estado en rayos $\gamma$ *broken* no es simplemente el estado *low/hard* en rayos X y el estado *powerlaw* en rayos $\gamma$ no es meramente el estado *high/soft* en rayos X. Hemos hallado una simple y sin cortes exponenciales ley de potencias como la mejor descripción del espectro de GRO J1655–40 en el estado *low/hard*, cuando la componente de un disco de acreción no pudo ser detectada. También hemos hallado que los cortes exponenciales (i.e. *cut-offs*) aparecen y desaparecen durante el estado *high/soft*: a veces la ley de potencias es simple y a veces es más compleja, tal y como vimos en las observaciones de GX 339–4. Claramente, nuestro programa está proporcionando valiosas pistas en nuestra visión de los estados de los agujeros negros. A

la hora de ir más allá y no sólamente darnos cuenta de los nuevos comportamientos y complejas relaciones entre los estados en rayos X y $\gamma$ y para entender los estados como cambios en la geometría de los procesos de acreción, son necesarias más observaciones para construir una representación más convincente y completa.

### 6.2.2 Comptonización o emisión por un *jet*?

La reflexión en rayos X es un proceso que resulta cuando una fuente de rayos X duros ilumina una distribución de gas ópticamente gruesa y relativamente fría (George & Fabian, 1991). En los BHCs y AGNs, los rayos X duros iluminan el disco, creando un espectro característico que consiste en una línea Fe $K_\alpha$ de emisión, y un contínuo de reflexión que (relativo a la ley de potencias) aparece como un decremento en el flujo en el rango 10–20 keV y un exceso en el flujo con un máximo en torno a 30 keV (el denominado *reflection hump*, debido a una re-dispersión Compton). La naturaleza del espectro reflejado nos permite desvelar la intensidad del flujo en rayos X duros que ilumina el disco de acreción y un cierto número de parámetros importantes, incluyendo la extensión radial del borde interno del disco, la inclinación del disco interno y su estado de ionización.

La reflexión por el disco es una herramienta incisiva para distinguir si la región de emisión de rayos X duros es una corona Comptonizadora o un *jet* compacto en rayos X y si el mecanismo y la región de emisión de rayos X duros cambian estado tras estado. A la hora de producir el bajo nivel de radiación de la emisión dura en rayos X en el estado *low/hard*, factores de Lorentz del orden $\gamma = 2 - 3$ son requeridos para la base del *jet* (Markoff et al., 2001). Esto tiene el efecto de focalizar la emisión en rayos X en un cono con un ángulo de apertura $\theta \propto 1/\gamma$, y la emisión dentro del cono queda potenciada por un factor $\gamma^3$. Para $\gamma = 2 - 3$, la radiación estaría colimada fuera del disco en torno a 8–27 veces como máximo, al contrario de lo que se esperaría si iluminara el disco la emisión por una distribución isotrópica de una corona Comptonizadora emisora. La intensidad del espectro reflejado entonces sirve como un test directo para averiguar la naturaleza de la región emisora en rayos X. Si los *jets* son los responsables de la emisión en rayos X duros, fracciones muy pequeñas de $F_{refl}/F_{total}$ serían observables. La elevada sensibilidad de *INTEGRAL* a 30 keV relativa a *RXTE* hace del primero el mejor instrumento para medir el contínuo reflejado y la naturaleza de la emisión en rayos X duros y rayos $\gamma$ blandos en las BHCs.

Los mecanismos de emisión en rayos X duros y rayos $\gamma$ blandos podrían no ser los mismos en cada estado en rayos X y en rayos $\gamma$. Observaciones con *INTEGRAL* son esenciales a la hora de determinar si éste es el caso. En general, la reflexión es más intensa en el estado *Very High* en rayos X, sólo ligeramente más débil en el estado *intermediate*, pero tanto como 3–4 veces más débil en el estado *low/hard*. Esto podría implicar que *diferentes estructuras iluminan el disco en estos estados*. Para confirmar esto, sin embargo,

se necesita apurar la sensibilidad de *INTEGRAL* hasta varios centenares de keV. Una corona Comptonizadora se espera que produzca un corte exponencial del espectro en torno a la temperatura cinética de los electrones ($E_{break} \approx kT_e$). Cortes exponenciales en torno a 150–200 keV no son estadísticamente significativas en las observaciones con *BeppoSAX* y *RXTE*. Más dramáticamente incluso, *a energías entre 0.5–1 MeV, la emisión sincrotrón de un jet se espera sea menospreciable debido a enfriamiento sincrotrón, mientras que un híbrido de Comptonización térmica y no térmica podría permanecer sin cambios incluso hasta energías mayores.*

Finalmente, ahora está claro que los modelos para las transiciones entre estados basados sólo en $\dot{m}$ no pueden ser correctos: estados dominados por un disco y estados más duros (coronales o dominados por un *jet*?) se han visto en un rango amplio de $\dot{m}$. Al menos dos factores deben dirigir las transiciones entre estados; siendo el segundo de ellos, e.g., la compacidad de la corona. Modelos como el EQPAIR incluyen la compacidad de la corona como parámetro de ajuste, pero dependen del hecho de tener una elevada sensibilidad hasta varios centenares de keV.

### 6.2.3 La línea de aniquilación

Aunque tanto las regiones de Comptonización como los *jets* están muy probablemente constituídos por electrones y protones, podría haber también una población de positrones. La intensidad de la línea de aniquilación electron-positrón a 511 keV, y/o su característica dispersora en torno a ≈170 keV, podrían dar valiosas pistas acerca de la densidad y la temperatura en tales volúmenes. La línea de aniquilación podría formarse muy cerca del agujero negro, y podría poner a prueba las condiciones de relatividad general en dicho ambiente. Alternativamente, también se ha propuesto que las líneas de aniquilación podrían estar producidas lejos del agujero negro, en los flujos de los *jets* (Kaiser & Hannikainen, 2002). De hecho, líneas de aniquilación podrían haber sido también detectadas en otros sistemas como Nova Muscae 1991 y 1E 1740.7–2942 (Churazov et al. (1993); Cordier et al. (1993)). Estas detecciones son muy controvertidas dado que no fueron detectadas por *BATSE* ni *OSSE* (Smith et al., 1996). Complementando nuestras observaciones de *INTEGRAL* con las de otras observaciones simultáneas en radio, estaríamos en condiciones de ver si la línea de emisión está ligada a la emisión en radio (ésta última ligada a la emisión de un *jet*).

# Lista de publicaciones

El trabajo presentado en esta tesis ha dado lugar a las siguientes publicaciones en revistas internacionales y contribuciones a congresos:

Artículos en revistas con árbitro

- "*INTEGRAL and XMM-Newton observations of GX 339–4 during hard, soft and intermediate states in the 2007 outburst* " **M. D. Caballero-García**; J. M. Miller; M. Díaz Trigo; E. Kuulkers; A. C. Fabian; J. M. Mas-Hesse; D. Steeghs; M. van der Klis 2008, Submitted to the Astrophysical Journal.

- "*TYC 2675- 663-1: a newly discovered accreting binary star system*" **M. D. Caballero-García**; G. Torres; B. Montesinos; I. Ribas; A. Domingo; D. Rísquez; J. M. Mas-Hesse; E. Solano; A. Giménez 2008, Submitted to Astronomy and Astrophysics.

- "*Cygnus X-3 transition from the ultrasoft to the hard state* " V. Beckmann; S. Soldi; G. Belanger; S. Brandt; **M. D. Caballero-Garcia**; G. De Cesare; N. Gehrels; S. Grebenev; O. Vilhu; A. von Kienlin; T.J.-L. Courvoisier; 2007, Astronomy and Astrophysics, 473, 903

- "*The high energy emission of GRO J1655-40 as revealed with INTEGRAL spectroscopy of the 2005 outburst* " **M. D. Caballero-García**; J. M. Miller; E. Kuulkers; M. Díaz Trigo; J. Homan; W. H. G. Lewin; P. Kretschmar; A. Domingo; J. M. Mas-Hesse; R. Wijnands; A. C. Fabian; R. P. Fender; M. van der Klis, 2007, The Astrophysical Journal, 669, 534

- "*XMM-Newton and INTEGRAL spectroscopy of the microquasar GRO J1655-40 during its 2005 outburst* " M. Díaz Trigo; A. N. Parmar; J. Miller; E. Kuulkers; **M. D. Caballero-García**; 2006, Astronomy and Astrophysics, 462, 657

- "*The Input Catalogue for the OMC camera on-board INTEGRAL* " Domingo, A.; **Caballero, M. D.**; Figueras, F.; Jordi, C.; Torra, J.; Mas-Hesse, J. M.; Giménez, A.; Hudcova, V.; Hudec, R. ; 2003, Astronomy and Astrophysics, 411, L281

- "*OMC: An Optical Monitoring Camera for INTEGRAL. Instrument description and performance* " J.M. Mas-Hesse; A. Giménez; L. Culhane; C. Jamar; B. McBreen; J. Torra; R. Hudec; J. Fabregat; E. Meurs; M.A. Alcacera; A. Balado; R. Beiztegui; T. Belenguer; L. Bradley; **M.D. Caballero**; P. Cabo; J.M. Defise; E. Díaz; A. Domingo; F. Figueras; I. Figueroa; L. Hanlon; F. Hroch; V. Hudcova; T. García; B. Jordan; P. Kretschmar; C. Laviada; M. March; E. Martín; E. Mazy; M. Menéndez; J.M. Mi; E. de Miguel; T. Muñoz; K. Nolan; J. Polcar; R. Olmedo; M. Reina; A.

Sánchez; J.C. San Martín; A. Smith; J. Soldan; J.P. Swings; P. Thomas; V. Timón; and D. Walton; 2003, Astronomy and Astrophysics, 411, L261

Contribuciones a congresos y/o publicadas en libros

- "*XMM-Newton and INTEGRAL spectroscopy of GRO J1655-40 during its 2005 outburst*" M. Díaz Trigo; A. N., Parmar; J. M. Miller; E. Kuulkers; **M. D. Caballero-García**; American Institute of Physics Conference Series, 924, 877D, 2007

- "*The high energy emission from black holes* "**M. D. Caballero-García**; J. M. Miller; E. Kuulkers on behalf of a large collaboration team
  X-rays from Nearby Galaxies, Madrid (Spain). September 2007. Talk.
  MPE report, astro-ph/0711.0844

- "*A deep view into the black holes high energy emission*" **M. D. Caballero-García**; J. M. Miller; E. Kuulkers; M. Díaz Trigo
  XMM-Newton: The Next Decade. Madrid (Spain), June 2007, Poster.

- "*ToO observations of GRO J1655-40 during outburst* "**M. D. Caballero-García**; E. Kuulkers; P. Kretschmar; A. Domingo; J. M. Miller and J. M. Mas-Hesse
  The 6th INTEGRAL Workshop: the obscured Universe. Moscow (Russia), July 2006, Poster
  December 2006 as Special Publication SP-622; astro-ph/0609491

- "*INTEGRAL/OMC: optical counterparts of ROSAT sources* "**M. D. Caballero-García**; A. Domingo; D. Rísquez and J. M. Mas-Hesse
  The X-ray Universe 2005. El Escorial (Spain), September 2005. Poster
  Proceedings of The X-ray Universe 2005. ESA SP-604, January 2006.

- "*OMC-INTEGRAL: optical observations of X-ray binaries* " **M.D. Caballero**; A. Domingo; D. Rísquez; J. M. Mas-Hesse; A. Giménez; F. Figueras and C. Jordi
  Joint European and National Astronomical Meeting (JENAM). Granada (Spain), September 2004. Talk
  The many scales in the universe. JENAM 2004 Astrophysics Reviews. Ed.: Springer

- "*OMC: The Optical Monitoring Camera onboard INTEGRAL*" J.M. Mas-Hesse; A. Giménez; J.L. Culhane; C. Jamar; B. McBreen; J. Torra; R. Hudec; J. Fabregat; E. Meurs; J.P. Swings; A. Domingo; E. Díaz; E. de Miguel; P. Cabo; **M.D. Caballero**; D. Rísquez
  Joint European and National Astronomical Meeting (JENAM). Granada (Spain), September 2004. Poster
  The many scales in the universe. JENAM 2004 Astrophysics Reviews. Ed.: Springer

- "*Optically variable sources monitored by the OMC*" A. Domingo; D. Rísquez; **M.D. Caballero**; J.M. Mas-Hesse; A. Giménez; R. Gutiérrez; E. Solano; L. Sarro
  Joint European and National Astronomical Meeting (JENAM). Granada (Spain), September 2004. Poster
  The many scales in the universe. JENAM 2004 Astrophysics Reviews. Ed.: Springer

- "*OMC: An optical monitoring camera for INTEGRAL*" J.M. Mas-Hesse; A. Giménez; J.L. Culhane; C. Jamar; B. McBreen; J. Torra; R. Hudec; J. Fabregat; E. Meurs; J.P. Swings; A. Domingo; **M.D. Caballero**; D. Rísquez
  The 5th INTEGRAL Workshop: The Integral Universe. Munich (Germany), February 2004. Co-author talk
  Proceedings of The 5th INTEGRAL Workshop: The Integral Universe. ESA SP-552

- "*Optically variable sources monitored by the OMC*" A. Domingo; D. Rísquez; **M.D. Caballero**; J.M. Mas-Hesse; A. Giménez; R. Gutiérrez; E. Solano; L. Sarro
  The 5th INTEGRAL Workshop: The Integral Universe. Munich (Germany), February 2004. Poster
  Proceedings of The 5th INTEGRAL Workshop: The Integral Universe. ESA SP-552

- "*OMC-INTEGRAL: optical observations of X-ray sources*" **M. D. Caballero**; A. Domingo; D. Rísquez; J. M. Mas-Hesse; A. Giménez; F. Figueras and C. Jordi
  The 5th INTEGRAL Workshop: The Integral Universe. Munich (Germany), February 2004. Poster
  Proceedings of The 5th INTEGRAL Workshop: The Integral Universe. ESA SP-552

- "*The Input Catalogue for the OMC camera on-board INTEGRAL*" A. Domingo; F. Figueras; J.M. Mas-Hesse; J. Torra; C. Jordi; **M.D. Caballero**
  Quinta reunión científica de la Sociedad Española de Astronomía (SEA). Toledo, September, 2002. Poster
  Highlights of Spanish Astrophysics III, ISBN 1-4020-1388-4, p. 470. Year 2003

## Otras publicaciones

Telegramas asronómicos

- "*INTEGRAL Campaign on GX 339-4* " J. M. Miller; E. Kuulkers; **M.D. Caballero-García**; M. Díaz Trigo; 2007, ATeL, 980

- "*INTEGRAL TOO observations of GX 339-4* " S. Soldi; J. Miller, E. Kuulkers, **M.D. Caballero-García**, M. Díaz Trigo, on behalf of a larger collaboration; 2007, ATeL, 986

- "*IGR J16558-4150: a new hard X-ray transient detected by INTEGRAL* " S. Soldi, S. Shaw, J. Miller, E. Kuulkers, **M.D. Caballero-García**, M. Díaz Trigo, on behalf of a larger collaboration; 2007, ATeL, 987

- "*INTEGRAL observations of GX339-4: preliminary spectral fit results* " **M.D. Caballero-García**, J. Miller, E. Kuulkers, M. Díaz Trigo, on behalf of a larger collaboration; 2007, ATeL, 1000

- "*INTEGRAL observations of GX339-4: preliminary spectral fit results* " **M.D. Caballero-García**, J. Miller, E. Kuulkers, M. Díaz Trigo, on behalf of a larger collaboration; 2007, ATeL, 1012

- "*INTEGRAL observations of GX339-4: preliminary spectral fit results* " **M.D. Caballero-García**, J. Miller, E. Kuulkers, M. Díaz Trigo, on behalf of a larger collaboration; 2007, ATeL, 1029

- "*INTEGRAL observations of GX339-4: preliminary spectral fit results* " **M.D. Caballero-García**, J. Miller, E. Kuulkers, M. Díaz Trigo, on behalf of a larger collaboration; 2007, ATeL, 1032

- "*INTEGRAL observations of GX339-4: preliminary spectral fit results* " **M.D. Caballero-García**, J. Miller, E. Kuulkers, M. Díaz Trigo, on behalf of a larger collaboration; 2007, ATeL, 1050

# Bibliografía

Amado, P. J., 2003, A&A, 404, 631A

Applegate, J. H., 1992, ApJ, 385, 621

Arnaud, K. A., 1996, ADASS, 5, 17A

Austin, S. J., Robertson, J. W., Tycner, C., Campbell, T. & Honeycutt, R. K., 2007, AJ, 133, 1934

Bade, N., Engels, D., Voges, W., Beckmann, V., Boller, T., Cordis, L. et al., 1998, A&AS, 127, 145B

Bailyn, C. D., Orosz, J. A., Girard, T. M., Shardha, J., della Valle, M. et al., 1995, Nature, 374, 701

Bailyn, C. D., Orosz, J. A., McClintock, J. E. & Remillard, R. A., 1995, Nature, 378, 157

Bardeen, J. M., Press, W. H. & Teukolsky, S. A., 1972, ApJ, 178 ,347B

Beckmann, V., Soldi, S., Bélanger, G., Brandt, S., Caballero-García, M. D. et al., 2007, A&A, 473, 903

Belloni, T., Mendez, M., King, A. R., van der Klis, M. & van Paradijs, J., 1997, ApJ, 488L, 109B

Belloni, T., Méndez, M. & van der Klis, M., 1999, ApJ, 519L, 159B

Belloni, T., Homan, J., Casella, P. et al., 2005, A&A, 440, 207B

Beloborodov, A. M., 1999, ApJ, 510L, 123B

Belloni, T., Parolin, I., Del Santo, M., 2006, MNRAS, 367, 1113B

Bird, A. J., Malizia, A., Bazzano, A. et al., 2007, ApJS, 170, 175B

Boirin, L. & Parmar, A. N., 2003, A&A, 407, 1079B

Bothe, W. & Kolhörster, W., 1929, Zeitschrift für Physik 56, 751

Bouchet, L., Jourdain, E., Mandrou, P. et al., 1993, ApJ, 407, 739B

Brandt, W. N. & Schulz, N. S., 2000, ApJ, 544L, 123B

Brocksopp, C. , McGowan, K. E., Krimm, H., Godet, O., Roming, P., et al. 2006, MNRAS, 365, 1203B

Buxton, M. & Bailyn, C., 2005, ATel 485

Michelle Buxton, Charles Bailyn, Dipankar Maitra, 2005, ATel 418

Caballero-García, M. D., 2003, Master thesis, Universitat de Barcelona

Caballero, M. D., 2004, Proceedings to the "5th INTEGRAL Workshop on the INTEGRAL Universe", 2004, ESA Special Publication, eds.: Schoenfelder, V., and Lichti, G. & Winkler, C. vol. 552, p. 875

Caballero-García, M. D., Domingo, A., Rísquez, D. & Mas-Hesse, J. M., Proceedings to the "The X-ray Universe 2005", 2006, ed.: Wilson, A., vol. 604, p. 249

Caballero-García, M. D., Miller, J. M., Kuulkers, E., Diaz Trigo, M., Homan, J., Lewin, W. H. G., Kretschmar, P., Domingo, A., Mas-Hesse, J. M., Wijnands, R., Fabian, A. C., Fender, R. P., van der Klis, M., 2007, ApJ, 669, 534

Caballero-García, M. D., Miller, J. M., Kuulkers, E., et al. 2007, ATel 1000

Caballero-García, M. D., Miller, J. M., Kuulkers, E., et al. 2007, ATel 1012

Caballero-García, M. D., Miller, J. M., Kuulkers, E., et al. 2007, ATel 1029

Caballero-García, M. D., Miller, J. M., Kuulkers, E., et al. 2007, ATel 1032

Caballero-García, M. D., Miller, J. M., Kuulkers, E., et al. 2007, ATel 1050

Cadolle Bel, M., Sizun, P., Goldwurm, A., Rodriguez, J., Laurent, P., Zdziarski, A. A., 2006, A&A, 446, 591C

Corbel, S., Tzioumis, T., Brocksopp & Fenfer, R., P., 2007, ATel 1007

Chaty, S. & Filliatre, P., 2005, Ap&SS, 297, 235C

Chen, W., Shrader, C. R. & Livio, M., 1997, ApJ, 491, 312

Chernyakova, M., 2005, ISDC/OSA-UM-IBIS

Chernyakova, M., Kretschmar, P., JEM-X team, Neronov, A., 2005, ISDC/OSA-UM-JEMX

Churazov, E., Gilfanov, M., Sunyaev, R., Pavlinsky, M., Grebenev, S., Dyachkov, A. et al., 1993, ApJ, 407, 752C

Clemens, J. C., Reid, I. N., Gizis, J. E. & O'Brien, M. S., 1998, 496, 352C

Coppi, P. S., 2000, Bulletin of the American Astronomical Society, 32, 1217

Corbel, S., Fender, R., Tzioumis, A. K., et al., 2000, A&A, 359, 251

Corbel, S., Tzioumis, T., Brocksopp, C., Fender, R. P., 2007, ATel 1007

Cordier, B., Paul, J., Ballet, J., Goldwurm, A., Bouchet, L., Roques, J. P et al., 1993, A&A, 275L, 1C,

Costa, E., Frontera, F., Heise, J. et al., 1997, Natur, 387, 783C

Courvoisier, T. J.-L., Walter, R., Beckmann, V., et al., 2003, A&A, 411, L53

Cox, A. N., Allen's Astrophysical quantities, 2000, Springer

Csizmadia, S., Patkós, L., Moór, A. & Könyves, V., 2004, A&A, 417, 745

Cutri, R. M., Skrutskie, M. F., van Dyk, S., Beichman, C. A., Carpenter, J. M., Chester, T., et al., 2003, The IRSA 2MASS All-Sky Point Source Catalog, NASA/IPAC Infrared Science Archive.

Cruddace, R. G. & Dupree, A. K., 1984, ApJ, 1984, 277, 263

Deluit, S., (2005) SPI-NS-0-4307-CESR

Den Herder, J. W., Brinkman, A. C., Kahn, S. M., et al. 2001, A&A, 365, L7

Díaz Trigo, M., Parmar, A., N., Miller, J. M., Kuulkers, E., Caballero-García, 2007, A&A, 462, 657D

Dickey & Lockman, 1990, ARAA, 28, 215

Domingo, A., Caballero, M. D., Figueras, F., Jordi, C., Torra, J., Mas-Hesse, J. M., Giménez, A., Hudcova, V. & Hudec, R., 2003, A&A, 411L, 281D

Done, C., & Nayakshin, S., 2001, MNRAS 328, 616

Dove, J. B., Wilms, J., Begelman, M. C., 1997, ApJ, 487, 747

Downes, R. A., Webbink, R. F., Shara, M. M., Ritter, H., Kolb, U. & Duerbeck, H. W., 2001, PASP, 113, 764D

Dubath, P., Knödlseder, J., Skinner, G. K., Connell, P., Kreykenbohm, I., Strong, A., Sizun, P., Attié, D., Schanne, S., Cordier, B., Bouchet, L., & von Kienlin, A., 2005, MNRAS, 357, 420

Dupree, A. K., Avrett, E. H., Brickhouse, N. S., Cranmer, S. R. & Szalai, T., 2007, astro-ph/0702395

Ebisawa, K., 1991, PhD thesis, Univ. of Tokyo

Ebisawa, K., Ueda, Y., Done, C., 1993, AAS, 183, 5516E

Ebisawa, K., Titarchuk, L. & Chakrabarti, S. K., 1996, PASJ, 48, 59

Ebisawa, K., Bourban, G., Bodaghee, A., Mowlavi, N., & Courvoisier, T. J.-L., 2003, A&A, 411L, 59E

Esin, A. A., McClintock, J. E. & Narayan, R., 1997, ApJ, 489, 865

Esin, A. A., McClintock, J. E., Drake, J. J. et al., 2001, ApJ, 555, 483

Fabian, A. C., Guilbert, P. W., Motch, C., et al., 1982, A&A, 111L, 9F

Fabian, A. C., Rees, M. J., Stella, L., White, N. E., 1989, MNRAS, 238, 729

Fabian, A. C., Miniutti, G., Gallo, L. et al., 2004, MNRAS, 353, 1071F

Fabian, A. C., Miniutti, G., Iwasawa, K. et al., 2005, MNRAS, 361, 795F

Fender, R., Corbel, S., Tzioumis, T., et al. 1999, ApJ, 519L, 165F

Fender, R., 2001, MNRAS, 322, 31

Fender, R. P., Belloni, T. M. & Gallo, E., 2004, MNRAS, 355, 1105F

Fichtel, C. E., Hartman, R. C., Kniffen, D. A., Thompson, D. J., Ogelman, H. et al., 1975, ApJ, 198, 163F

Fichtel, C. E., Hartman, R. C., Hunter, S. D., et al., 1990, VizieR Online Data Catalog, ref. VII/130

Fichtel, C. E., Bertsch, D. L., Chiang, J., Dingus, B. L., Esposito, J. A., Fierro, J. M., Hartman, R. C. et al., 1994, ApJS, 94, 551F

Foellmi, C., Depagne, E., Dall, T. H. & Mirabel, I. F., 2006, astro-ph/0606269

Forman, W., Jones, C., Cominsky, L., Julien, P., Murray, S., Peters, G., Tananbaum, H., Giacconi, R., 1978, ApJS, 38, 357F

Frank, J., King, A., Raine, D., 2002, Accretion Power in Astrophysics (third ed.). Cambridge University Press.

Freyberg, M. J., Altieri, B., Bermejo, D., Esquej, M. P. et al., 2006, Proceedings to the "The X-ray Universe 2005", ed.: Wilson, A., vol. 604, p. 913

Frontera, F., Amati, L., Zdziarski, A. A. et al., 2003, ApJ, 592, 1110

Gallo, E., Fender, R. P., Pooley, G. G., 2003, MNRAS, 344, 60G

Gallo, E., Corbel, S., Fender, R. P., Maccarone, T. J. & Tzioumis, A. K., 2004, MNRAS, 347L, 52G

George, I. M. & Fabian, A. C., MNRAS, 1991, 249, 352

Giacconi, R., Gursky, H., Paolini, F. R., Rossi, B. B., 1962, Physical Review Letters, 9, 439

Gilfanov, M., Churazov, E. & Revnivtsev, M., 2000, Proceedings of 5-th Sino-German workshop on Astrohpysics, 1999, Eds. Gang Zhao, Jun-Jie Wang, Hong Mei Qiu and Gerhard Boerner, SGSC Conference Series, vol.1, pp.114-123, astro-ph/0002415

Goldwurm, A., David, P. & Foschini et al., 2003, A&A, 411L, 223G

Grabelsky, D. A., Maltz, S. M., Purcell, W. R., et al., 1995, ApJ, 441, 800G

Graham, J. A., 1992, PASP, 104, 479G

Grebenev, S., Sunyaev, R., Pavlinsky, M. et al., 1993, A&AS, 97, 281G

Greeley, B. W., Blair, W. P., Long, K. S. & Raymond, J. C., 1999, ApJ, 513, 491

Greene, Bailyn & Orosz 2001, ApJ, 554, 1290

Grove, J. E., Johnson, W. N., Kroeger, R. A. et al., 1998, ApJ, 500, 899

Grove, J. E., Strickman, M. S., Matz, S. M., Hua, X.-M., Kazanas, D. & Titarchuk, L., 1998, ApJ, 502L, 45G

Guessoum, N., Jean, P. & Prantzos, N., 2006, A&A, 457, 753G

Gu, S.-h., Chen, P.-s., Choy, Y.-k., Leung, K.-c. et al., 2004, A&A, 423, 607

Harding, A. K. & Daugherty, J. K., 1991, ApJ, 374, 687

Harmon, B. A., Wilson, C. A., Paciesas, W. S., et al., 1994, ApJ, 425L, 17H

Hartman, R. C., Bertsch, D. L., Bloom, S. D., Chen, A. W. et al., 1999, ApJS, 123, 79H

Hawley, J. F., Balbus, S. A., Stone, J. M., 2001, ApJ, 554, L49

Hermsen, W., Swanenburg, B. N., Bignami, G. F., Boella, G., Buccheri, R., Scarsi, L. et al., 1977, Natur, 269, 494H

Hess, V. F., 1913, Phys. Zeitschrift, 14, 610

Hewitt, A. & Burbidge, G., 1993, ApJS, 87, 451H

Homan, J., Wijnands, R., van der Klis, M., Belloni, T., van Paradijs, J., Klein-Wolt, M., Fender, R. & Méndez, M., 2001, ApJS, 132, 377H

Homan J.; Wijnands R.; van den Berg, M., 2003, A&A, 412, 799H

Homan, J. & Belloni, T., 2005, Ap&SS, 300, 107H

Homan, J., 2005, ATel 440

Homan, J., Buxton, M., Markoff, S. et al., 2005, ApJ, 624, 295H

Homan et al., 2007, (in prep.)

Hjellming, R. M., & Rupen, M. P., 1995, Nature, 375, 464

Hua, X. & Titarchuk, L., 1995, ApJ, 449, 188

Hynes, R. I., Steeghs, D., Casares, J., Charles, P. A. & O'Brien, K., 2003, ApJ, 583L, 95H

Hynes, R. I., Steeghs, D., Casares, J., Charles, P. A. & O'Brien, K., 2004, ApJ, 609, 317H

Ibragimov, A. Poutanen, J. Gilfanov, M., et al., 2005, MNRAS, 362, 1435I

Ioannou, Z., van Zyl, L., Naylor, T., Charles, P. A. et al., 2003A&A, 399, 211I

Jansen, F., Lumb, D., Altieri, B., et al., 2001, A&A, 365, L1

Joinet, A. Jourdain, E., Malzac, J., Roques, J. P., et al., 2006, astro-ph/0611064

Kang, Y. W., Lee, H.-W., Hong, K. S., Kim, C.-H. & Guinan, E. F., 2004, 128, 846

Kaiser, C. R., Hannikainen, D. C., 2002, MNRAS, 330 225

Kazarovets, E. V., Samus, N. N., Durlevich, O. V., 1998, IBVS, 4655, 1K

Kazarovets, E. V., Samus, N. N., Durlevich, O. V., Frolov, M. S., Antipin, S. V. et al., 1999, IBVS, 4659, 1K

Kholopov, P. N., Samus, N. N., Kazarovets, E. V., Perova, N. B., 1985, IBVS, 2681, 1K

Kholopov, P. N., Samus', N. N., Kazarovets, E. V., Kireeva, N. N., 1987, IBVS, 3058, 1K

Kholopov, P. N., Samus, N. N., Frolov, M. S., Goranskij, V. P., Gorynya, N. A. et al., 1998, GCVS, 4.C, 0K

Klebesadel, R. W., Strong, I. B. & Olson, R. A., 1973, ApJ, 182L, 85K

Klein, O. & Nishina, Y., 1929, Z. Physik, 52, 853

Kolhörster, W., 1914, Deutsche Phys. Gesellschaft, Verhandlungen 16, 719

Kong, A. K. H., Kuulkers, E., Charles, P. A. & Homer, L., 2000, MNRAS, 312L, 49K

Kraushaar, W., Clark, G. W., Garmire, G., Helmken, H., Higbie, P. & Agogino, M., 1965, ApJ, 141, 845K

Krimm, H. A., Barbier, L., Barthelmy, S. D., et al. 2006, ATel 904

Krimm, H. A., Barbier, L., Barthelmy, S. D., et al. 2006, ATel 968

Kubota, A., Makishima, K., & Ebisawa, K., 2001, ApJ, 560, L147

Kukarkin, B. V., Kholopov, P., N., Artiukhina, N. M., et al., 1982, VizieR Online Data Catalog, ref. II/140

Kurucz, R. L., 1992, in the Stellar Populations of Galaxies, IAU Symp., No. 149, ed. B. Barbuy and A. Renzini (Kluwer Acad. Publ.: Dordrecht),225

Kurtz, M.J. & Mink, D. J., 1998, PASP, 110, 934

Kuster, M., 2004, Ph.D. thesis, Eberhard-Karls-Universität Tübingen

Kuulkers, E., Parmar, A. N., Owens, A. et al., 1997, A&A, 323L, 29K

Kuulkers, E., Wijnands, R., Belloni, T., Mendez, M., van der Klis, M. & van Paradijs, J., 1998, ApJ, 794, 753

Kuulkers, E., Shaw, S., E., Paizis, A., Chevenez, J. et al., 2007, astro-ph/0701244

Laor, A., 1991, ApJ, 376, 90

Labanti, C., Di Cocco, G., Ferro, G., Gianotti, F. et al., 2003, A&A, 411L, 149L

Lamb, R. C. & Macomb, D. J., 1997, ApJ, 488, 872L

Latham 1992; Latham, D. W., 1992, in IAU Coll. 135, Complementary Approaches to Double and Multiple Star Research, ASP Conf. Ser. 32, eds. H. A. McAlister & W. I. Harkopf (San Francisco: ASP), 110.

Leising, M. D. & Share, G. H., 1990, ApJ, 357, 638L

Levine, A. M., Lang, F. L., Lewin, W. H. G., Primini, F. A., Dobson, C. A., Doty, J. P. et al., 1984, ApJS, 54, 581L

Lin, Y. C., Bertsch, D. L., Dingus, B. L., Esposito, J. A., Fichtel, C. E., Fierro, J. M. et al., 1996, ApJS, 105, 331L

Liu, Q. Z., van Paradijs, J., van den Heuvel, E. P. J., 2000, A&AS, 147, 25L

Liu, Q. Z., van Paradijs, J., van den Heuvel, E. P. J., 2001, A&A, 368, 1021

Liu, Q.-Y. & Yang, Y.-L., 2003, 3, 142

Lebrun, F., Leray, J. P., Lavocat, P., et al., 2003, A&A, 411, L141

Li, L., Liu, Q., Zhang, F. & Han, Z., 2001, AJ, 121, 1091

Lubiński, P., Dubath, P., Paltani, S. et al., 2005, INTEGRAL cross-calibration status for OSA 5.1, ISDC/CCR 1.0

Lund, N., Budtz-Jorgensen, C., Westergaard, N. J., et al., 2003, A&A, 411, L231

Macomb, D. J. & Gehrels, N., 1999, ApJS, 120, 335M

Mahoney, W. A., et al., 1984, ApJ, 286, 578

Magdziarz, P. & Zdziarski, A. A., 1995, MNRAS, 273, 837M

Malizia, A., Bassani, L., Zhang, S. N., Dean, A. J., Paciesas, W. S. & Palumbo, G. G. C., 1999, ApJ, 519, 637M

Malzac, J., Beloborodov, A. M. & Poutanen, J., 2001, MNRAS, 326, 417M

Malzac, J., Petrucci, P.O. Jourdain, E., Cadolle Bel, M., Sizun, P., Pooley, G. et al., 2006, A&A, 448, 1125M

Markert, T. H., Canizares, C. R., Clark, G. W. et al., 1973, ApJ, 184L, 67M

Markoff, S., Falcke, H. & Fender, R., 2001, A&A, 372, 25

Markoff, S., Nowak, M., Corbel, S., Fender, R. & and Falcke, H., 2003, A&A, 397, 645

Markoff, S., Nowak, M. A., Wilms, J., 2005, ApJ, 635, 1203M

Markwardt, C. & Swank, J., (2005), ATel 414

Mas-Hesse, J. M., 1998, private communication

Mas-Hesse, J. M., Giménez, A., Culhane, J. L., et al., 2003, A&A, 411, L261-L268

Mason, K. O., Breeveld, A., Much, R., Carter, M., et al., 2001, A&A, 365L, 36M

McClintock, J. E., Remillard, R. A., 2003, "Compact Stellar X-ray Sources," eds. W.H.G. Lewin and M. van der Klis, Cambridge University Press

McConnell, M. L. Ryan, J. M. Collmar, W. et al., 2000, ApJ, 543, 928M

McConnell, M. L. Zdziarski, A. A. Bennett, K. et al., 2002, ApJ, 572, 984M

McGale, P. A., Pye, J. P. & Hodgkin, S. T., 1996, MNRAS, 280, 627

Mendez, M., & van der Klis, M., 1997, ApJ 479, 926M

Merloni, A., Fabian, A. C. & and Ross, R. R., 2000, MNRAS, 313, 193

Messina, S., Pizzolato, N., Guinan, E. F. & Rodonò, 2003, A&A, 410, 671M

Miller, K. A., Stone, J. M., 2000, ApJ, 534, 398

Miller, J. M., Ballantyne, D. R., Fabian, A. C., 2002, MNRAS, 335, 865M

Miller, J. M. , Fabian, A. C., Reynolds, C. S., Nowak, M. A., Homan, J. et al., 2004, 606, 131L

Miller, J. M., Raymond, J., Fabian, A. C., Homan, J., Nowak, M. A., 2004, ApJ, 601, 450

Miller, J. M., Fabian, A. C., Nowak, M. A., & Lewin, W. H. G., 2005, in the Proceedings of the Tenth Marcel Grossman Meeting, Rio de Janiero, Brazil, eds. M. novello, S. Perez Bergliaffa, & R. Ruffini, World Scientific Publishing, Singapore

Miller, J. M., 2006, Astron. Nachr. in the proceedings of the XMM-Newton workshop "Variable and Broad Iron Lines Around Black Holes", eds. A. C. Fabian and N. Schartel, 2006, Madrid, Spain

Miller, J, M., Raymond, J, Fabian, A., Steeghs, D., et al., 2006, Nat, 441, 953

Miller, J. M., ARA&A, vol. 45

Miller, J. M., Reynolds, C. S., Fabian, A. C. et al., astro-ph/0802.3882

Miller, J. M., Kuulkers, E., Caballero-García, M. D., et al. 2007, ATel 980

Mitsuda, K., Inoue, H., Koyama, K., et al., 1984, PASJ 36, 741-759

Miyakawa et al. 2007, astro-ph/0702087

Miyamoto, S., Kimura, K., Kitamoto, S. et al., 1991, ApJ, 383, 784M

Miyamoto, S. & Kitamoto, S., 1991, ApJ, 374, 741M

Morrison, P., 1958, Nuo Cim 7, 858

Motch, C., Ilovaisky, S. A. & Chevalier, C., 1982, A&A, 109L, 1M

Motch, C., Ricketts, M. J., Page, C. G., et al., 1983, A&A, 119, 171M

Motch, C., Ilovaisky, S. A., Chevalier, C., et al. 1985, SSRv, 40, 219M

Nandra, K., O'Neill, P. M., George, I. M. & Reeves, J. N., 2007, astro-ph/0708.1305, accepted for publication in MNRAS

Narayan, R. (1996), ApJ 462, 136-141

Nespoli, E., Belloni, T., Homan, J., Miller, J. M., Lewin, W. H. G., Méndez, M. & van der Klis, M., 2003, A&A, 412, 235

Niarchos, P. G., Hoffmann, M. & Duerbeck, H. W., 1997, 124, 291

Nowak, M., A., 1995, PASP, 107, 1207

Nowak, M. A., Wilms, J. & Dove, J. B., 1999, ApJ, 517, 355N

Nowak, M. A., Wilms, J. & Dove, J. B., 2002, MNRAS, 332, 856

O'Donoghue, D., Koen, C., Kilkenny, D., et al., 2003, MNRAS, 345, 506

Orosz, J. A., Bailyn, C. D., 1997, ApJ, 477, 876

Orosz, J. A., Remillard, R. A., Bailyn, C. D., & McClintock, J. E., 1997, ApJ, 478, L83

Padovani, P. & Giommi, P., 1995, MNRAS, 277, 1477P

Padovani, P., 1998, private communication

Pinkau, K., 1979, Natur, 277, 17P

Piquard, S., Halbwachs, J.-L., Fabricius, C., Geckeler, R., Soubiran, C. & Wicenec, A., 2001, A&A, 373, 576P

Prsa & Zwitter 2005; ApJ 628, 426

Remillard, R. A. & McClintock, J. E, 2006, ARA&A, 44, 49

Retter, A., Richards, M. T. & Wu, K., 2005, ApJ, 621, 417

Reynolds C. S., Nowak M. A., 2003, PhR, 377, 389

Rodriguez, J., Corbel, S. & Tomsick, J. A., 2003, ApJ, 595, 1032

Rodriguez, J., Fuchs, Y., Hannikainen, D., Vilhu, O., Shaw, S., 2004, ESA SP-552, 377

Rodriguez, J., Pooley, G., Hannikainen, D. C., Lehto, H. J., Belloni, T., et al., 2006, "Proceedings of the VI Microquasars Workshop: Microquasars and beyond", eds. Belloni, T., PoS(MQW6)O24

Rodriguez, J., Hannikainen, D. C., Shaw, S. E. et al., 2007, ApJ, astro-ph/0712.0456

Roques, J-P., Jourdain, E., 2005, SPI-NS-0-4305-CESR

Roques, J-P., Jourdain, E. & Shrader, C., 2005, SPI-NS-0-4308-CESR

Ross, R. R., Fabian, A. C., Young, A. J., 1999, MNRAS, 306, 461

Rubin, B. C., Harmon, B. A., Paciesas, W. S., et al. 1998, ApJ, 492L, 67R

M.P. Rupen (NRAO/GSFC), V. Dhawan, A.J. Mioduszewski (NRAO), 2005, ATel 419

Rybicki, G. B. & Lightman, A. P., 1979, Radiative processes in astrophysics. New York, Wiley-Interscience, 393

Sandage, A., Osmer, P., Giacconi, R., et al., 1966, ApJ, 146, 316

Saito, K., Homan, J., Yamaoka, K., Fukuyama, M., 2007, astro-ph/0702022

Scholz, A. & Jayawardhana, R., 2006, 638, 1056

Shakura, N. I., Sunyaev, R. A., 1973, A&A, 24, 337

Shapiro, S. L. and Teukolsky, S. A., 1983, Black Holes, White Dwarfs and Neutron Stars: The Physics of Compact Objects (Wiley, New York)

Shaposhnikov, N., Swank, J. H., shrader, C. R. et al., 2006, astro-ph/0609757

Shimura, T. & Takahara, F., 1995, ApJ, 445, 780

Sidoli, L., Oosterbroek, T., Parmar, A. N. et al., 2001, A&A, 379, 540S

Skinner, G. & Connell, P., 2003, A&A, 411, L123

Smith, D. M., Leventhal, M., Cavallo, R., Gehrels, N., Tueller, J., Fishman, G., et al., 1996, ApJR, 471, 783S

Smolinski, J., Climenhaga, J. L., Huang, Y., Jiang, S., Schmidt, M. & Stahl, O., 1993, Space Science Reviews, 66, 231

Steiman-Cameron, T. Y., Scargle, J. D., Imamura, J. N., et al., 1997, ApJ, 487, 396S

Stellingwerf, R., 1978, ApJ, 224, 953

Swanenburg, B. N., Bennett, K., Bignami, G. F., Buccheri, R., Caraveo, P., Hermsen, W. et al., 1981, ApJ, 243L, 69S

Space Telescope Science Institute (STScI) and Osservatorio Astronomico di Torino (2001)

Strohmayer, T. E., 2001, ApJ, 552, L49

Sunyaev, R. A., Trümper, J., 1979, Nat, 279, 506S

Sunyaev, R. A. & Titarchuk, L. G., 1980, A&A, 86, 121S

Swank, J. H., Smith, E. A., Smith, D. M., et al. 2006, ATel 944

Takami, M., Bailey, J., Gledhill, T. M., Chrysostomou, A. & Hough, J. H., 2001, MNRAS, 323, 177

Tanaka, Y., Lewin, W. H. G., 1995, Black-hole binaries, In : Lewin, W. H. G., van Paradijs J., van der Heuvel, E. P. J., (Eds.), X-ray Binaries, Cambridge University Press, Cambridge, 308-330

Thompson, D. J., Fichtel, C. E., Hartman, R. C., Kniffen, D. A. & Lamb, R. C., 1977, ApJ, 213, 252T

Thompson, D. J., Bertsch, D. L., Dingus, B. L., Esposito, J. A., Etienne, A. et al., 1995ApJS..101..259T

Thompson, D. J., Bertsch, D. L., Dingus, B. L., Esposito, J. A., Etienne, A. et al., 1996, ApJS, 107, 227T

Thorne, K. S., 1974, ApJ, 191, 507T

Tingay, S. J., et al., 1995, Nature, 374, 141

Titarchuk, L., 1994, ApJ, 434, 570

Titarchuk, L. & Shrader, C. R., 2002, ApJ, ApJ, 567, 1057

Tomsick, J. A., Kaaret, P., Kroeger, R. A. & Remillard, R. A., 1999, ApJ, 512, 892

M.A.P. Torres (CfA), D. Steeghs (CfA), P. Jonker (SRON), P. Martini (CfA), 2005, ATel 417

Strüdel, L., Briel, U., Dennerl, K., et al., 2001, A&A, 365, L18

Turner, T. J., Nandra, K., Turcan, D., George, I. M., 2001, AIPC, 599, 991T

Turner, M. J. L., Abbey, A., Arnaud, M., et al., 2001, A&A, 365, L27

Ubertini, P., Lebrun, F., Di Cocco, G., Bazzano, A., Bird, A. J., 2003, A&A, 411L, 131U

Ueda, Y., Ebisawa, K. & Done, C., 1994, PASJ, 46, 107U

Ueda, Y., Inoue, H., Tanaka, Y., et al., 1998, ApJ, 492, 782

van Hamme, W., 1993, AJ, 106, 2096

van der Hooft, F., Heemskerk, M. H. M., Alberts, F., & van Paradijs, J., 1998, A&A, 329, 538

van der Klis, M., 2004, astro-ph/0410551, to appear in Compact stellar X-ray sources, Lewin & van der Klis (eds), Cambridge University Press

van der Klis, M., 2006, Compact Stellar X-ray Sources, Cambridge University Press Book

van de Steene, G. C., Wood, P. R. & van Hoof, P. A. M., 2000, Astronomical Society of the Pacific Conference Series, eds.: Kastner, J. H. and Soker, N. and Rappaport, S., vol.: 199, p.: 191

Vargas, M., Goldwurm, A., Denis, M., Paul, J., Borrel, V., Roques, J. P., Jourdain, E., et al., 1996, A&AS, 120C, 291V

Vargas, M. et al., 1997, ESA-SP-382, 129, eds.: C. Winkler, T. J. Courvoisier, P. Durouchoux

Varricatt, W. P., Williams, P. M., Ashok, N. M. et al., 2004, MNRAS, 351, 1307V

Vedrenne, G., Roques, J. P., Schönfelder, V., 2003, A&A, 411, L63

Véron-Cetty, M. P. & Véron, P., VizieR Online Data Catalog, ref. VII/188

Véron-Cetty, M. P. & Véron, P., 1998, yCat, 7207, 0V

Voges, W., Gruber, R., Haberl, F., 1994, VizieR Online Data Catalog, ref. IX/11

Voges, W., Aschenbach, B., Boller, T., Bräuninger, H., Briel, U., Burkert, W., Dennerl, K., Englhauser, J., Gruber, R. & Haberl, F. et al., 1999, A&A, 349, 389V

Voges, W., Aschenbach, B., Boller, T., Bräuninger, H., Briel, U., Burkert, W., Dennerl, K., Englhauser, J., Gruber, R. & Haberl, F. et al., 2000, IAUC, 7432R, 1V

Walter et al. 2007, A&A, 461, L17

Warner, 1995, Cataclysimic Variable Stars. Cambridge Univ. Press, Cambridge

Westergaard, N. J., Kretschmar, P. & Oxborrow et al., 2003, 411L, 257W

White, N. E., Giommi, P., Angellini, L., 1995, VizieR Online Data Catalog, ref. IX/12

Winkler, C., Courvoisier, T. J.-L., Di Cocco, G., Gehrels, N. & Giménez, A., 2003, A&A, 411L, 1W

Witham, A. R., Knigge, C., Aungwerojwit, A., Drew, J. E., Gänsicke, B. T., Greimel, R., Groot, P. J., Roelofs, G. H. A., Steeghs, D. & Woudt, P. A., 2007, MNRAS, 382, 1158W

Williams, R. E., 1992, AJ, 104, 725W

Wilms, J., Nowak, M. A., Dove, J. B. et al., 1999, ApJ, 522, 460W

Wilms, J., Nowak, M. A., Pottschmidt, K., Pooley, G., G. & Fritz, S., 2006, A&A 447, 245-261

Klein-Wolt, M. & van der Klis, M., 2007, ApJ, astro-ph/0711.1274

Wolter, A., Ciliegi, P., della Ceca, R., Gioia, I. M., Giommi, P., 1997, MNRAS, 284, 225W

Wu, K., Soria, R., Hunstead, R. W., Johnston, H. M., 2001, MNRAS, 320, 177

Yang, Y. & Liu, Q., 2001, AJ, 122, 245

Yuan, F. & Zdziarski, A. A., 2004, MNRAS, 354, 953

Yuan, F., Zdziarski, A. A., Xue, Y. & Wu, X.-B., 2007, ApJ, 659, 541Y

Zacharias, N., Urban, S. E., Zacharias, M. I., Wycoff, G. L., Hall, D. M., Monet, D. G. & Rafferty, T. J., 2004, AJ, 127, 3043Z

Zdziarski, A. A., Poutanen, J., Mikolajewska, J., et al., 1998, MNRAS, 301, 435Z

Zdziarski, A. A., Grove, J. E., Poutanen, J., Rao, A. R., 2001, ApJ, 554, L45

Zdziarski, A. A., Gierliński, M. & Mikołajewska, J., 2004, MNRAS, 351, 791Z

Zhang, S. N., Wilson, C. A., Harmon, B. A., Fishman, G. J., Wilson, R. B., Paciesas, W. S., Scott, M., & Rubin, B. C., 1994, IAU Circ. 6209